



## ELECTROSPRAYING OF POLYMER SOLUTIONS FOR THE GENERATION OF MICRO-PARTICLES, NANO-STRUCTURES AND GRANULAR FILMS

**Eszter Bodnár**

**ADVERTIMENT.** L'accés als continguts d'aquesta tesi doctoral i la seva utilització ha de respectar els drets de la persona autora. Pot ser utilitzada per a consulta o estudi personal, així com en activitats o materials d'investigació i docència en els termes establerts a l'art. 32 del Text Refós de la Llei de Propietat Intel·lectual (RDL 1/1996). Per altres utilitzacions es requereix l'autorització prèvia i expressa de la persona autora. En qualsevol cas, en la utilització dels seus continguts caldrà indicar de forma clara el nom i cognoms de la persona autora i el títol de la tesi doctoral. No s'autoritza la seva reproducció o altres formes d'explotació efectuades amb finalitats de lucre ni la seva comunicació pública des d'un lloc aliè al servei TDX. Tampoc s'autoritza la presentació del seu contingut en una finestra o marc aliè a TDX (framing). Aquesta reserva de drets afecta tant als continguts de la tesi com als seus resums i índexs.

**ADVERTENCIA.** El acceso a los contenidos de esta tesis doctoral y su utilización debe respetar los derechos de la persona autora. Puede ser utilizada para consulta o estudio personal, así como en actividades o materiales de investigación y docencia en los términos establecidos en el art. 32 del Texto Refundido de la Ley de Propiedad Intelectual (RDL 1/1996). Para otros usos se requiere la autorización previa y expresa de la persona autora. En cualquier caso, en la utilización de sus contenidos se deberá indicar de forma clara el nombre y apellidos de la persona autora y el título de la tesis doctoral. No se autoriza su reproducción u otras formas de explotación efectuadas con fines lucrativos ni su comunicación pública desde un sitio ajeno al servicio TDR. Tampoco se autoriza la presentación de su contenido en una ventana o marco ajeno a TDR (framing). Esta reserva de derechos afecta tanto al contenido de la tesis como a sus resúmenes e índices.

**WARNING.** Access to the contents of this doctoral thesis and its use must respect the rights of the author. It can be used for reference or private study, as well as research and learning activities or materials in the terms established by the 32nd article of the Spanish Consolidated Copyright Act (RDL 1/1996). Express and previous authorization of the author is required for any other uses. In any case, when using its content, full name of the author and title of the thesis must be clearly indicated. Reproduction or other forms of for profit use or public communication from outside TDX service is not allowed. Presentation of its content in a window or frame external to TDX (framing) is not authorized either. These rights affect both the content of the thesis and its abstracts and indexes.

ESZTER BODNÁR

*ELECTROSPRAYING OF POLYMER SOLUTIONS  
FOR THE GENERATION OF MICRO-PARTICLES,  
NANO-STRUCTURES, AND GRANULAR FILMS*

DOCTORAL THESIS

**Rovira i Virgili University**



UNIVERSITAT ROVIRA I VIRGILI

**2016**

UNIVERSITAT ROVIRA I VIRGILI

ELECTROSPRAYING OF POLYMER SOLUTIONS FOR THE GENERATION OF MICRO-PARTICLES, NANO-STRUCTURES AND GRANULAR FILMS

Eszter Bodnár

UNIVERSITAT ROVIRA I VIRGILI

ELECTROSPRAYING OF POLYMER SOLUTIONS FOR THE GENERATION OF MICRO-PARTICLES, NANO-STRUCTURES AND GRANULAR FILMS

Eszter Bodnár

UNIVERSITAT ROVIRA I VIRGILI

ELECTROSPRAYING OF POLYMER SOLUTIONS FOR THE GENERATION OF MICRO-PARTICLES, NANO-STRUCTURES AND GRANULAR FILMS

Eszter Bodnár

ESZTER BODNÁR

*ELECTROSPRAYING OF POLYMER SOLUTIONS  
FOR THE GENERATION OF MICRO-PARTICLES,  
NANO-STRUCTURES, AND GRANULAR FILMS*

DOCTORAL THESIS

**Supervised by Dr. Joan Rosell-Llompart**

**Department of Chemical Engineering**



UNIVERSITAT ROVIRA I VIRGILI

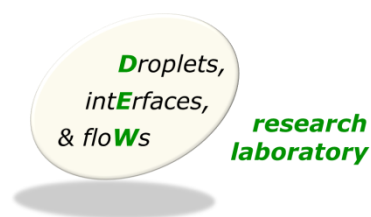
**Tarragona**

**2016**

UNIVERSITAT ROVIRA I VIRGILI

ELECTROSPRAYING OF POLYMER SOLUTIONS FOR THE GENERATION OF MICRO-PARTICLES, NANO-STRUCTURES AND GRANULAR FILMS

Eszter Bodnár



Department d'Enginyeria Química

Universitat Rovira i Virgili  
Campus Sescelades,

Av. Països Catalans, 26  
43007 Tarragona  
Tel: 977559658  
Fax: 977559667

Dr. Joan Rosell-Llompart,

I STATE that the present study, entitled “Electrospraying of polymer solutions for the generation of micro-particles, nano-structures, and granular films“ presented by Eszter Bodnár for the award of the degree of Doctor, has been carried out under my supervision at the Department d'Enginyeria Química (DEQ) of this university.

Tarragona 30<sup>th</sup> October, 2015

Dr. Joan Rosell-Llompart



UNIVERSITAT ROVIRA I VIRGILI

ELECTROSPRAYING OF POLYMER SOLUTIONS FOR THE GENERATION OF MICRO-PARTICLES, NANO-STRUCTURES AND GRANULAR FILMS

Eszter Bodnár

## Acknowledgements

During the preparation of this thesis I have accepted, with gratitude, many gifts from my supervisor, *Prof. Joan Rosell-Llompарт*: knowledge, guidance, encouragement, and a thousand different ways of support. Thank you!

I also would like to thank each former and current members of the DEW research group: *Prof. Jordi Grifoll, dr. Pavel Kiselev, dr. Luis Balam Modesto Lopez, Ajith, Nikolas, Laura, Evgenii, Luca*. They have been an inspiring company during these years.

I owe a big thank you to my *Family* and *Friends* for their patience and support.

Thanks to the financial support extended by the *Ministerio de Educación y Ciencia* via project CTQ2008-05758/PPQ, DPI2012-35687 & DPI2015-68969-P, and by the *Generalitat de Catalunya* (refs. 2009SGR-01529 and 2014SGR-1640). Also acknowledged is the scholarship granted by *Universitat Rovira i Virgili* and the financial support of *DEW Research Group*.

UNIVERSITAT ROVIRA I VIRGILI

ELECTROSPRAYING OF POLYMER SOLUTIONS FOR THE GENERATION OF MICRO-PARTICLES, NANO-STRUCTURES AND GRANULAR FILMS

Eszter Bodnár

# Table of contents

Summary .....	i
List of publications and conferences .....	iii
List of figures .....	v
List of tables .....	vii
1. Introduction .....	1
1.1. Electropray and its unique feature .....	1
1.2. Applications of electropray.....	2
1.3. Particle and film formation by electropray of polymer solutions: Physics and engineering aspects .....	4
1.3.1. Overview of electropray physics .....	5
1.3.2. Physics of particle formation.....	14
1.4. Thesis aims and structure .....	16
1.5. References .....	17
2. Polymeric microparticles and nanoparticles by electrospaying .....	29
2.1. Introduction .....	29
2.2. Materials and Methods .....	31
2.2.1. Materials.....	31
2.2.2. Electrospaying.....	32
2.2.3. Particle collection and imaging .....	34
2.3. Results .....	34
2.3.1. Terminology .....	34
2.3.1.1. <i>Particle kinds arising from jet break up</i> .....	34
2.3.1.2. <i>Coulombic instability vs fission, and progeny particle</i> .....	35
2.3.2. Effects due to the solvent vapor jacket.....	36
2.3.3. Particle morphologies vs. initial concentration .....	39

2.3.3.1.	<i>Poly(methyl)methacrylate morphologies from MEK solutions</i> .....	41
2.3.3.2.	<i>Polystyrene morphologies from MEK and DCM solutions</i> .....	43
2.3.3.3.	<i>Ethyl cellulose morphologies from MEK and DCM solutions</i> .....	48
2.4.	Discussion .....	51
2.4.1.	Fluid dynamic-to-solid structure transformation .....	52
2.4.2.	Polymer precipitation during jet breakup .....	55
2.4.3.	Production of non-filamented particles .....	56
2.5.	Conclusions .....	59
2.6.	References .....	61
3.	Polymeric nanostructures by electro spraying in non-solvent water vapor environment....	65
3.1.	Introduction .....	65
3.1.1.	Pore formation at high RH in electro spinning of PS solutions .....	67
3.1.2.	Description of VIPS/TIPS and BFF .....	68
3.2.	Materials and Methods .....	72
3.2.1.	Materials.....	72
3.2.2.	Electro spraying.....	73
3.2.3.	Particle collection and imaging .....	75
3.3.	Results and Discussion.....	75
3.3.1.	PMMA-350 morphologies from MEK solution at low and high RH.....	76
3.3.2.	PMMA-15 morphologies from MEK solutions at low and high RH .....	79
3.3.3.	EC morphologies from MEK solutions at low and high RH.....	80
3.3.4.	PS-350 morphologies from MEK solutions at three RH levels .....	82
3.3.5.	PS-35 morphologies from MEK solutions at three RH levels.....	84
3.3.6.	PS-35 and EC-15 morphologies from DCM solution at low and high RH .....	86
3.3.7.	Proposed mechanisms .....	87
3.4.	Conclusions .....	91
3.5.	References .....	92
4.	Structure and growth of granular films produced by electro spray deposition .....	96
4.1.	Introduction .....	96

4.2.	Materials and Method.....	98
4.2.1.	Materials.....	98
4.2.2.	Electrospray deposition apparatus.....	98
4.2.3.	Electrospray film deposition .....	100
4.2.4.	Deposits characterization .....	100
4.2.5.	Spray imaging experiments.....	101
4.3.	Results and Discussion.....	101
4.3.1.	Macroscopic features of the film.....	101
4.3.2.	Particle size, shape, and segregation by size .....	102
4.3.3.	Local mass distribution on the particulate film .....	105
4.3.4.	Film thickness, mass and porosity profile .....	108
4.3.5.	Hypothesis of electrostatic charging .....	112
4.4.	Conclusions .....	116
4.5.	References .....	118
4.6.	Appendix .....	122
5.	General conclusions .....	124

## Summary

This thesis is focused on the mechanisms of formation of microparticles and their granular films, obtained by electrospraying polymer solutions in the steady cone-jet mode. Electrospays (ES's) are dispersions of highly charged droplets which are released by electrohydrodynamic microjets into a gas. Electrospay is a unique method for producing electrically-charged micro- and nano-droplets in the gas phase, with near size monodispersity, and is unsurpassed by other liquid fragmentation methodologies, which produce larger droplets, and/or wider dispersion of droplet sizes. Therefore they have attracted interest for making solid nanoparticles. However, many questions remain about the mechanisms leading to the formation of such particles.

In the first study, we have produced polymeric particles and films of such particles under carefully controlled conditions of operation of the electrospay. We have performed by electrospraying different polymeric solutions under dry ambient conditions, and we have determined the role of the following factors on the drying process of the electrosprayed polymer solution droplets, and resulting morphologies: polymer (PMMA, EC, and PS), solvent (butanone, dichloromethane), initial polymer concentration, and polymer molecular weight (either “low” ~10-35 kDa, or “high” 220-350 kDa). The collected deposits have been analyzed by scanning electron microscopy, revealing a wide variety of particle morphologies. We show that these morphologies present transitions as the initial polymer concentration is reduced, depending on the fluid dynamic regime at which polymer vitrification happens. All of the morphologies have been attributed to either of four regimes identified to be: (1) Incomplete jet break up, (2) complete jet breakup without coulomb instabilities, (3) coulombic instabilities without progeny droplets, and (4) coulombic fission of main droplets (with emission of progeny droplets).

In our second study, we have used the solutions from the first study, and have established the changes in particle morphology due to water vapor in the ambient in which the electrospays are produced. In these experiments, ambient relative humidity (RH) was added to the factors from the first study. The most notable effect due to RH is the prevention of coulombic instabilities, due to earlier vitrification of the polymer

shell. Surface porosity changes from being inexistent under dry conditions, to porous at humidified conditions (~60-70 %RH) only under high molecular weight and high concentration when using butanone. However, when using dichloromethane, surface porosity develops for the low molecular weight solutions. For this solvent, we attribute the formation of the marked porous structure to the templating of the droplet surface by condensed water nanodrops. This proposed mechanism is similar to the phenomenon called breath figure formation (BFF), which has been described to explain similar structures on spin coating films, as well as on electrospun nanofibers. Another mechanism that agrees with the observations is vapor-induced phase separation (VIPS).

In our third study, we demonstrate that granular films made by deposition of dry polymeric particles from electrosprays grow non-linearly in time, due to accumulation of electrostatic charges on the film and their effect on the electrospray particle trajectories. This phenomenon has not been previously reported in the literature. We have characterized the growth dynamics (not only the expansion rate) of granular films of ethyl cellulose particles, in terms of film thickness, accumulated mass, and porosity, as a function of key factors: deposition time, ambient humidity, and deposition flux. This study is focused on a single-electrospraying source or needle, but has important implications for multiplexed systems, where the deposition fluxes can be significantly larger.



# List of publications and conferences

## Articles

- E. Bodnár, and J. Rosell-Llompart, “Growth Dynamics of Granular Films Produced by Electropray”, *Journal of Colloid and Interface Science*, 407, 536-545 (2013) 43.
- E. Bodnár, and J. Rosell-Llompart, “Polymeric microparticles and nanoparticles formation by electro spraying”. *To be submitted*.
- E. Bodnár, and J. Rosell-Llompart, “Polymeric nanostructures by electro spraying in non-solvent water vapor environment”. *To be submitted*.

## Conferences

- E. Bodnár, P. Kiselev, J. Rosell-Llompart. Thin Film Uniformity as a Function of Electropray Conditions. AAAR 28th Annual Conference (American Association for Aerosol Research), Minneapolis MN (USA), 26-30 October 2009
- E. Bodnár, P. Kiselev, J. Grifoll, J. Rosell-Llompart. Experiments and numerical simulation of electropray thin film formation. 8th International Aerosol Conference, Helsinki (FINLAND), 29 August - 3 September 2010
- E. Bodnár, P. Kiselev, J. Rosell-Llompart. Effect of relative humidity on the microstructure of electropray deposited polymer thin films. Nanospain 2011, Bilbao (SPAIN), 11-14 April 2011
- E. Bodnár, P. Kiselev, J. Grifoll, J. Rosell-Llompart. Morphology dependency of electropray-generated polymer particles and coatings on ambient humidity [B-WG07S1P53]. European Aerosol Conference 2012 (EAC-2012), Granada (SPAIN), 2-7 September 2012
- E. Bodnár, J. Grifoll, J. Rosell-Llompart. Growth Dynamics of Polymer Granular Films Produced by Electropray Deposition. 1st Iberian Meeting on Aerosol Science and Technology (RICTA-2013), Évora (PORTUGAL), 1-3 July 2013
- E. Bodnár, N. Sochorakis, J. Grifoll, J. Rosell-Llompart. Electrostatic charging during electropray deposition of polymer granular coatings. European Aerosol Conference 2013 (EAC-2013), Prague (CZECH REPUBLIC), 1-6 September 2013
- N. Sochorakis, E. Bodnár, J. Grifoll, J. Rosell-Llompart. Scaling of linearly aligned electrosprays [P10]. RICTA-2014 (2nd Iberian Meeting on Aerosol Science and Technology), Tarragona (SPAIN), July 7-9, 2014
- N. Sochorakis, J. Rosell-Llompart, J. Grifoll, E. Bodnár. Electro spraying from a Linear Array System [OP42-3]. IAC-2014 (9th International Aerosol Conference), Busan (KOREA), Aug. 28 –Sept. 2, 2014

N. Sochorakis, E. Bodnár, J. Grifoll, J. Rosell-Llompart. Multiple electrospaying from extractor-free Linear Arrays [O111]. AT 2015 (Aerosol Technology 2015), Tampere (FINLAND), June 15-17, 2015

N. Sochorakis, E. Bodnár, J. Grifoll, J. Rosell-Llompart. Electropray plumes dynamics in linearly multiplexed arrays of Taylor cones [20ELE\_O007]. EAC 2015 (European Aerosol Conference 2015), Milano (ITALY), September 6-11, 2015

## List of figures

Figure 1-1	Schematics of typical electro spray configuration and jet breakup modes in Newtonian and viscoelastic liquids. ....	5
Figure 1-2	Example of electro spray, Taylor cone and jet (cone-jet) and beginning of spray. ....	10
Figure 1-3	Examples of droplets undergoing Coulomb fission. ....	13
Figure 2-1	Electrospray setup. ....	33
Figure 2-2	Effect of co-flow on Taylor cone for various solutions in MEK. ....	37
Figure 2-3	Effect of co-flow on jet break-up in the case of high $M_w$ 5% w/v a,c) PS and b,d) PMMA. ....	38
Figure 2-4	Effect of co-flow on jet particle morphology in the case of low $M_w$ 5% w/v a,c) EC and b,d) PS. ....	39
Figure 2-5	Particle morphologies obtained from 350 kDa PMMA/MEK solutions. .	41
Figure 2-6	Particle morphologies obtained from 15 kDa PMMA/MEK solutions. ...	43
Figure 2-7	Particle morphologies obtained from 350kDa PS/MEK solutions. ....	44
Figure 2-8	Particle morphologies obtained from 35 kDa PS/MEK solutions. ....	46
Figure 2-9	Particle morphologies obtained from 35 kDa PS/DCM solution. ....	47
Figure 2-10	Particle morphologies obtained from 100 cps EC/MEK solutions. ....	49
Figure 2-11	Particle morphologies obtained from 4cps EC/MEK solutions. ....	50
Figure 2-12	Particle morphologies obtained from EC/DCM solutions. ....	51
Figure 2-13	Mechanisms for polymeric nanostructure formation from electrohydrodynamic (EHD) jetting. ....	53
Figure 3-1	Schematic comparison between VIPS and BFF. ....	69
Figure 3-2	Phase separation trajectories in binary (solvent/polymer) systems by TIPS, and ternary solvent/non-solvent/polymer system by VIPS. ....	70
Figure 3-3	Composition change in a material element on the droplet surface represented in a ternary phase diagram and a corresponding theoretical concentration profiles along the droplet radius. ....	71
Figure 3-4	Cloud point boundaries represented in ternary phase diagram. ....	73
Figure 3-5	Electrospray setup. ....	74
Figure 3-6	Cone and jet photos at low and high RH. ....	76

Figure 3-7	Effect of RH on the deposited morphologies obtained by electro spraying solutions of 350 kDa PMMA-MEK at different initial concentrations. ....	77
Figure 3-8	Effect of RH on the deposited morphologies obtained by electro spraying solutions of 15 kDa PMMA-MEK at different initial concentrations. ....	79
Figure 3-9	Effect of RH on the deposited morphologies obtained by electro spraying solutions of 220 kDa EC-MEK at different initial concentrations. ....	81
Figure 3-10	Effect of RH on the deposited morphologies obtained by electro spraying solutions of 15 kDa EC-MEK. ....	82
Figure 3-11	Effect of RH on the deposited morphologies obtained by electro spraying solutions of 350 kDa PS-MEK at different initial concentrations. ....	83
Figure 3-12	Effect of RH on the deposited morphologies obtained by electro spraying solutions of 35 kDa PS-MEK at different initial concentrations. ....	85
Figure 3-13	Effect of RH on the deposited morphologies obtained by electro spraying solutions of 35 kDa PS/DCM and 15 kDa EC/DCM. ....	86
Figure 4-1	Electrospray deposition chamber, close up of the silica tube (“needle”) and sheath gas tube, Taylor cone-jet meniscus at the end of the needle and annealed film with Newton rings. ....	99
Figure 4-2	Short and long exposure photographs of 2 EC films collected during 15 minutes under dry and under humid chamber ambient conditions. ....	102
Figure 4-3	Electrical current vs. time traces for two consecutive collections of EC/MEK electro spray coatings under dry and humid conditions. ....	103
Figure 4-4	SEM images of droplet residues collected from EC/MEK at dry and humid conditions. ....	105
Figure 4-5	SEM micrographs of two EC deposits collected at dry and humid conditions, for different radial positions from the center. ....	107
Figure 4-6	Radial profiles of local thickness and porosity for granular coatings for different deposition times and RH, and local thickness for the annealed films for $H = 20$ mm. ....	109
Figure 4-7	Radial profiles of the local thickness of granular coatings and of annealed films, and the local porosity of granular coatings (Eq. 4-1), for $H = 40$ mm. ....	110
Figure 4-8	Spray plume evolution during ES deposition. ....	113

## List of tables

Table 2-1 Some polymer properties .....	32
Table 2-2 Solution properties and electropray conditions .....	40
Table 3-1 Factors influencing surface porosity in PS-THF electrospinning studies and their interpretation about pore formation.....	68
Table 3-2 Some solvent properties .....	73
Table 3-3 Main trends in particle surface topography observed in the present study, changing different factors at high RH. ....	87
Table 4-1 Characteristics of the EC films. ....	116

# 1. Introduction

## 1.1. Electrospray and its unique features

This thesis is focused on the mechanisms of formation of microparticles and their granular films, obtained by electrospraying polymer solutions in the steady cone-jet mode. Electrosprays are dispersions of highly charged droplets which are released by electrohydrodynamic microjets into a gas. Therefore, electrospray is sometimes called *electro-hydrodynamic spraying* (EHDS), or *electro-hydrodynamic atomization* (EHDA). The droplets are in the micrometer range or smaller (depending on liquid properties and operating conditions), and their release from the end of an EHD-microjet is regular (quasi periodic), producing narrowly dispersed droplet sizes. Since the electrical field is the driving force for the atomization, there is no need for assistance from additional energy sources, such as gas streams (used for pneumatic atomization). Consequently, electrospray has low specific power consumption. In addition, since electrospray is based on laminar (non turbulent) microjet flows, different liquids can be combined in the same jet coaxially in order to produce structured multi-phase droplets, which can be used to make core-shell particles [1,2].

In sum, electrospray (ES) is a facile method for dispersing liquids as charged microdroplets and nano-sized droplets, with near size monodispersity, and is unsurpassed by other liquid fragmentation methodologies, which produce larger droplets, and/or wider dispersion of droplet sizes.

## 1.2. Applications of electrospray

The electrospray methodology has attracted much interest for applications [3,4] which seek either the small, uniform droplet size, or the high electrical charge density of the droplets, or need to obtain a fine dispersion over a large collection surface. It has been applied to the making of micro- and nano-particles of many different materials with diverse applications in mind [5].

The best known application of electrosprays probably is *electrospray ionization mass spectrometry*, or ESI-MS. It is an ionization method for converting ions in a solution to ions in the gas phase, which are transferred to a vacuum where their charge-mass ratio is determined by a so called mass spectrometer. This method has revolutionized biomedical science since John B. Fenn and colleagues developed it to generate protein ions [6], work for which Fenn received the Nobel Prize in chemistry in 2002 [7]. ESI-MS has nowadays become a standard analytical chemistry method. One interesting variation on this method is secondary electrospray ionization (SESI), in which an electrospray is used to ionize vapor molecules that are dispersed in trace quantities in ambient air, such as explosives, chemical warfare agents, or drugs, or in human breath, such as drugs, metabolites, or bacterial emissions [8,9].

Electrosprays have also been proposed as means to do *size spectrometry* of colloidal nanoparticles and viruses (MDa complexes) by means of aerosol characterization methods like differential mobility analysis [10,11]. In this methodology, the objects to be sized are dispersed by electrospray, and then their charged residues are charge-reduced using small gas-phase ions produced by either radioactive or soft x-ray sources.

Electrosprays have been also proposed as a one-step method to produce micro- and nano-particles via the spray-drying route [3,5,12,13] or by deposition in coagulation liquids [14], especially for pharmaceutical applications [3,5,15], often involving a drug and a polymer, and for electronics and power applications. The polymer in pharmaceutical particles is used for stabilizing the drug against crystallization and for controlling the rate of drug release in the body. In this application, the droplet can be viewed as a liquid template where the solute precipitates. The scaling up of particle production by electrospray faces challenges which are still being addressed in research work. However, the unique features of electrospray continue to draw researchers

interested in it as a versatile method for particle engineering. One of the attractive features of electrospray is the possibility of making core-shell structures by combining different solutions in a co-flow arrangement [1,15-19]. Another interesting configuration of electrospray for particle production is *bipolar coagulation*, in which electrospray droplets of different composition and opposite electrical polarity are generated in two opposing cone-jets, and are allowed to coagulate and chemically react in a micro-confined space [20].

Another field of application is *electrospray deposition*, or ESD, in which electrosprays are directed at solid surfaces for producing coatings or for dispersing small amounts of materials over large surface areas [21]. Interesting examples of ESD are the dispersion of platinum nanoparticles on carbon films for use as cathodes of PEMFC's (proton exchange membrane fuel cells) [22,23], and the coating of pharmaceutical carrier particles with drug nanoparticles [24,25]. One variation of ESD is patterned deposition using dielectric masks [26-30], or ion-induced focusing masks [31-33].

Some other related areas of research and application should be mentioned: (1) *EHD direct writing*, also called *EHD printing* or *EHD jet printing* [34,35], in which the cone-jet is used for directing a jet or micro-drops to precise locations on a moving planar substrate, (2) *electrospinning* [36-39], an important method for making polymeric nanofibers, which have interest in nanocomposites [40] and biomedical applications [41] (3) *colloidal thrusters*, designed for imparting thrust to spacecraft by accelerating electrospray-generated droplets or ions [42,43], and (4) *focused ion beams*, or FIB [44]. The latter two are vacuum applications in which a highly-conducting non-volatile liquid is used, e.g. an ionic liquid or liquid metal, whose Taylor cone can emit ions instead of a liquid jet [45]. Recently, Gamero-Castaño et al. has carried out sputtering of semiconducting surfaces by electrospray nanodroplets in vacuum without attempting focusing, demonstrating high etching rates and amorphization of silicon [46-48]. Electrospray and electrospinning have been used for creating a super-hydrophobic coating made of balls and nanofibers of polystyrene [49].

Non-steady EHD jetting modes has been used for “drop-on-demand”, which is the use of pulsed fields to eject electro-hydrodynamically and at will droplets or streams of droplets, typically for printing [50-55].



One constraint of electro spray is that the electrical conductivity of the liquid determines the range of flow rates at which it can be operated stably. In addition, the flow rate is generally low, typically about 0.1 mL/hr for typical solutions used in ESI-MS, and much lower for applications requiring high conductivity liquids such as colloidal thrusters or FIB. Therefore, electro spray excels in low flow rate applications. However, in many applications, the flow rate is insufficient, and has led to the development of multiplexed arrays of electro spray emitters.

The use of electro sprays for producing a wide range of nanomaterials require much higher flows than are possible with a single emitter, and motivate the development of robust *multiplexing* of ES emitters. Although this thesis will not develop multiplex systems, it is pertinent to review some of the key efforts in this direction. ES multiplexing has been proposed at lab scale for diverse goals. For example, pharmaceutical particles have been produced using 2D hexagonal arrays [56,57] and 1D linear arrays [58]. 2D arrays have also been designed for use as colloidal thrusters [59;60]. 1D arrays (linear or circular) have also been tested for nano-ESI-MS [61-63], and linear ones for near-field pulsed deposition [64] and electrohydrodynamic (EHD) jet printing [65]. Circular 1D, when equidistant nozzles in a circle experience identical electric field conditions [66], have become popular in electrospinning devices, which are closely related to electro spray. Another application of multiplexed electro sprays is gas cleaning [67]

### **1.3. Particle and film formation by electro spray of polymer solutions: Physics and engineering aspects**

Given the importance and technological potential of using EHD microjets to produce particles and coatings (as reviewed in previous section), it is relevant to understand the drying process of droplets and films in electro spray systems. Our particular interests are polymeric solutions, because of their relevance as reviewed in the previous section.

This section deals with electro sprays with solute precipitation (from solutions of non-volatile solutes).

### 1.3.1. Overview of electrospray physics

#### *Steady electrohydrodynamic spraying and scaling laws*

Figure 1-1(a) shows the typical configuration of electrospray. Liquid is pumped at a fixed known rate  $Q$  through a capillary tube (or “needle”), for example a flat-ended hypodermic needle. This needle is held at a high electrical potential  $V$  relative to a nearby electrode, in the Figure an Earth-grounded flat collector plate. For sufficiently high values of  $V$  and  $Q$ , the liquid meniscus adopts a stationary conical shape, whose vertex ejects a continuous stream in the form of an EHD microjet, which breaks into droplets. Since the microjet radius is independent of the needle radius (especially when the needle is much wider), clogging is not an issue, unlike in microjet methods based on extruding liquid through microholes.

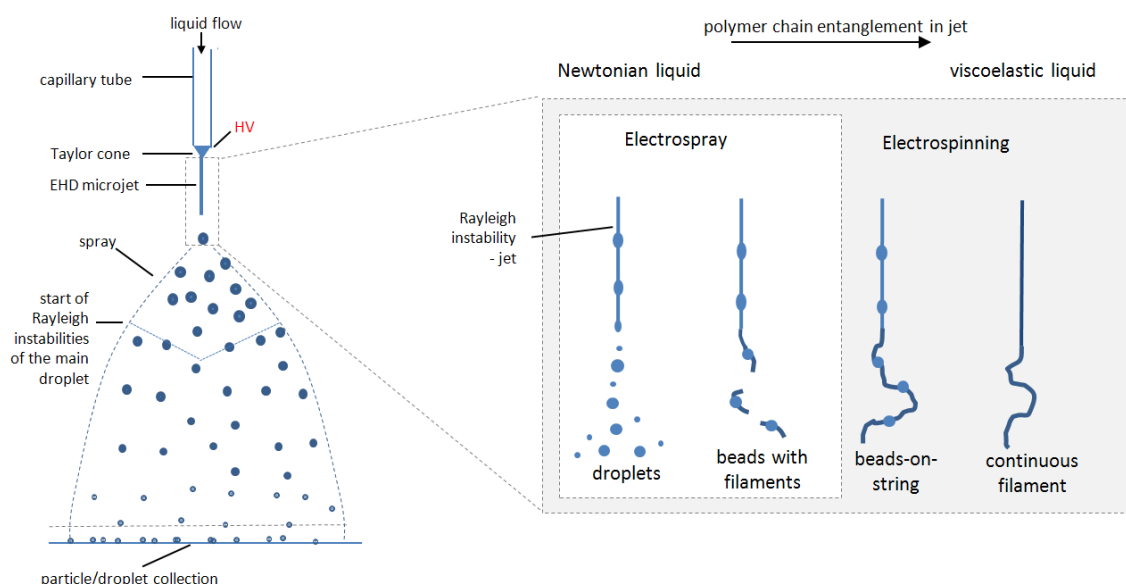


Figure 1-1 Schematics of (a) typical electrospray configuration with Taylor cone and electrohydrodynamic microjet and (b) jet breakup modes in Newtonian and viscoelastic liquids.

This thesis is concerned with the so called “steady cone-jet mode”, in which stable electrified liquid menisci produce continuous EHD microjets. Stable conical menisci can only be produced within finite ranges of  $V$  and of  $Q$  (defined by minimum and maximum values of these two parameters) which depend on the liquid mechanical and electrical properties and on the electrodes configuration. Typically, the operation flow rate decreases with increasing liquid electrical conductivity  $K$ , while the voltage

increases with liquid surface tension  $\gamma$  [68-71]. Outside of those limits, a rich variety of fluid dynamic modes exist, which include oscillatory modes, stable modes, multijet modes, etc. [72-77]. In addition, for high surface tension liquids, such as water sprayed in standard air, a Taylor cone may coexist with corona discharges [78,79].

In steady cone-jet mode, the electrified meniscus is conical, and is usually called “Taylor cone” in honor of G. I. Taylor, who proved mathematically that conical electrically charged interfaces at constant electrical potential can be in hydrostatic and electrostatic equilibrium [80-82]. In fact, conical menisci encountered in electrospaying are not in equilibrium because the jet emission convects electrical charge, thus overcoming charge transport by electrical conduction, which is necessary for maintaining electrostatic equilibrium [83,84].

Physical models have been developed to describe the electro-hydrodynamics of the transition region between the cone and the jet [85,86]. These models predict droplet mean size  $d_d$  (or jet radius) and electrical current  $I$ , as functions of  $Q$  and the liquid properties: liquid density  $\rho$ , surface tension  $\gamma$ , dynamic viscosity  $\mu$ , electrical conductivity  $K$ , and dielectric constant  $\varepsilon$ . Such relationships are called *scaling laws* of electrospay. Fernández de la Mora and Loscertales’s pioneered this approach with a model that considers relaxation of electrical charge in the transition region [83]. This model predicts the following scaling relationships for the jet diameter and the current:

$$d_d \approx \left( \frac{Q\varepsilon_0\varepsilon}{K} \right)^{1/3} \quad (1-1)$$

$$I = f(\varepsilon) \left( \frac{\gamma Q K}{\varepsilon} \right)^{1/2} \quad (1-2)$$

Gañán-Calvo [G97] has proposed the following alternative scaling laws:

$$d_d = 3.78\pi^{-2/3} 0.6Q^{1/2} \left( \frac{\rho\varepsilon_0}{\gamma K} \right)^{1/6} \quad (1-3)$$

$$I = 4.25 \left( \frac{QK\gamma}{\ln((Q/Q_0)^{1/2})} \right)^{1/2} \quad (1-4)$$

where  $Q_0$  is defined as  $\gamma\varepsilon_0/(K\rho)$ . Additional works have checked that these laws are fulfilled to different degrees depending on the electro sprayed liquid [86-92]. Experimentally, the current is better predicted than the droplet diameter, in part because the ratio of jet diameter to droplet diameter depends on factors not considered by these laws. Additional analytical and numerical models have been developed around this problem [19,84,85,93-99].

#### *EHD microjet breakup*

Liquid jets are produced and sustained when any unstable perturbations of the jet flow are convected downstream faster than they can travel upstream [100]. Unstable perturbations can eventually grow downstream, typically by the action of surface tension, leading to jet breakup. Such a jet is said to be *convectively unstable* [101]. In electro spray (Fig. 1-1(b)), Newtonian liquids form convectively unstable EHD microjets which break up into droplets. Examples of such liquids are water, organic solvent, or a dilute solution or nanoparticle dispersion in those solvents. On the other hand, EHD microjets of viscoelastic liquids, such as concentrated polymeric solutions, can resist the action of surface tension and form continuous filaments thanks to polymer chain entanglements (Fig. 1-1(b)). This is the basis of electrospinning [38]. However, in addition to chain entanglements, Fong et al. have shown that the electrical charge plays a key role in resisting the breaking action of surface tension on electrospun jets [102].

The rest of this section deals with jet behavior of Newtonian liquids. In electro spray, the best known jet breakup mode is the periodic (regular) breakup of a jet called *axisymmetric breakup mode*, *varicose breakup mode*, or *Rayleigh breakup mode*, in honor of Lord Rayleigh, who developed the first linear stability analysis of an infinitely long, neutral cylinder of an inviscid (i.e. non viscous) liquid [103,104]. Rayleigh's analysis predicts a droplet to jet diameter ratio  $d_d/d_j$  of  $\sim 1.89$ . In reality, Rayleigh breakup of either electrically neutral or charged jets often leads to two droplet types: "main droplets" and "satellite droplets", shown in Figure 1-1(b). Main drops form by accumulation of liquid at the wave crests (or swells), whereas satellite droplets form at the wave nodes (or valleys) as the liquid bridges formed between wave crests develop two breakup points [101]. Typically, the main droplets are significantly larger than satellite droplets.

Satellite drops do not always form [89], or, when they do, they may forward merge with the leading or rear merge with the trailing main drop, typically at low  $Re$  [69,101,105]. In these cases, the distribution of droplet sizes will be monomodal (made of main droplets only) and quasi monodisperse (due to the breakup periodicity). The merging of satellite droplets has been reported only in a few electrospray works [69,89,106].

Viscous stresses, neglected in Rayleigh's analysis, are noticeable when the Reynolds number for the capillary flow within the jet,  $Re$ , is  $\sim 1$  or smaller, where  $Re = (\rho \gamma d_j)^{1/2} / \mu$ , and where  $\rho$  is the liquid density,  $\gamma$  its surface tension coefficient,  $\mu$  its dynamic viscosity, and  $d_j$  the initial jet radius [107,101]. This Reynolds number is equal to the jet radius times the characteristic velocity of the capillary flow during breakup, called *capillary velocity*, namely  $[2\gamma/(\rho d_j)]^{1/2}$ , over the dynamic viscosity.

The ratio  $d_d/d_j = 1.89$  has been confirmed in electrospray studies where  $d_j > 7 \mu\text{m}$  and  $Re$  in the range  $\sim 10$ -30 [69,108,109]. However, this ratio becomes larger for much thinner microjets, for which viscous stresses cannot be neglected [87,110]. On the other hand, the role of electrical stresses on the jet break up is to reduce the fastest growing wavelength, thus reduce  $d_d/d_j$  [89,110,111].

Another common instability of EHD microjets is the *bending instability*, which causes the jet to undergo whipping as the result of amplification of non-axisymmetric perturbations [69,87,89]. (This instability is called *kink instability* in some older electrospray literature.) In the *whipping mode*, the jet either thrashes chaotically or undergoes helicoidal motions [17,112]. Jet whipping starts at a critical value of the liquid flow rate  $Q^*$  ( $> Q_{\min}$ , the lowest flow rate compatible with stability), where the main droplet size distribution bifurcates into two modes [87,113]. As  $Q$  is increased further from this value (as  $V$  is also increased), the jet whipping increases in amplitude, while the droplet size distribution becomes broader due to irregular jet breakup [87,89]. Cloupeau and Prunet-Foch attribute the appearance of whipping to the increase in charge-to-volume ratio of the jet [69]. Hartmann et al. [89] establish experimentally that, as the liquid flow rate is increased, jet whipping sets in when the normal electrical stress on the jet exceeds  $\sim 0.23$  times the capillary stress (following Melcher's model [111]). Hohman et al. predict mathematically that high charge tends to suppress the axisymmetric break up mode and enhance the bending instability [114]. The bending

instability is common also in electrospinning, as the growth rate of axisymmetric perturbations is greatly suppressed [38].

### *Electrospray plume structure*

Electrosprays are fine dispersions of liquid droplets into a gas, kept typically at atmospheric pressure, which expand under the repulsion of the droplets. The high electrical charge on the droplets prevents their agglomeration [115]. They are laminar aerosol flows, i.e. non-turbulent, unless gas turbulence is introduced by external energy sources. When the jet undergoes Rayleigh breakup, the satellite droplets segregate to the periphery of the spray plume, forming a shroud around the main spray made of the main droplets (see Figure 1-2) [106,109,116-118]. This effect is due to the fact that a unidimensional array of charges is radially unstable, as any fluctuations in the charges' radial positions are amplified by the (always-positive) radial electrical force due to the other droplets (especially neighboring ones). The radial acceleration is expected to be much higher for the satellite droplets than the main droplets because both of the key factors involved, charge-over-mass ratio and radial electrical field (whose product equals acceleration), are higher for the satellite droplets [106,109]. This mechanism is similar to that of the bending instability mentioned earlier. Note, however, that when the jet breaks up irregularly, ejecting droplets into a wide cone, the droplets also segregate by size in the spray [119].

The electrospray structure arising from Rayleigh-mode jets in the tube-collector configuration has been characterized by different methods, such as (i) Phase Doppler Anemometry and Sizing for supermicron main droplet sizes [109,118,120,121], (ii) time-of-flight and energy analysis methods, for submicron droplets in vacuum [106], and (iii) by numerical simulations of electrosprays [115,122-125]. From these studies we know that the number density varies strongly along the axis, and weakly in the radial direction. For electrosprays at ~1 atm and droplets under, roughly, 10 microns, the droplets' inertia (mass times acceleration) becomes negligible compared to the electrical and drag forces, some distance away from the zone of jet breakup. Then, the droplets follow electrophoretic motion, where the vector sum of the drag and electric forces is equal to zero [126]. Therefore, the electrical power gained by the charged particle is transmitted to the surrounding fluid (gas), where it is (partly) dissipated into heat by viscous stresses, which, however, cause negligible raises in gas temperature. The

droplet force on the gas (called reactive drag force) induces a laminar (i.e. non turbulent) gas flow pattern. This “induced gas flow” has been neglected on the argument that its average speed was much smaller than the droplet speed [127]. However, the data and analysis of Hartman et al. [117] and more recent numerical simulations [123,124] show that the axial gas speed near the spray centerline can be significantly higher than the average gas speed, up to 30-40% of the droplet axial velocities.

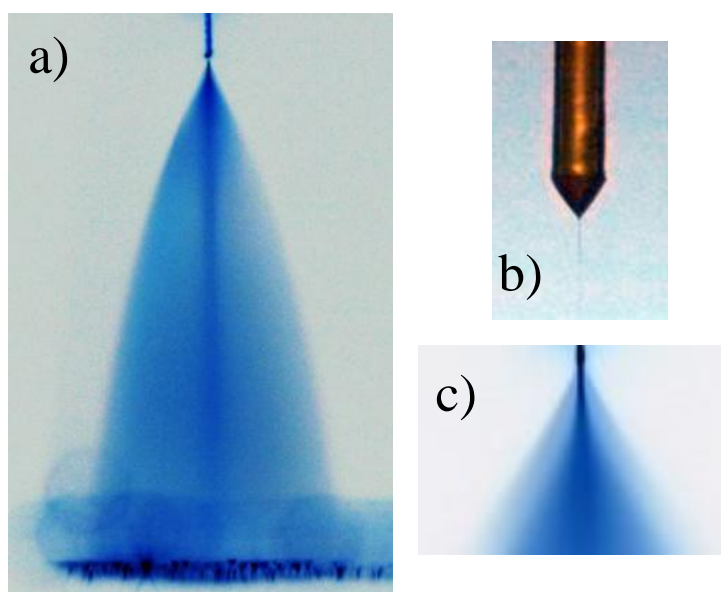


**Figure 1-2** Example of (a) electrospay (needle-collector distance: 20 mm, negative image), (b) Taylor cone and jet (cone-jet) (needle OD: 200 $\mu$ m), and (c) beginning of spray, showing outer spray due to satellite droplets surrounding inner spray due to main droplets (negative image).

Electrosprays of evaporating droplets have been studied also by both experimental and numerical methods [121,125,128]. In electrospays of volatile electrospays of methanol-water mixtures by Olumee et al. [121], the average drop diameter  $d_{10}$  decreases along the spray axis, as expected due to evaporation, when the initial droplet diameter is relatively large (5-7  $\mu$ m). However, it decreases when the initial droplet diameter is much smaller (1-2  $\mu$ m). This is either due to depletion of smaller sizes by an analogous mechanism to satellite-primary segregation [121], or by droplet shrinking below the smallest detectable size, due to evaporation and coulombic fission. Homopolar droplet coagulation is suggested also by these authors, but as less likely. The importance of each mechanism could be tested using numerical simulations as performed by Arumugham-Achari et al. [125].

Another important effect due to droplet evaporation is droplet cooling, which is very fast initially, as the latent heat is removed the droplet, and becomes slower, as the droplets become sufficiently cold and the latent heat is provided by heat conduction from the warmer gas to the droplet [125]. At this stage, the droplet temperature stabilizes at close to the wet bulb temperature of the solvent [125]. Recent experimental droplet temperature data obtained by ratiometric fluorescence agree with this picture [129]. Lagrangian numerical simulations of methanol, acetone, and heptane electrosprays of average drop diameter  $d_{10} = 10 \mu\text{m}$  confirm also this trend [125], and further show that (i) the background solvent vapor does not build up significantly compared to the saturation value, except very near the droplet generation zone, and (ii) that the temperature of the gas changes only slightly (a few °C). These simulations, which consider induced gas flow, have also shown that main droplets undergo Coulomb explosions within regions which are approximately conical, with distance from the electrospray needle of 7-15 mm, being slightly larger on the axis than at the spray periphery. Note that any progeny droplets from Coulomb explosions would not migrate to the periphery of the spray, but rather follow similar trajectories as the parent droplets under electrophoretic motion (as a result of their low inertia).

#### *Coulombic instabilities of the droplets*

*Coulombic instability* occurs to electrically charged droplets as they evaporate. While the droplet shrinks, the destabilizing electrical stress due to electrostatic repulsion between net charges on the droplet's surface increases faster than the stabilizing capillary tension stress. Rayleigh also developed the linear stability analysis for this problem, for a spherical droplet of an inviscid perfectly conducting fluid [104,130]. Instability is predicted for the critical droplet diameter

$$d_R = \left( \frac{q^2}{8\pi^2 \varepsilon_0 \gamma} \right)^{1/3} \quad (1-5)$$

where  $q$  is the droplet charge,  $\varepsilon_0$  the electrical permittivity of vacuum (8.854 pF/m) and  $\gamma$  the surface tension coefficient of the liquid [130,131]. Another way of expressing Rayleigh's critical condition is with the charge necessary for a droplet with diameter  $d$  to undergo instability, or *Rayleigh limit charge* [82]:

$$q_R = \sqrt{8\pi^2 \varepsilon_0 \gamma d^3} . \quad (1-6)$$



The stability criterion for a drop is the same when slight viscosity and charge relaxation by conduction are allowed, or when very rapid charge relaxation on a very viscous drop is allowed; but it is different for dielectric drops [104].

One of the characteristics of electrospays is the high charge of its droplets, which is comparable (though smaller) than  $q_R$ . Therefore, droplets of volatile electrospays are known to undergo extensive coulombic instabilities [125,132].

The Rayleigh instability of a charged droplet is a complex problem, which is still not fully understood theoretically, even for Newtonian (i.e. non rheological) fluids. Droplets made of low viscosity, conductive liquids undergo fragmentation (called *coulombic fission* or *Coulomb explosion*), in which two small jets form and break up into so called *progeny droplets* (or *offspring droplets*) [82]. Coulombic fissions of droplets in electrospays were first captured photographically by Gomez and Tang [132]. Their unstable heptane droplets are tens of  $\mu\text{m}$ 's in diameter, and some examples are shown in Figure 1-3(a)-(c). Similar behaviors have been photographed for electrodynamically levitated droplets of similarly large sizes, as shown in Figure 1-3(d) [133-135]. Using this technique, Giglio et al. [135] have been able to record detailed deformation pathways of droplets with  $d_R \sim 50\text{-}100 \mu\text{m}$ , and show that initially an unstable droplet elongates during the first few 100  $\mu\text{s}$ , becoming spindle-shaped, and then, over the following 1-5  $\mu\text{s}$ , it emits two microjets ( $d_j \sim 1 \mu\text{m}$ ) from the pointed ends of the droplet.

Micro- and nano-droplets are too small to be imaged by current methods (both because their shape cannot be captured accurately by optical imaging, and because the times scales are much shorter). Some electrospay studies have formed solid relics *during* coulombic instability of such droplets, by precipitation of a solute, e.g. for polymeric solutions [56,136] and for droplets undergoing a sol-gel reaction triggered by ambient moisture [137]. These images show spindle-like shapes probably associated to double-jet emissions, and single-filamented relics indicating single jet emissions, but also dumbbell shapes not seen with larger droplets. Sometimes, the filaments found in electrospayed polymeric solutions are very long (many times the droplet diameter, unlike in the imaging studies with microdroplets). This suggests that viscosity or viscoelasticity (or both) plays an important role in stabilizing the emitted jets, and maybe in their formation as well.

The charge and mass fractions released in coulomb fissions of large drops ( $d_R \sim 5\text{-}50 \mu\text{m}$ ) have been determined by various methods: (a) levitation in electrodynamic balances (EB) combined with detection of light Mie scattering detection for accurate droplet sizing before and after the explosion [138], (b) phase Doppler interferometry (PDI) detection in a “ping-pong” electrophoretic cell [139]. One conclusion from these studies is that coulombic explosions result in a large droplet charge loss (typically) 10-25% and negligible mass loss (<5%) (as reviewed in [139]; also [133]). Hunter and Ray have studied the effect of electrical conductivity by the EB method, and find that increases in conductivity result in reduced mass loss (< 3%), increased charge loss up to a limit (~30%) [140].

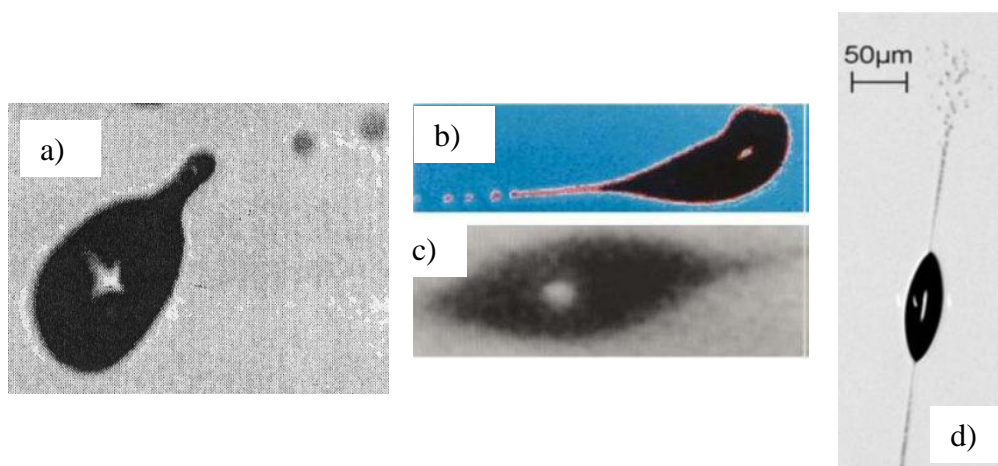


**Figure 1-3** Examples of droplets undergoing Coulomb fission.(a-c) [132], (d) [134]

The formation of one jet, instead of two opposite jets, can be produced when a droplet charged *below* the Rayleigh limit ( $q < q_R$ ) breaks up under the action of an applied field. In this case, the electrical stresses are significantly higher on one side of the droplet, from where a single jet is emitted [141,142]. Electrospays of volatile droplets can experience such high field strengths only near the region of jet break up [82,132]. Conceivably, the field due to a near passer-by charged drop (having different speed) could also trigger single-jet emission. Therefore electro spray droplets can undergo single-jet or double-jet emissions.

### 1.3.2. Physics of particle formation

The manufacturing of particles from liquid sprays is known as *spray drying*, and is widely used in the food, cosmetic, and pharmaceutical industries [143,144]. In spray drying, a precursor solution or nanosuspension is atomized (usually by pneumatic or pressure atomization), as the spray is being mixed with drying gas, and then the dry particles are collected.

Although electrospray drying has not been implemented industrially, it has proven to be able to make unique particles of potential use in many technological fields [13]. In particular, electrosprayed polymeric particles have attracted much pharmaceutical research [3,5,144], because of the promise of easy drug encapsulation and particle design.

The key processes that must be controlled in spray drying are solvent evaporation and solid phase formation. Solute concentration is expected to enrich at the droplet surface as solvent evaporates from it [143]. However, they explain that surface solute concentration will be reduced by solute transport to the droplet core, i.e. by diffusion (and, we may add, internal circulation, as well). Vehring et al. have developed a one-dimensional model which predicts solute concentrations versus radial position within the droplet. Shell formation is assumed to start happening at the surface of the droplet when the surface concentration exceeds the solute solubility concentration. However, their model is for small molecular weight compounds. In addition, they alert that crystallization is not immediate, due to the dynamics associated with crystal nucleation and growth.

A similar model to Vehring's does not exist for polymeric solutes. On the one hand, the diffusion coefficients of polymers are difficult to estimate, as they are highly dependent on molecular weight, as well as polymer chain conformation, and polymer concentration. Furthermore, the times needed for polymer chains to reach thermodynamic equilibrium may be large compared to the droplet drying time. In addition, the kinetics of polymer nucleation and growth of the glassy amorphous phase (vitrification) is not completely understood.

Some of the physics can be anticipated, however. As the solvent evaporates, the polymer will accumulate on the droplet surface, forming a rubbery skin, which can eventually vitrify (solidify forming a glassy skin) and grow into a shell by precipitation

of polymer from inside the droplet. The concentration of polymer on the surface is determined by the interplay between polymer accumulation due to drying (solvent evaporation) and diffusional transport of polymer from the droplet surface towards its core, which will depend on molecular weight, and perhaps internal droplet circulation. Yao et al. [145] explain shell formation in electro sprayed droplets of polymeric solutions as being due to diffusional-limited polymer accumulation at the droplet surface; while they explain compact particles as forming when diffusion is dominant. While generally agreeing with this picture for pharmaceutical microparticles formed by spray drying, Vehring et al. [143] caution that thin shells can form even when solute diffusion is dominant, if the solute is surface active. Clearly, Yao et al.'s model should be expanded to take into account the solubility of the polymer, and the rate of polymer vitrification.

In addition, in electrospray, the electrical charge on the droplets can cause coulombic instabilities during their drying. Such instabilities could result in the formation of nanoparticles, which will broaden the particle size distribution. In addition, exploding droplets can solidify while drying, especially when polymers are dissolved in the droplet. In this case, the instability may be slowed down due to the increase in viscosity and/or polymer chain entanglements. Therefore, the solvent can evaporate significantly from the emitted jet while the jet is forming, leading to polymer precipitation and the halting of the emission. Subsequently the droplet dries up. This scenario therefore leads to particles carrying thin filaments attached. Such particle geometry is often not desirable, especially for pharmaceutical applications. To avoid this scenario, some authors simply follow the approach of using the highest possible concentration to get non-exploded individual particles [136,146] have found that for PLGA in chloroform there is a range of concentrations over which spherical particles are found, and such range becomes narrower as the molecular weight of the polymer increases. However, Almería et al. [56] show that for a given polymer concentration, the liquid flow rate  $Q$  can be adjusted to preclude the coulombic instabilities. A reduction in  $Q$  lowers the initial charge-to-Rayleigh limit charge ratio ( $q/q_R$ ), and delays the coulombic instability to a later time in the droplet history. Therefore, when the concentration of polymer is high enough, polymer chain entanglements will prevent the coulombic instability, and filament-free particles will be formed [56].

Besides the variation of shapes due to Coulomb explosion, the morphology (surface structure) of electro spray particles is also diverse, from smooth to textured with highly porous surfaces and even with a hollow structure [5, 3]. The explanations given for the formation of the different morphologies are qualitative, and usually involve solvent properties only. One usual explanation is that fast solvent evaporation reduces the time needed for the polymer chains to re-arrange within the droplet during solidification [3,5,147]. However, we know from electrospinning literature that relative humidity in the ambient surrounding the fiber can lead to fiber porosity. Strangely, the role of this factor has almost not been highlighted in electro spray review literature (e.g. [3], [5]).

## 1.4. Thesis aims and structure

In electro spraying of polymeric solutions, important questions still remain open, which are addressed in this thesis. More specifically, these questions refer to the electro spraying of non-water soluble polymeric solutions in organic solvents, and are addressed in this thesis as follows:

1) The control over Rayleigh instability in electro sprays of polymeric solutions could be a powerful tool for particle engineering, whether the goal is spherical fiberless particles or particles with fibers. However, whereas the Rayleigh instability happens often in electro spray of volatile solvents, it is yet not sufficiently studied and explained in the case of polymeric solutions. Our aim is to identify the main factors and mechanisms leading to different morphologies in the presence of Rayleigh instabilities. In **Chapter 2** we address this goal, in an investigation over the formation of polymeric microparticles and nanoparticles by electro spray under low ambient humidity.

2) The use of vapors which are non-solvents for the polymer is another powerful tool for particle engineering. For many polymers water vapor in the spray can have a profound influence on the particle formation process and its nanostructure. Nevertheless, the non-solvent effects due to ambient humidity on the electro spraying of polymeric solutions has not been sufficiently studied, often not even recognized. In the closely related field of electro spinning, where the effect has been explained, there is still no consensus about how ambient humidity influences polymeric nanostructure formation. Our aim in **Chapter 3** is, therefore, to systematically study the effect of

ambient humidity on the particle morphology obtained by electro spraying dilute polymer solutions, and to provide interpretations of the mechanisms of formation based on thermodynamic and transport concepts.

3) Collecting dry polymeric particles made by electro spray onto solid substrates leads to the expansion of the granular film. This phenomenon, which has not been reported in the literature before this investigation, is studied in detail in **Chapter 4**. Here, we are interested in understanding the growth dynamics of such granular films (not only the expansion rate), as a function of key factors: deposition time, ambient humidity, and deposition flux. This study is focused on a single-electro spraying source or needle, but has important implications for multiplexed systems, where the deposition fluxes can be significantly larger.

All of the experiments reported in this thesis have been performed in the Sescelades Campus of Universitat Rovira i Virgili in Tarragona, Catalonia, Spain.

## 1.5. References

- [1] Loscertales, I. G., Barrero, A., Guerrero, I., Cortijo, R., Marquez, M., Gañán-Calvo, A. M. (2002). Micro/nano encapsulation via electrified coaxial liquid jets. *Science*, 295, 1695-1698.
- [2] Loscertales, I. G., Barrero, A., Márquez, M. (2004). Production of complex nano-structures by electro-hydro-dynamics. *Mater. Res. Soc. Symp. Proc.*, 860, LL5.9.
- [3] Bock, N., Dargaville, T. R., Woodruff, M. A. (2012). Electro spraying of polymers with therapeutic molecules: State of the art. *Progress in Polymer Science*, 37, 1510-1551.
- [4] Yurteri, C. U., Hartman, R. P. A., Marijnissen, J. C. M. (2010). Producing pharmaceutical particles via electro spraying with an emphasis on nano and nano structured particles - A Review. *KONA Powder and Particle Journal*, (28), 91-115.
- [5] Xie, J., Jiang, J., Davoodi, P., Srinivasan, M. P., Wang, C.-H. (2015). Electrohydrodynamic atomization: A two-decade effort to produce and process micro-/nanoparticulate materials. *Chemical Engineering Science*, 125, 32-57.
- [6] Fenn, J. B., Mann, M., Meng, C. K., Wong, S. F., and Whitehouse, C. M. (1989). Electro spray ionization for mass spectrometry of large biomolecules. *Science*, 246 (4926), 64-71.

- [7] Fenn, J. B. (2003). Electrospray wings for molecular elephants (Nobel Lecture). *Angew. Chem.-Int. Edit.*, 42(33), 3871-3894.
- [8] Zhu, J., Jiménez-Díaz, J., Bean, H. D., Daphtary, N. A., Aliyeva, M. I., Lundblad, L. K., Hill, J. E. (2013). Robust detection of *P. aeruginosa* and *S. aureus* acute lung infections by secondary electrospray ionization-mass spectrometry (SESI-MS) breathprinting: from initial infection to clearance. *J Breath Res.*, 7(3), 037106.
- [9] Barrios-Collado, C., Vidal-de-Miguel, G., Martínez-Lozano Sinues, P. (2016). Numerical modeling and experimental validation of a universal secondary electrospray ionization source for mass spectrometric gas analysis in real-time. *Sensors and Actuators B: Chemical*, 223, 217-225.
- [10] Lenggoro, I. W., Xia, B., Okuyama, K. (2002). Sizing of colloidal nanoparticles by electrospray and differential mobility analyzer methods. *Langmuir*, 18(12), 4584-4591.
- [11] Hogan, C. J., Kettleson, E. M., Ramaswami, B., Chen, D.-R., Biswas, P. (2006). charge reduced electrospray size spectrometry of mega- and gigadalton complexes: Whole viruses and virus fragments. *Analytical Chemistry*, 78(3), 844-852.
- [12] Okuyama, K., Lenggoro, I. W. (2003). Preparation of nanoparticles via spray route. *Chemical Engineering Science*, 58(3-6), 537-547.
- [13] Jaworek, A. (2007). Micro- and nanoparticle production by electrospraying. *Powder Technology*, 176(1), 18-35.
- [14] Almería, B., Gomez, A. (2014). Electrospray synthesis of monodisperse polymer particles in a broad (60 nm-2  $\mu$ m) diameter range: guiding principles and formulation recipes. *J. Colloid Interface Sci.*, 417, 121-130.
- [15] Chakraborty, S., Liao, I. C., Adler, A., Leong K. W. (2009). Electrohydrodynamics: A facile technique to fabricate drug delivery systems. *Adv. Drug Delivery Rev.*, 61(12), 1043-1054.
- [16] Larsen, G., Velarde-Ortiz, R., Minchow, K., Barrero, A., Loscertales, I. G. (2003). A method for making inorganic and hybrid (organic/inorganic) fibers and vesicles with diameters in the submicrometer and micrometer range via sol-gel chemistry and electrically forced liquid jets. *Journal of the American Chemical Society*, 125(5), 1154-1155.
- [17] Barrero, A., Loscertales, I. G. (2007). Micro and nanoparticles via capillary flows. *Ann. Rev. Fluid Mech.*, 39, 89-106.
- [18] Park, I., Kim, W., Kim, S. S. (2011). Multi-Jet mode electrospray for non-conducting fluids using two fluids and a coaxial grooved nozzle. *Aerosol Science and Technology*, 45(5), 629-634.

- [19] Xu, Q., Qin, H., Yin, Z., Hua, J., Pack, D. W., Wang, C.-H. (2013). Coaxial electrohydrodynamic atomization process for production of polymeric composite microspheres. *Chemical Engineering Science*, 104, 330-346.
- [20] Borra, J. P., Camelot, D., Chou, K.-L., Kooyman, P. J., Marijnissen, J. C. M., Scarlett, B. (1999). Bipolar coagulation for powder production: Micro-mixing inside droplets. *Journal of Aerosol Science*, 30(7), 945-958.
- [21] Jaworek, A. (2007). Electrospray droplet sources for thin film deposition. *J. Mater. Sci.*, 42, 266-297.
- [22] Umeda, M., Kawaguchi, S., Uchida, I. (2006). Characterization of Membrane Electrode Assembly for Fuel Cells Prepared by Electrostatic Spray Deposition. *Japanese Journal of Applied Physics*, 45(7R), 6049.
- [23] Martin, S., Garcia-Ybarra, P. L., Castillo, J. L. (2010). Electrospray deposition of catalyst layers with ultra-low Pt loadings for PEM fuel cells cathodes. *J. Power Sources*, 195, 2443-2449.
- [24] Ellis, N., Yurteri, C. U., Ruud van Ommen, J. (2012). Continuous process to deposit nanoparticles onto microparticles. *Chemical Engineering Journal*, 181-182, 798-805.
- [25] Cardoso, M. A. T., Talebi, M., Soares, P., Yurteri, C. U., van Ommen, J. R. (2011). Functionalization of lactose as a biological carrier for bovine serum albumin by electrospraying. *International Journal of Pharmaceutics*, 414(1-2), 1-5.
- [26] Morozov, V. N., Morozova, T. Ya. (1999). Electrospray deposition as a method for mass fabrication of mono- and multicomponent microarrays of biological and biologically active substances. *Anal. Chem.*, 71, 3110-3117.
- [27] Avseenko, N. V., Morozova, T. Y., Ataulkhanov, F. I., Morozov, V. N. (2002). Immunoassay with multicomponent protein microarrays fabricated by electrospray deposition. *Analytical Chemistry*, 74(5), 927-933.
- [28] Kim, J.-W., Yamagata, Y., Takasaki, M., Lee, B.-H., Ohmori, H., Higuchi, T. (2005). A device for fabricating protein chips by using a surface acoustic wave atomizer and electrostatic deposition. *Sensors and Actuators B: Chemical*, 107(2), 535-545.
- [29] Woo, C. G., Shin, H., Jeong, C., Jun, K., Lee, J., Lee, J.-R., Lee, H., You, S., Son, Y., Choi, M. (2011). Selective nanopatterning of protein via ion-induced focusing and its application to metal-enhanced fluorescence. *Small*, 7(13), 1790-1794.
- [30] Xie, J., Rezvanpour, A., Wang, C. W., Hua, J. (2010). Electric field controlled electrospray deposition for precise particle pattern and cell pattern formation. *AIChE Journal*, 56(10), 2607-2621.



- [31] Kim, H., Kim, J. Yang H., Suh J., Kim T., Han B., Kim S., Kim D. S., Pikhitsa P. V., Choi M. (2006). Parallel patterning of nanoparticles via electrodynamic focusing of charged aerosols. *Nature Nanotechnology*, 1(2), 117-121.
- [32] Lee, H., You, S., Woo C. G., Lim K., Jun K., Choi M. (2009). Focused patterning of nanoparticles by controlling electric field induced particle motion. *Appl. Phys. Lett.*, 94(5), 053104-3.
- [33] You, S., Han, K., Kim H., Lee H., Woo C. G., Jeong C., Nam W., Choi M. (2010). High-Resolution, Parallel Patterning of Nanoparticles via an Ion-Induced Focusing Mask (2010). *Small*, 6(19), 2146-2152.
- [34] Huang, Y., Bu, N. Duan Y., Pan Y., Liu H., Yin Z., Xiong Y. (2013). Electrohydrodynamic direct-writing. *Nanoscale*, 5(24), 12007-12017.
- [35] Onses, M. S., Sutanto, E., Ferreira, P. M., Alleyne, A. G., Rogers, J. A. (2015). Mechanisms, capabilities, and applications of high-resolution electrohydrodynamic jet printing. *Small*, 11, 4237-4266.
- [36] Li, D., Xia, Y. (2004). Electrospinning of Nanofibers: Reinventing the Wheel? *Advanced Materials*, 16(14), 1151-1170.
- [37] Greiner, A., Wendorff, J. H. (2007). Electrospinning: A Fascinating Method for the Preparation of Ultrathin Fibers. *Angew. Chemie Int. Ed.*, 46(30), 5670-5703.
- [38] Reneker, D. H., Yarin, A. L. (2008). Electrospinning jets and polymer nanofibers. *Polymer*, 49, 2387-2425.
- [39] Bhardwaj, N., Kundu, S. C. (2010). Electrospinning: A fascinating fiber fabrication technique. *Biotechnology Advances*, 28(3), 325-347.
- [40] Huang, Z.-M., Zhang, Y. Z., Kotaki, M., Ramakrishna, S. (2003). A review on polymer nanofibers by electrospinning and their applications in nanocomposites. *Composites Science and Technology*, 63(15), 2223-2253.
- [41] Agarwal, S., Wendorff, J. H., Greiner, A. (2008). Use of electrospinning technique for biomedical applications. *Polymer*, 49(26), 5603-5621.
- [42] Gamero-Castano, M., Hruby, V. (2001). Electro spray as a source of nanoparticles for efficient colloid thrusters. *Journal of Propulsion and Power*, 17(5), 977-987.
- [43] Morris, T., Forget, M., Malardier-Jugroot, C., Jugroot, M. (2011). Multi-scale investigation of a colloid micro-propulsion system. *Plasma Processes and Polymers*, 8(6), 478-489.
- [44] Orloff, J., Swanson, L., Utlaut, M. (2003). *High Resolution Focused Ion Beams: FIB and its Applications*. Springer, New York.

- [45] Romero-Sanz, I., Bocanegra, R., Fernandez de la Mora, J., Gamero-Castaño, M. (2003). Source of heavy molecular ions based on Taylor cones of ionic liquids operating in the pure ion evaporation regime. *Journal of Applied Physics*, 94(5), 3599-3605.
- [46] Gamero-Castaño, M., Mahadevan, M. (2009) Sputtering of silicon by a beamlet of electrospayed nanodroplets. *Appl. Surf. Sci.*, 255, 8556-8561.
- [47] Gamero-Castaño, M., Torrents, A., Valdevit, L., Zheng, J.-G. (2010). Pressure-Induced Amorphization in Silicon Caused by the Impact of Electrospayed Nanodroplets. *Phys. Rev. Lett.*, 105, 145701.
- [48] Borrajo-Pelaez, R., Grustan-Gutierrez, E. Gamero-Castaño, M. (2013). Sputtering of Si, SiC, InAs, InP, Ge, GaAs, GaSb, and GaN by electrospayed nanodroplets. *Journal of Applied Physics*, 114(18), 184304.
- [49] Jiang, L., Zhao, Y., Zhai, J. (2004). A lotus-leaf-like superhydrophobic surface: A porous microsphere/nanofiber composite film prepared by electrohydrodynamics. *Angewandte Chemie International Edition*, 43, 4338–4341.
- [50] Chen, C. H., Saville, D. A., Aksay, I. A. (2006). Electrohydrodynamic "drop-and-place" particle deployment. *Applied Physics Letters*, 88(15), 154104.
- [51] Tran, S. B. Q., Byun, D., Nguyen, V. D., Kang, T. S. (2009). Liquid meniscus oscillation and drop ejection by ac voltage, pulsed dc voltage, and superimposing dc to ac voltages. *Physical Review E*, 80(2), 026318.
- [52] Stachewicz, U., Dijksman, J. F., Burdinski, D., Yurteri, C. U., Marijnissen, J. C. M. (2009). Relaxation times in single event electrospaying controlled by nozzle front surface modification. *Langmuir*, 25(4), 2540-2549.
- [53] Stachewicz, U., Yurteri, C. U., Frits Dijksman, J., Marijnissen, J. C. M. (2010). Single event electrospaying of water. *Journal of Aerosol Science*, 41(10), 963-973.
- [54] Lee, M. W., Kang, D. K., Kim, N. Y., Kim, H. Y., James, S. C., Yoon, S. S. (2012). A study of ejection modes for pulsed-DC electrohydrodynamic inkjet printing. *Journal of Aerosol Science*, 46(4), 1-6.
- [55] Lee, S., Song, J., Kim, H., Chung, J. (2012). Time resolved imaging of electrohydrodynamic jetting on demand induced by square pulse voltage. *Journal of Aerosol Science*, 52, 89-97.
- [56] Almería, B., Deng, W., Fahmy, T. M., Gomez, A. (2010). Controlling the morphology of electrospay-generated PLGA microparticles for drug delivery. *Journal of Colloid and Interface Science*, 343, 125–133.
- [57] Almería, B., Fahmy, T. M., Gomez A. (2011). A multiplexed electrospay process for single-step synthesis of stabilized polymer particles for drug delivery. *Journal of Controlled Release*, 154(2), 203-210.

- [58] Kawakami, K. (2012). Miscibility analysis of particulate solid dispersions prepared by electrospray deposition. *International Journal of Pharmaceutics*, 433(1-2), 71-78.
- [59] Xiong, J., Zhou, Z., Ye, X., Wang, X., Feng, Y. (2002). A colloid micro-thruster system. *Microelectronic Engineering*, 61-62, 1031-1037.
- [60] Huberman, M. N., Beynon, J. C., Cohen, E., Goldin, D. S., Kidd, P.W., Zafran, S. (1968). Present status of colloid microthruster technology. *Journal of Spacecraft and Rockets*, 5, 1319-1324.
- [61] Kelly, R. T., Page, J. S., Tang, K., Smith, R. D. (2007). Array of chemically etched fused-silica emitters for improving the sensitivity and quantitation of electrospray ionization mass spectrometry. *Analytical Chemistry*, 79(11), 4192-4198.
- [62] Kelly, R. T., Page, J. S., Marginean, I., Tang, K., Smith, R. D. (2008). Nanoelectrospray emitter arrays providing interemitter electric field uniformity. *Analytical Chemistry*, 80(14), 5660-5665.
- [63] Kim, W., Guo, M., Yang, P., Wang, D. (2007). Microfabricated monolithic multinozzle emitters for nanoelectrospray mass spectrometry. *Analytical Chemistry*, 79(10), 3703-3707.
- [64] Wang, L., Stevens, R., Malik, A., Rockett, P., Paine, M., Adkin, P., Martyn, S., Smith, K., Stark, J., Dobson, P. (2007). High-aspect-ratio silica nozzle fabrication for nano-emitter electrospray applications. *Microelectronic Engineering*, 84(5-8), 1190-1193.
- [65] Lee, J.-S., Kim, S.-Y., Kim, Y.-J., Park, J., Kim, Y., Hwang, J., Kim, Y.-J. (2008). Design and evaluation of a silicon based multi-nozzle for addressable jetting using a controlled flow rate in electrohydrodynamic jet printing. *Appl. Phys. Lett.*, 93, 243114.
- [66] Sen, A. K., Darabi, J., Knapp, D. R. (2007). Simulation and parametric study of a novel multi-spray emitter for ESI-MS applications. *Microfluidics and Nanofluidics*, 3(3), 283-298.
- [67] Jaworek, A., Balachandran, W., Lackowski, M., Kulon, J., Krupa, A. (2006). Multi-nozzle electrospray system for gas cleaning processes. *Journal of Electrostatics*, 64, 194-202.
- [68] Smith, D. P. H. (1986). The Electrohydrodynamic atomization of liquids. *IEEE Transactions on Industry Applications*, 22(3), 527-535.
- [69] Cloupeau, M., Prunet-Foch, B. (1989). Electro spraying of liquids in cone-jet mode. *J. Electrostatics*, 22, 135-159.
- [70] Scheideler, W. J., Chen, C.-H. (2014). The minimum flow rate scaling of Taylor cone-jets issued from a nozzle. *Applied Physics Letters*, 104(2), 024103.

- [71] Gañán-Calvo, A. M., Rebollo-Muñoz, N., Montanero, J. M. (2013). The minimum or natural rate of flow and droplet size ejected by Taylor cone-jets: Physical symmetries and scaling laws. *New Journal of Physics*, 15, 033035.
- [72] Cloupeau, M., Prunet-Foch, B. (1990). Electrostatic spraying of liquids – Main functioning modes. *Journal of Electrostatics*, 25(2), 165-184.
- [73] Cloupeau, M., Prunet-Foch, B. (1994). Electrohydrodynamic spraying functioning modes: a critical review. *Journal of Aerosol Science*, 25(6), 1021-1036.
- [74] Jaworek, A., Krupa, A. (1999). Classification of the modes of EHD spraying. *Journal of Aerosol Science*, 30(7), 873-893.
- [75] Paine, M. D., Alexander, M. S. et al. (2007). Nozzle and liquid effects on the spray modes in nanoelectrospray. *Journal of Colloid and Interface Science*, 305(1), 111-123.
- [76] Marginean, I., Nemes, P., Vertes, A. (2007). A stable regime in electrosprays. *Physical Review E*, 76(2), 026320.
- [77] Verdoold, S., Agostinho, L. L. F. et al. (2014). A generic electrospray classification. *Journal of Aerosol Science*, 67, 87-103.
- [78] Borra, J. P., Camelot, D. et al. (1997). A new production process of powders with defined properties by electrohydrodynamic atomization of liquids and post-production electrical mixing. *Journal of Electrostatics*, 40-41, 633-638.
- [79] Borra, J.-P., Ehouarna, P., Boulaud, D. (2004). Electrohydrodynamic atomisation of water stabilised by glow discharge—operating range and droplet properties. *J. Aerosol Science*, 35, 1313–1332.
- [80] Taylor, G. I. (1964). Disintegration of water drops in electric field. *Proc. R. Soc. Lond. A*, 280, 383-397.
- [81] Fernández de la Mora, J. (1992). The effect of charge emission from electrified liquid cones. *Journal of Fluid Mechanics*, 243, 561-574.
- [82] Fernández de la Mora, J. (2007). The fluid dynamics of Taylor cones. *Annu. Rev. Fluid Mech.*, 39, 217-243.
- [83] Fernández de la Mora, J. F., Loscertales, I. G. (1994). The current emitted by highly conducting Taylor cones. *Journal of Fluid Mechanics* 260, 155-184.
- [84] Herrada, M. A., Lopez-Herrera, J. M., et al. (2012). Numerical simulation of electrospray in the cone-jet mode. *Physical Review E*, 86(2), 026305.
- [85] Higuera, F. J. (2003). Flow rate and electric current emitted by a Taylor cone. *J. Fluid Mech.*, 484, 303-327.

- [86] Gamero-Castaño, M. (2010). Energy dissipation in electrosprays and the geometric scaling of the transition region of cone-jets. *J. Fluid Mech.*, 662, 493–513.
- [87] Rosell-Llompart, J., Fernández de la Mora, J. (1994). Generation of monodisperse droplets 0.3 to 4 micrometre in diameter from electrified cone-jets of highly conducting and viscous liquids. *J. Aerosol Sci.*, 25, 1093-1119.
- [88] Chen, D.-R., Pui, D. Y. H. (1997). Experimental investigation of scaling laws for electrospraying: dielectric constant effect. *Aerosol Sci. Tech.*, 27(3), 367- 380.
- [89] Hartman, R. P. A., Brunner, D. J., Camelot, D. M. A., Marijnissen, J. C. M., Scarlett, B. (2000). Jet break-up in electrohydrodynamic atomization in the cone-jet mode. *Journal of Aerosol Science*, 31(1), 65-95.
- [90] Lenggoro, I. W., Okuyama, K., Fernández de la Mora, J., Tohge, N. (2000). Preparation of ZnS nanoparticles by electrospray pyrolysis. *Journal of Aerosol Science*, 31(1), 121-136.
- [91] Gañán-Calvo, A. M., Montanero, J. M. (2009). Revision of capillary cone-jet physics: Electrospray and flow focusing. *Phys. Rev. E*, 79, 066305.
- [92] Ieta, A., Gerlach, H. et al. (2009). Scaling law for electrospray droplet formation. *Particulate Science and Technology*, 27(3), 238-244.
- [93] Yan, F., Farouk, B. et al. (2003). Numerical modeling of an electrostatically driven liquid meniscus in the cone-jet mode. *Journal of Aerosol Science*, 34(1), 99-116.
- [94] Lastow, O., Balachandran, W. (2006). Numerical simulation of electrohydrodynamic (EHD) atomization. *Journal of Electrostatics*, 64(12), 850-859.
- [95] Higuera, F. J. (2009). Charge separation in the conical meniscus of an electrospray of a very polar liquid: Its effect on the minimum flow rate. *Physics of Fluids*, 21(3), 032104.
- [96] Higuera, F. J. (2010). Numerical computation of the domain of operation of an electrospray of a very viscous liquid. *Journal of Fluid Mechanics*, 648, 35-52.
- [97] Lim, L. K., Hua, J., Wang, C.-H., Smith, K. A. (2011). Numerical simulation of cone-jet formation in electrohydrodynamic atomization. *AIChE J.*, 57, 57–78.
- [98] Sarkar, K., Hoos, P., Urias, A. (2013). Numerical simulation of formation and distortion of Taylor cones. *J. Nanotechnology in Engineering and Medicine*, 3(4), 041001.
- [99] López-Herrera, J. M., Herrada, M. A. et al. (2013). On the validity and applicability of the one-dimensional approximation in cone-jet electrospray. *Journal of Aerosol Science*, 61, 60-69.

- [100] Eggers, J., Villermaux, E. (2008). Physics of liquid jets. *Rep. Progr. Phys.*, 71(3), 036601.
- [101] Eggers, J. (1997). Nonlinear dynamics and breakup of free-surface flows. *Rev. Mod. Phys.*, 69(3), 865-929.
- [102] Fong, H., Chun, I., Reneker, D. H. (1999). Beaded nanofibers formed during electrospinning. *Polymer*, 40(16), 4585-4592.
- [103] Rayleigh, L. (1878). On the instability of jets. *Proc. London Math. Soc.*, s1-10, 4-13.
- [104] Saville, D. A. (1997). Electrohydrodynamics: The Taylor-Melcher leaky dielectric model. *Ann. Rev. Fluid Mech.*, 29, 27-64.
- [105] Ashgriz, N., Mashayek, F. (1995). Temporal analysis of capillary jet breakup. *J. Fluid Mech.*, 291, 163-190.
- [106] Gamero-Castaño, M. (2008). The structure of electro spray beams in vacuum. *J. Fluid Mech.*, 604, 339-368.
- [107] Chandrasekhar, S. (1981). *Hydrodynamic and Hydromagnetic Stability*. Dover, New York.
- [108] Jones, A. R., Thong, K. C. (1971). The production of charged monodisperse fuel droplets by electrical dispersion. *J. Phys. D: Appl. Phys.*, 4, 1159-1166.
- [109] Tang, K., Gomez, A. (1994). On the structure of an electrostatic spray of monodisperse droplets. *Physics of Fluids*, 6(7), 2317-2332.
- [110] Gamero-Castano, M., Hruby, V. (2002). Electric measurements of charged sprays emitted by cone-jets. *Journal of Fluid Mechanics*, 459, 245-276.
- [111] Melcher, J. R. (1963). *Field-Coupled Surface Waves*. MIT, Cambridge, MA.
- [112] Riboux, G., Marín, Á. G. et al. (2011). Whipping instability characterization of an electrified visco-capillary jet. *Journal of Fluid Mechanics*, 671, 226-253.
- [113] de Juan, L., Fernández de la Mora, J. (1997). Charge and size distributions of electro spray drops. *Journal of Colloid and Interface Science*, 186(2), 280-293.
- [114] Hohman, M. M., Shin, M. et al. (2001). Electrospinning and electrically forced jets. II. Applications. *Physics of Fluids*, 13(8), 2221-2236.
- [115] Grifoll, J., Rosell-Llompart, J. (2012). Efficient Lagrangian simulation of electro spray droplets dynamics. *Journal of Aerosol Science*, 47, 78-93.
- [116] Zeleny, J. (1917) Instability of electrified liquid surfaces. *Phys. Rev.*, 10, 1-6.

- [117] Hartman, R. P. A., Borra, J. P., Brunner, D. J., Marijnissen, J. C. M., Scarlett, B. (1999). The evolution of electrohydrodynamic sprays produced in the cone-jet mode, a physical model. *Journal of Electrostatics*, 47, 143–170.
- [118] Wilhelm, O., Madler, L. (2006). Cone-jet and multijet electrosprays: Transport and evaporation. *Atomization and Sprays*, 16(1), 83-102.
- [119] Grifoll, J., Rosell-Llompart, J. (2015). Continuous droplets' charge method for the Lagrangian simulation of electrostatic sprays. *Journal of Electrostatics*, 72, 357-364.
- [120] Gañán-Calvo, A. M., Lasheras, J. C., Dávila, J., Barrero, A. (1994). The electrostatic spray emitted from an electrified conical meniscus. *J. Aerosol Sci.*, 25, 1121–1142.
- [121] Olumee, Z., Callahan, J. H., et al. (1998). Droplet dynamics changes in electrostatic sprays of methanol-water mixtures. *The Journal of Physical Chemistry A*, 102(46), 9154-9160.
- [122] Higuera, F. J. (2012). Eulerian model of a dilute spray of charged droplets. *Journal of Aerosol Science*, 48, 34-45.
- [123] Arumugham-Achari, A., Grifoll, J., Rosell-Llompart, J. (2013). Two-way coupled numerical simulation of electrospray with induced gas flow. *Journal of Aerosol Science*, 65, 121-133.
- [124] Higuera, F. J. (2013). Multifluid Eulerian model of an electrospray in a host gas. *J. Fluid Mech.*, 734, 363–386.
- [125] Arumugham-Achari, A., Grifoll, J., Rosell-Llompart, J. (2015). A comprehensive framework for the numerical simulation of evaporating electrosprays. *Aerosol Science and Technology*, 49(6), 436-448.
- [126] Willeke, K., Baron, P. A. (Eds.) (1993). *Aerosol Measurement*. VNR, New York.
- [127] Wilhelm, O., Mädler, L., Pratsinis, S. E. (2003). Electrospray evaporation and deposition. *J. Aerosol Sci.*, 34(7), 815–836.
- [128] Kiselev, P., Rosell, J., Fenn, J. B. (1997). Determining the composition of liquid droplets in a gas of different composition. *Ind. Eng. Chem. Res.*, 36(8), 3081-3084.
- [129] Gibson, S. C., Feigerle, C. S., Cook, K. D. (2013). Fluorometric measurement and modeling of droplet temperature changes in an electrospray plume. *Analytical Chemistry*, 86(1), 464-472.
- [130] Rayleigh, J. W. S. (1882). On the equilibrium of liquid conducting masses charged with electricity. *Phil. Mag.* 14, 184-186.
- [131] Rayleigh, J. W. S. (1945). *The Theory of Sound. Vol. II*. Dover, New York. Unabridged republication of the second edition of 1896.

- [132] Gomez, A., Tang, K. (1994). Charge and fission of droplets in electrostatic sprays. *Phys. Fluids A*, 6, 404-414.
- [133] Duft, D., Achtzehn, T., Müller, R., Huber, B. A., Leisner, T. (2003). Rayleigh jets from levitated microdroplets. *Nature*, 421, 128.
- [134] Achtzehn, T., Müller, R., Duft, D., Leisner, T. (2005). The Coulomb instability of charged microdroplets: dynamics and scaling. *Eur. Phys. J. D*, 34, 311–313.
- [135] Giglio, E., Gervais, B., Rangama, J., Manil, B., Huber, B. A., Duft, D., Müller, R., Leisner, T., Guet, C. (2008). Shape deformations of surface-charged microdroplets. *Physical Review E*, 77(3), 036319.
- [136] Meng, F., Jiang, Y., Sun, Z., Yin, Y., Li, Y. (2009). Electrohydrodynamic liquid atomization of biodegradable polymer microparticles: Effect of electrohydrodynamic liquid atomization variables on microparticles. *J. Appl. Polym. Sci.*, 113, 526-53.
- [137] Li, D., Marquez, M., Xia, Y. (2007). Capturing electrified nanodroplets under Rayleigh instability by coupling electrospray with a sol-gel reaction. *Chemical Physics Letters*, 445(4-6), 271-275.
- [138] Richardson, C. B., Pigg, A. L., Hightower, R. L. (1989). On the stability limit of charged droplets. *Proc. R. Soc. Lond. A*, 422, 319-328.
- [139] Smith, J. N., Flagan, R. C., Beauchamp, J. L. (2002). Droplet evaporation and discharge dynamics in electrospray ionization. *J. Phys. Chem. A*, 106(42), 9957-9967.
- [140] Hunter, H. C., Ray, A. K. (2009). On progeny droplets emitted during Coulombic fission of charged microdrops. *Physical Chemistry Chemical Physics*, 11(29), 6156-6165.
- [141] Grimm, R. L., Beauchamp, J. L. (2005). Dynamics of field-induced droplet ionization: Time-resolved studies of distortion, jetting, and progeny formation from charged and neutral methanol droplets exposed to strong electric fields. *The Journal of Physical Chemistry B*, 109(16), 8244-8250.
- [142] Fontelos, M. A., Kindelán, U., Vantzós, O. (2008). Evolution of neutral and charged droplets in an electric field. *Phys. Fluids.*, 20, 092110.
- [143] Vehring, R., Foss, W. R., Lechuga-Ballesteros, D. (2007). Particle formation in spray drying, *Aerosol Science* 38, 728 – 746.
- [144] Peltonen, L., Valo, H., Kolakovic, R., Laaksonen, T., Hirvonen, J. (2010). Electrospraying, spray drying and related techniques for production and formulation of drug nanoparticles *Expert Opin. Drug Deliv.* 7(6):705-719.



- [145] Yao, J., Lim, L. K., Xie, J., Hua, J., Wang, C.-H. (2008) Characterization of electro spraying process for polymeric particle fabrication, *Aerosol Science*, 39, 987-1002.
- [146] Fantini, D., Zanetti, M., Costa, L. (2006). Polystyrene Microspheres and Nanospheres Produced by Electro spray, *Macromolecular Rapid Communications*, 27(23), 2038–2042.
- [147] Park, C. H., Lee, J. (2009). Electro sprayed Polymer Particles: Effect of the Solvent Properties, *Journal of Applied Polymer Science*, 114, 430-437.

## **2. Polymeric microparticles and nanoparticles by electrospaying**

### **2.1. Introduction**

Electrospray (ES) is often portrayed as a unique and facile method to produce monodisperse micro- and nano-particles from liquid solutions comprising precursor solutes. One important challenge in ES is to understand the conditions leading to different particle morphologies, and specifically spherical or globular particles, which are of interest to different applications [1, 2]. In the electrospay process, the electrical stresses overcome the surface tension forces that resist its atomization into droplets, pulling a liquid meniscus into a Taylor cone and a microjet which breaks up into a fine spray (atomize). Typically this process is sustained in steady state by continuously flowing liquid solution through a tube held at a high electrical potential relative to its surroundings. The key to obtaining monodisperse size particles is controlling the mode of microjet breakup. The mode of greatest interest is the Rayleigh mode, where axisymmetric “varicose” waves develop on the jet surface leading to main droplets, and, often satellite droplets. The satellite droplets segregate spontaneously to the periphery of the spray soon after forming, due to an electrostatic/inertial separation process [3, 4]. Therefore, nearly monodisperse droplets can be sampled from the center of the spray by excluding the region occupied by satellite droplets. However, this is not the only mode in which the jet can break up [5].

In addition the charge that is necessary to form small monodisperse droplets causes later on Rayleigh instability in the droplets as they lose solvent by evaporation, which leads to droplet fragmentation (called coulombic fissions or Coulomb explosions) [56]. Filaments from the exploding droplets can release smaller droplets which lead to smaller polymer residues, which upset the initial monodisperse size distribution of the droplets.

Furthermore, the instability happens by the emission of one or two small filaments which can dry up in the process, leading to solute residues or particles which have a filament or tail. Studies with high molecular weight linear polymers (few hundred kDa) show that nearly spherical particles are accompanied by thin nanofilaments [6, 7]. These have been interpreted as incomplete jet breakup [6, 7]. Other times, particles without such tails are obtained, because the polymer precipitates out on the surface of the evaporating electrospray droplets, thus stabilizing them against (and preventing) coulombic fission. Therefore, controlling the appearance of filaments requires understanding which phenomena compete against their formation.

In addition evaporation from the surface of the cone (and the jet) may lead to significant increase in polymer concentration. In the case of polymer solutions, solvent evaporation from the jet, may lead to increased viscoelasticity, which may prevent the jet breakup forming beaded fibers (or beads connected by thin filaments) instead of droplets. A direct demonstration of this are the experiment of Larsen et al [8] in which the addition of solvent vapor co-flow around the Taylor cone changes the particle morphology, from beaded fibers to individual particles.

Meng et al [9] have found that for PLGA in chloroform there is a range of concentrations over which spherical particles are found, and such range becomes narrower as the molecular weight of the polymer increases. Almeria et al. [10] have shown that flow rate and initial polymer chain entanglements (dependent on the polymer, the molecular weight and the concentration) determine, whether spherical particles can be formed. Yao et al [11] argue that the formation of a shell is favored when the Brownian diffusion time of the polymer is small enough so that it cannot diffuse as the droplet evaporates.

In conclusion, the morphologies are diverse, and the phenomena involved are complex. Therefore, in this work we aim to interpret the mechanisms leading to the different

morphologies of micro-particles which are formed in electro-hydrodynamic atomizations of dilute solutions of polymers, specifically water-insoluble amorphous linear homopolymers. The main factors influencing particle morphology are the polymer, the polymer molecular weight, the solvent, and the initial (solution) polymer concentration. The effects of these factors on the morphology of the collected microparticles are explained in terms of the dominant transport and phase-change phenomena involved, and to deduce which regime they formed in: (I) incomplete jet break up, (II) precipitation in spherical (stable) droplets, (III) precipitation during a coulombic instability, (IV) precipitation after a coulombic fission.

The polymers chosen in this study are polystyrene (PS), poly(methyl methacrylate) (PMMA), and ethyl cellulose (EC). “Low” and “high” molecular weights are used for each polymer, from about 15 kDa to few hundred kDa, in order to have different polymer-chain entanglement dynamics, and different Brownian diffusion speeds of the polymer chains in the liquid phase. Butanone (MEK) and dichloromethane (DCM) have been chosen as solvents, since their different boiling points and polarity should lead, respectively, to widely different evaporation rates and polymer-solvent interactions.

Critical to these experiments are (1) the use of dry ambient conditions (near zero relative humidity), and (2) the use of a co-flow of solvent-vapor-laden gas around the nozzle (following Larsen et al. [8]). Elevating the ambient relative humidity can critically change the morphology of the particles formed, and such effects will be described in Chapter-3. The use of co-flow prevents premature polymer precipitation at the nozzle, ensuring perfectly stable jetting conditions.

## **2.2. Materials and Methods**

### **2.2.1. Materials**

Polystyrene, PS (Mw=350,000 and 35,000), Poly(methyl methacrylate), (Mw=350,000 and 15,000), Ethyl cellulose, EC (48% ethoxyl content, 100 cP viscosity grade, Mw~220,000 and 48% ethoxyl content, 4 cP viscosity grade, Mw~15-20,000 [12, 13]) were purchased from Sigma-Aldrich and used without further purification. ACS grade butanone (MEK) and reagent grade dichloromethane (DCM) (stabilized with ethanol -

0.3 v%) were purchased from Scharlau. We added rhodamine 6G to the DCM solutions (Rh6G, Sigma-Aldrich) at 1:1250 Rh6G:polymer weight ratio to raise the electrical conductivity of the solution. Some polymer properties can be found in Table 2-1. Polymeric solutions of different concentrations (100, 50, 30, 10 and 2 mg/ml solvent) were prepared at room temperature and stirred with magnetic stirrer for at least 6 hours. After preparation the solutions were stored at room temperature. The electrical conductivities of the solutions (shown in Table 2-2 in section 2.3.3) were determined by measuring the current through a Teflon tubing (length: 120mm, ID: 0.254mm) filled with our solutions when applying a voltage difference (~30 V) between the two ends of the tube.

**Table 2-1** Some polymer properties

	entanglement molecular weight  M <sub>c</sub> (Da)	density @ 25 °C <sup>c</sup>  ρ (g/ml)	glass transition temperature <sup>c</sup>  T <sub>G</sub> (°C)	Mark-Houwink parameters in MEK		interaction parameter with MEK
				K (10 <sup>-3</sup> )	a	χ
PMMA	13600 <sup>a</sup>	1.16	105	6.8 <sup>d</sup>	0.72 <sup>d</sup>	0.46-0.47 <sup>g</sup>
EC	7830 <sup>b*</sup>	1.14	129	18.2 <sup>e</sup>	0.84 <sup>e</sup>	0.42 <sup>e</sup>
PS	16600 <sup>a</sup>	1.04	95	39 <sup>f</sup>	0.58 <sup>f</sup>	0.478 <sup>h</sup>

<sup>a</sup> [14]; <sup>b</sup> [41]; \*EC with 46wt% ethoxyl content; <sup>c</sup> supplier information; <sup>d</sup> [42]; <sup>e</sup> [16]; <sup>f</sup> [43]; <sup>g</sup> [15]; <sup>h</sup> [44]

## 2.2.2. Electrospaying

A schematic diagram of the electrospaying arrangement and a picture of a working needle with co-flow are shown in Figure 2-1(a) and (b). We electrospayed in a chamber of glass walls and a methacrylate top plate. The glass walls define a square top-view section of about 10cm x 10 cm. The setup rested on an aluminium bottom plate. We introduced and dispersed dry N<sub>2</sub> (Carbueros Metálicos, Premier grade) flow into the chamber at ~0.5 slpm at the top of the chamber. Chamber humidity was monitored using a Vaisala HM34 meter probe inserted through the bottom plate. A syringe pump (HARVARD Apparatus) was used to generate liquid flow. Polymeric solutions were sprayed typically at a flow rate of 2 μL/min. The needle was a square-terminated stainless steel needle (400 μm OD, 165 μm ID), and the tip was polished with diamond paste (Figure-2.1(b)), which was passed through a tee and was centered in a glass capillary (ID:1.16 mm) from which the needle protruded by ~0.22 mm. Nitrogen gas

containing (saturated with) solvent vapor flowed through the tee to create a sheath flow around the silica capillary of  $\sim 18$  cc/min (linear exit gas velocity near needle  $\sim 340$  mm/s). The distance between needle and collector plate was 20 mm. Positive high voltage from a HV power supply (Ultravolt HV-RACK-4-250-00228) was applied to the SS capillary. An additional electrode ('back plate/electrode'), a 10 cm diameter circular brass plate was placed 17 mm behind the needle end and connected to the same potential as the needle. The back electrode contained twenty 3 mm holes, letting the chamber flow go through, but the  $N_2$  also flowed through the spaces between the brass plate and the chamber walls. The holes did not change the electric field. The bottom aluminium plate was connected to a home-made nanoammeter. The signal from the nanoammeter and the applied voltage was recorded with a National Instrument data acquisition board (NI-DAQ-PCI6221).

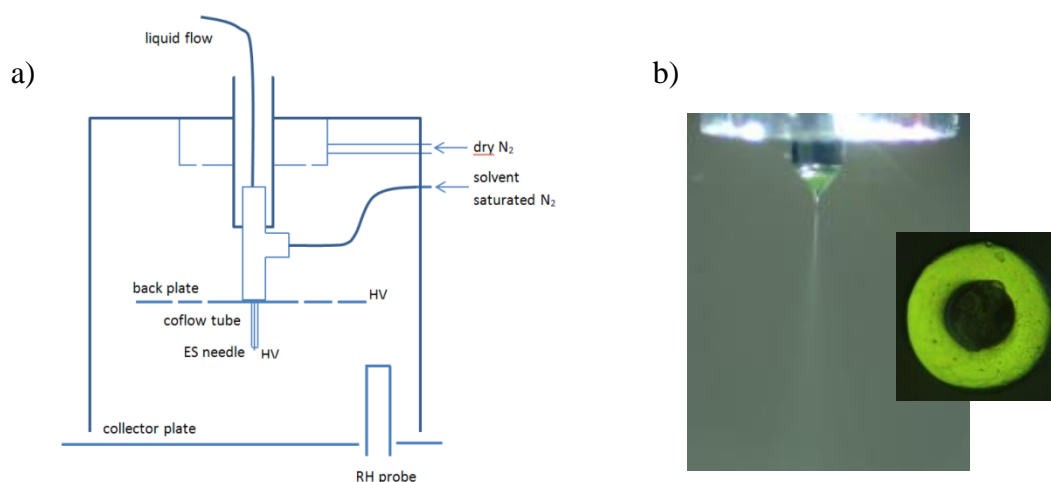


**Figure 2-1** Electro spray setup, a) chamber, b) ES needle with co-flow exit during ES, and photo of the polished needle end, needle OD: 400  $\mu$ m.

Some ancillary tests were done in the same chamber, but with a different needle configuration. The needle was a square-cut polyimide-coated fused-silica tubing (OD = 200  $\mu$ m, ID = 100  $\mu$ m, length  $\sim 80$  mm). (Results shown in Figures 2-11(b,c) and 2-12 (b,c).)

### 2.2.3. Particle collection and imaging

The particles/polymeric residues were collected on pieces of silicon wafer (SiMat, prime grade, P/Boron, <100>, 500  $\mu\text{m}$  thickness, 1-30  $\text{ohm}\cdot\text{cm}$ ) of approximately 20x20 mm size. The collection time was 10 seconds ( $\pm 1\text{s}$ ), unless noted otherwise. The Si wafers were slid under the spray during stable ES conditions (without disturbing the cone-jet) and then pushed rapidly away to terminate the collection.

All samples were gold coated ( $\sim 10\text{ nm}$ ) for SEM imaging and imaged at different locations in the collection spot, using a Quanta 650 apparatus (run typ. at 30kV,  $\sim 10\text{ mm}$  working distance).

## 2.3. Results

### 2.3.1. Terminology

In order to properly identify and classify the different particle morphologies observed by SEM, we find it necessary to define terminology that does not presume the mechanism of formation. Whenever possible, we choose terminology that is already widely accepted in the electrospray, electrospinning, and fluid dynamics literatures (see Chapter-1).

#### 2.3.1.1. *Particle kinds arising from jet break up*

The term *particle* is reserved to individual solid objects, namely unconnected to other particles (except for contact points formed on arrival at the collector). The largest particles in a deposit are here called *main particles*. We will assume that *main particles* evolve from the *main droplets* that form by breakup of the EHD microjet that is emitted from the Taylor cone (see Chapter-1). The term *main droplets* is used for the droplets that arise from the swells in the breakup of free-surface flows [17], of which EHD microjets are an example.

The term *beaded fibers* is used here to describe the solid structure made of globular volumes, or *beads*, connected by solid fibers. This meaning is common in the electrospinning field [18, 19], where beaded fibers's use for material nano-

encapsulation is widely known [20]. EHD polymeric jets produce beaded fibers by solidification while undergoing axisymmetric capillary instability. The corresponding fluid structure is called the *beads-on-string* structure [17]. The fluid bulges are the *beads*, which form by the growth of the *crests/swells* of the capillary wave responsible for the breakup of the jet, while the fibers develop from the *nodes* of the wave [17]. Therefore the term *bead* may be used to refer to a solid or a liquid structure. By *beading* we refer to the formation of a beads-on-string structure.

Smaller beads can grow on a liquid filament that strands two larger beads. The larger beads will be called *main beads*, and the smaller ones *secondary beads*. Here, the term *secondary* again parallels usage in the fluid dynamics literature: During axisymmetric break up of a neutral jet, *secondary swellings* can develop between two main swells of the capillary wave, resulting in satellite droplets in the case of Newtonian liquids [17, 21]. Secondary, as well as tertiary and higher order swells, can also develop during elastocapillary thinning of liquid bridges of high molecular weight polymer solutions [22].

The term *fiber* is used to describe a solid fiber, while the liquid structure that dried into this fiber is called *filament* or *bridge*, or *jet*. A filament is formed by an extensional flow driven by surface tension stresses, which cause liquid mass flow into two opposite directions (along the filament). On the other hand, a jet is a mass which is ejected from a reservoir of larger size, for example, during a Coulomb fission of an electrically charged drop.

### 2.3.1.2. *Coulombic instability vs. fission, and progeny particle*

*Coulombic instability* is used to refer to the fluid motions that occur to an electrically charged droplet when, as a result of solvent evaporation, the electrical stresses overcome the capillary stresses. This instability is also referred in the literature as the *Rayleigh instability* in honor of Lord Rayleigh, for his linear stability analysis of the problem (Chapter-1). We use the term *coulombic instability* instead, in order to avoid confusion with the Rayleigh mode of jet breakup. A coulombic instability can be called a *Coulomb explosion* or *Coulomb fission* when it results in the fragmentation of the unstable droplet, typically through development of a jet of diameter substantially smaller than the droplet diameter, and subsequent breaking of this jet into smaller



droplets, so called *progeny droplets* (or *offspring droplets*) (Chapter-1). Progeny droplets could in principle undergo further subdivision by the same pathway. Particles which form by drying of progeny droplets are here called *progeny particles*. When a droplet undergoes coulombic fission while in electrophoretic motion, all of the droplet fragments will follow nearby trajectories. As a result main and progeny particles will be collected in substantially the same regions of the collection substrate.

### **2.3.2. Effects due to the solvent vapor jacket**

Long term stability of the Taylor cone is essential for extended deposition experiments. The use of the solvent vapor jacket, as used by Larsen et al. [8] (Fig. 2-1) helped stabilize the EHD jetting process against drying at the meniscus. The effect was critical when using high concentration solutions of high molecular weight polymers. Figure 2-2 shows how turning off and back on the solvent vapor co-flow affected the Taylor cone, for the PMMA 350kDa 5% w/v MEK solution. Starting from the steady state, 46 s after turning off the co-flow the meniscus has evolved several filaments (Figure 2-2(b)). The two filaments on the left side are dry, while the one on the left is the liquid jet. The steady state is fully recovered after restarting the co-flow (at  $t = 2'16''$ ), as shown in (Figure 2-2(d)). The other concentrated solutions in MEK used in this work did not recover reversibly (Figure 2-2(e-k)).

Co-flow was not necessary to stabilize low molecular weight PMMA and PS solutions at any concentration. However, it was critical for the 15 kDa EC solution at 5% w/v, since the contact line of the Taylor cone moved from the outer rim of the steel needle (Figure 2-2(b-r)), perhaps because this polymer requires much lower concentration for gelling than PMMA or PS.

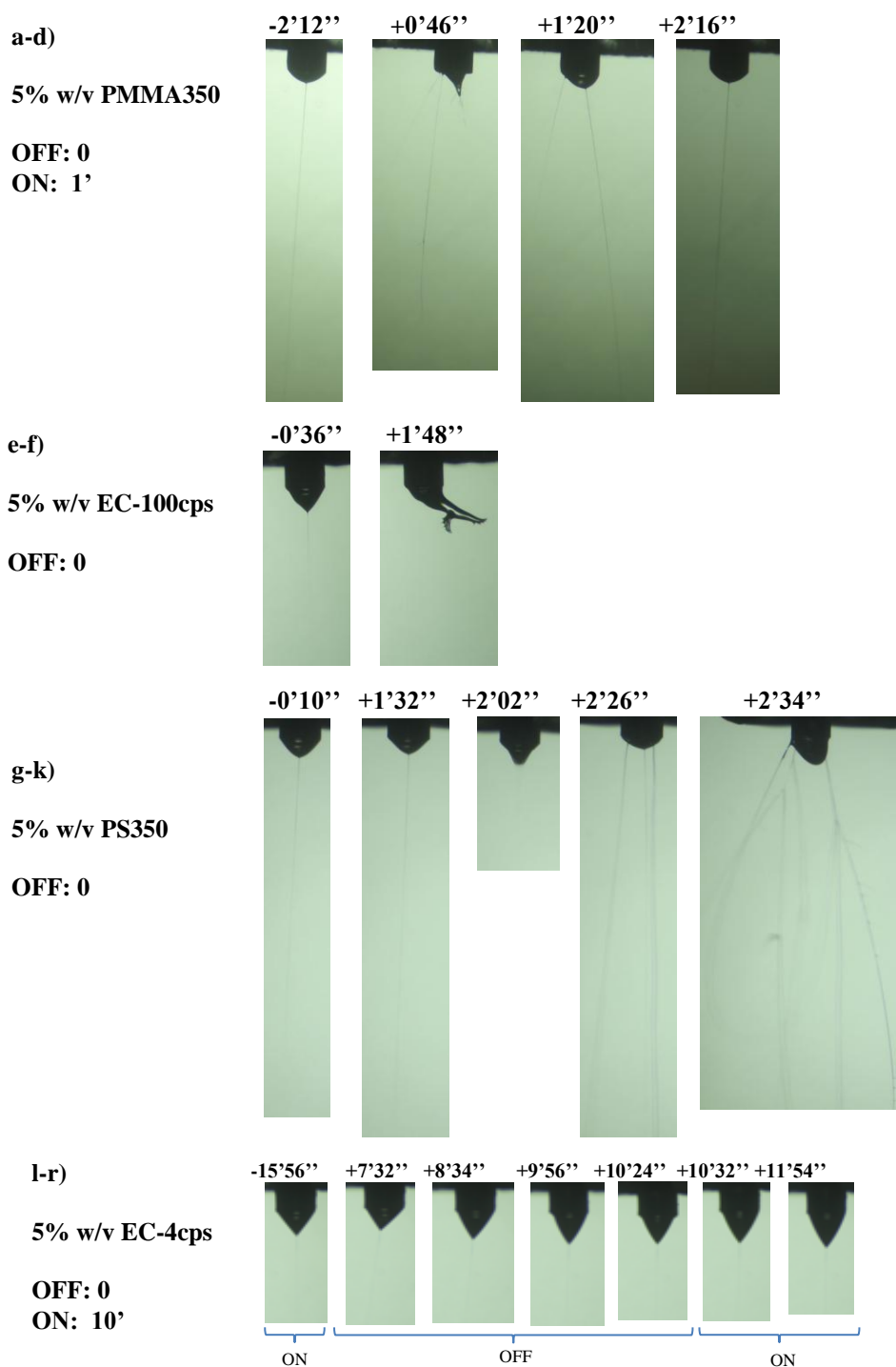


**Figure 2-2** Effect of co-flow on Taylor cone for various solutions in MEK. Co-flow is turned off at time 0 (OFF: 0) and back on at the indicated times (ON: ).

Aside from stabilizing the Taylor cone, the solvent co-flow also reduces solvent evaporation from the jet, keeping its viscosity lower. Small changes in viscosity and viscoelasticity can have a noticeable effect on the jet length, and breakup pattern, as schematically represented in Figure 1-2 and explained in Chapter-1. Without co-flow, in

our high initial concentration solutions of high molecular weight PMMA and PS in MEK, the jet did not break up, resulting in the formation of numerous fibers and beads to which the fibers are attached, as shown in Fig. 2-3(a-b). Secondary beading is extensive. With co-flow the fibers either disappear completely (PS) or become much thinner and appear broken (PMMA) (Fig. 2-3(c-d)). Fiber breakage could be caused by the pull the fibers experience as the main beads drift apart in the “spray” impelled by electrostatic repulsion. We should note incidentally that the beads are deflated, indicating that a polymer glassy layer grew out of the liquid-gas interface on the droplet or bead. However, the mechanical properties of such layers are different for PS, which collapsed into raisin-like shapes, and PMMA, which produced a cup-like (or bowl-like) shape.

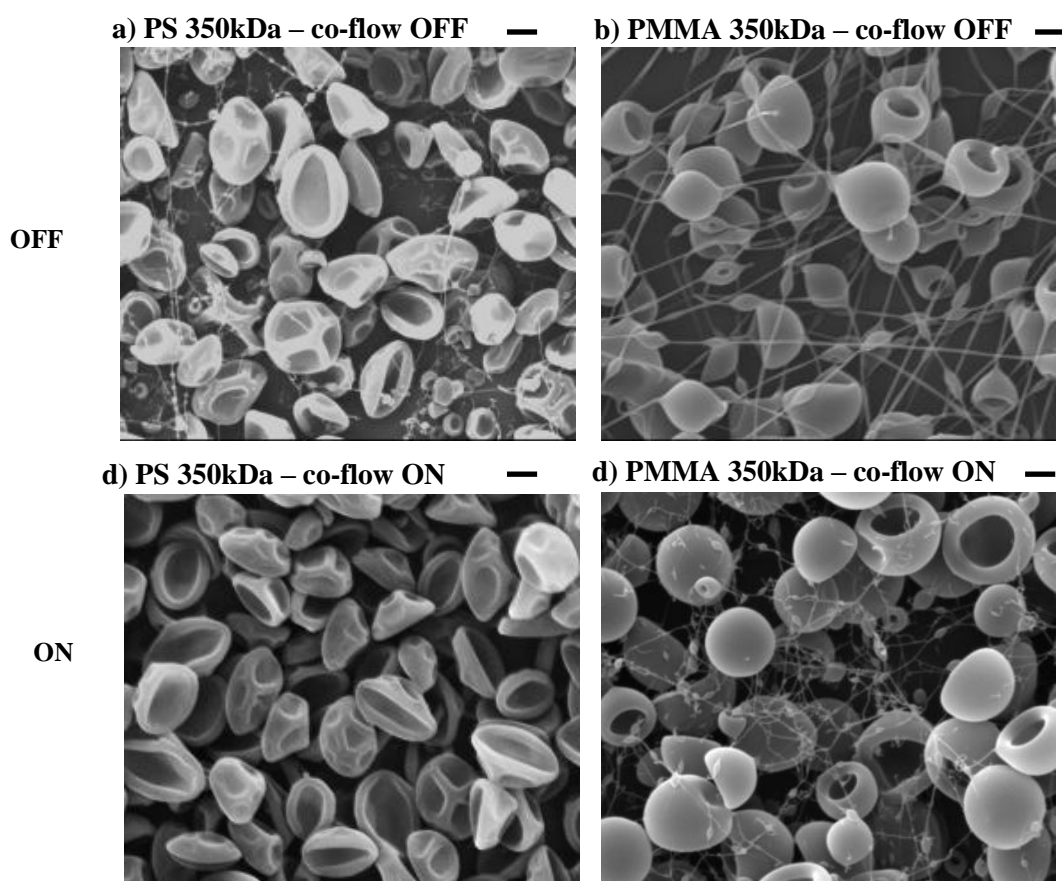


**Figure 2-3** Effect of co-flow on jet break-up in the case of high  $M_w$  5% w/v a,c) PS and b,d) PMMA; scale bars: 1  $\mu\text{m}$ .

Figure 2-4 shows the effect of the use of solvent co-flow for two concentrated low polymer molecular weight solutions. As will be proved later, the fibers we see in these pictures are formed by drying of nanojets ejected from main drops undergoing

coulombic instabilities. When co-flow is used, the frequency of such fibers is *increased* in both cases. The reason is that the concentration of polymer is high enough when co-flow is not used to prevent the development of the coulombic instability (formation of nanojets). We should note that, from an engineering point of view, if one desires to reduce the number of fibers, one should not turn off the co-flow but increase the initial polymer concentration, achieving the same result.

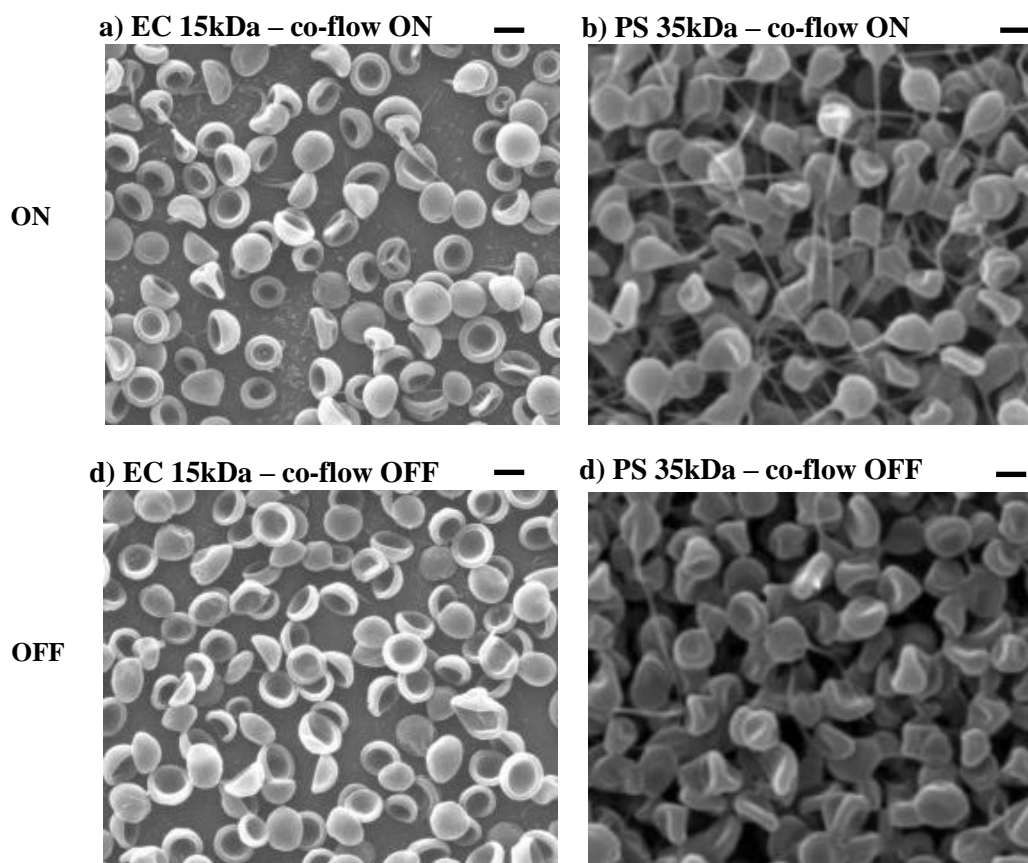


**Figure 2-4** Effect of co-flow on jet particle morphology in the case of low  $M_w$  5% w/v a,c) EC and b,d) PS; scale bars: 1  $\mu\text{m}$ .

### 2.3.3. Particle morphologies vs. initial concentration

Particle morphologies were obtained for different polymers and concentrations in MEK. Ancillary experiments with DCM were also performed, but for fewer polymer concentrations. Solutions were electrospayed at 2  $\mu\text{L}/\text{min}$  flow rate, except in the cases, where it became necessary to increase the flow rate to attain stable cone-jetting. During electrospaying, solvent-saturated co-flow (gas jacket) was provided around the

meniscus. The particles were collected on clean silicon wafers for 10 seconds, unless noted.

**Table 2-2** Solution properties and electro spray conditions.

	polymer concentration $C_0$ (mg/ml solvent)	electrical conductivity		solution flow rate Q ( $\mu$ l/min)	temperature T ( $^{\circ}$ C)	applied voltage V (kV)	measured electrospray current I (nA)	estimated from charge relaxation model [23] <sup>a</sup>	
		at						current $I_{FL}$ (nA)	droplet size $d_{FL}$ ( $\mu$ m)
		T	K						
		( $^{\circ}$ C)	( $\mu$ S/m)						
PMMA-350-MEK	50	25	56	2	23	6	6	16.2	4.60
PMMA-350-MEK	30	25	52	2	27.1	6.6	10	15.6	4.72
PMMA-350-MEK	10	25	48	2	27.1	7.9	15	15.0	4.84
PMMA-350-MEK	2	25	32	2	27.1	10	10	12.3	5.55
PMMA-15-MEK	50	25	143	2	23	7.5	26	25.9	3.37
PMMA-15-MEK	10	25	88	2	27.1	7.5	20	20.3	3.96
PMMA-15-MEK	2	25	56	2	27.1	6.6	15.5	16.2	4.60
EC-220-MEK	50	23.5	593	2	21.8	7.5	50	52.7	2.10
EC-220-MEK	10	2.35	96	2	26.7	8.2	27	21.2	3.85
EC-220-MEK	2	23.5	72	2	26.7	9.4	12	18.4	4.23
EC-15-MEK	50	25	247	2	21.8	6	34	34.0	2.81
PS-350-MEK	50	25	32	2	26.2	8	8	12.3	5.55
PS-350-MEK	10	25	40	2.5	26.7	8.9	9	15.3	5.55
PS-350-MEK	2	25	32	3.5	26.7	10.5	14	16.2	6.68
PS-35-MEK	100	22	42	2	26.7	9.7	10	14.0	5.07
PS-35-MEK	50	22	63	2	24	6.2	13.5	17.2	4.42
PS-35-MEK	10	22	59	2	26.3	6	12	16.6	4.52
PS-35-MEK	2	22	63	2	26.7	7.7	12	17.2	4.42
EC-15-DCM	50	22.5	47	2	26.3	7.0	13	13.4	3.83
PS-35-DCM	50	22.5	56	2	26.3	6.7	18	15.5	3.47

<sup>a</sup> For the computations we have used the measured electrical conductivity of our solutions, and other properties have been assumed equal to those of the pure solvent, at 20  $^{\circ}$ C.  $d_{FL}$  and  $I_{FL}$  are computed using eqs. (1-1) and (1-2).

The particle deposits onto the silicon wafers were round and white, indicating a dry deposit, or had a small wet center, as described later below. The outer edge of the zone populated by main particles disappeared over a few tens of microns, as inspected by SEM. The characterization of the particle morphologies observed by SEM as a function of polymer concentrations is a powerful methodology for ruling out morphology formation pathways. For example, knowledge that the EHD microjet breaks up implies that the jets from more dilute solutions (at same liquid flow) must do so as well. Therefore, fibers encountered with such dilute solutions are more likely to be formed during coulombic instabilities, than as string-on-bead structures arising during jet instability.

### 2.3.3.1. Poly(methyl)methacrylate morphologies from MEK solutions

#### 350 kDa PMMA / MEK

Figure 2-5 shows the morphologies obtained from PMMA/MEK solutions corresponding to the high molecular weight (350 kDa) PMMA solutions, and Figure 2-6 corresponding to our low molecular weight (15 kDa) solutions. The similar current and conductivity values from these solutions suggest very similar initial droplet size (Table 2-2).

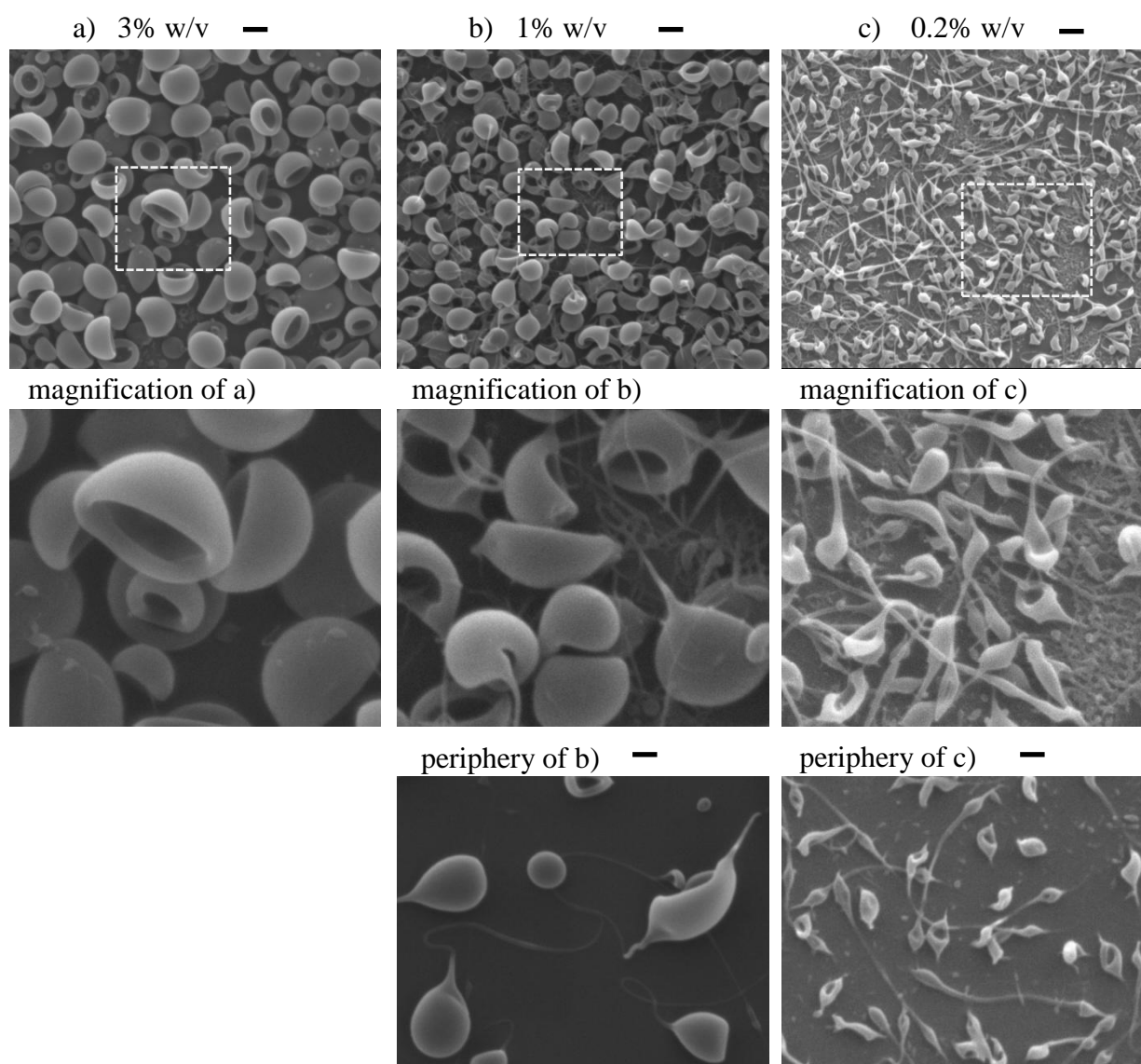


**Figure 2-5** Particle morphologies obtained from 350 kDa PMMA/MEK solutions; scale bars: 1 μm.

Recalling Fig. 2-3(d), PMMA-350 at the highest polymer concentration tested of 5% w/v produced relatively “large” beads surrounded by very thin fibers (of about 50 nm in diameter). Some of these fibers presented secondary beads. Figure 2-5 shows the sequence as  $c_0$  is decreased from this value. At 3% w/v (Fig. 2-5(a)) only similarly sized particles are formed, indicating that the jet break up occurred in Rayleigh mode. The absence of any fibers further indicates that these particles did not become coulombically unstable during solvent evaporation.

At  $c_0 = 1\%$  w/v (Fig. 2-5(b)), mostly main particles connected to one thin fiber are formed, and many of these particles are elongated in the direction of the fiber. At  $c_0 = 0.2\%$  w/v (Fig. 2-5(c)), most main particles are attached to fibers, however, mixed shapes appear. In addition, these main particles are surrounded by much smaller nanoparticles. These are very numerous, consistently with being progeny particles produced in Coulomb fission events. The small progeny particles are connected by very thin nanofibers, which may mean that for this high molecular weight PMMA, the solution could be entangled at the moment of coulombic instability not letting the progeny beads separate into droplets. It is interesting that these nanoparticles accumulate in the spaces between main particles, as if their trajectories were electrostatically segregated from those of the main particles down to the moment of impact with the collection surface.

The fibers in this sample (Fig. 2-5(c)) are thicker than those found at higher  $c_0$  (Fig. 2-5(b)). In addition, the fibers are connected to typically two particles, suggesting that the two formed by splitting of an original particle. In these cases, the two connected particles often present pointed ends on the “outer” sides. In addition, some fibers present a secondary bead. Taken together, these morphological features suggest very different fiber formation mechanisms from these two solutions.

#### *15 kDa PMMA / MEK*

The solutions with 15 kDa PMMA (Fig. 2-6(a-c)) produced fiber-free main particles (predominantly), whose size decreases with decreasing initial polymer concentration, as expected for similar initial droplet sizes (Table 2-2). A small fraction of the main particles hold a fiber. For the two most dilute solutions (Fig. 2-6(b-c)), the main particles are surrounded by numerous nanoparticles, whose size scales with the main particle size. The presence of two particle sizes modes, and the much greater relative

abundance of the smaller particles prove that these nanoparticles are relics from progeny droplets in Coulomb fission events, as seen for high molecular weight case in Fig. 2-5(c).

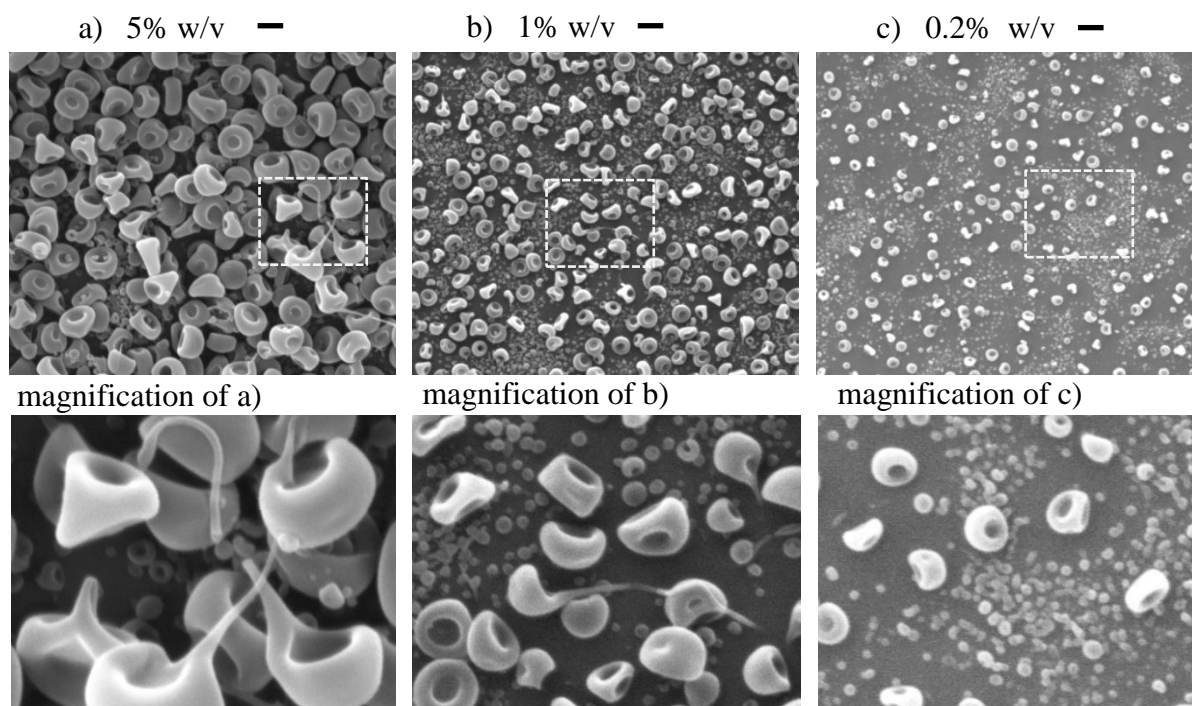


**Figure 2-6** Particle morphologies obtained from 15 kDa PMMA/MEK solutions; scale bars: 1  $\mu\text{m}$ .

### 2.3.3.2. *Polystyrene morphologies from MEK and DCM solutions*

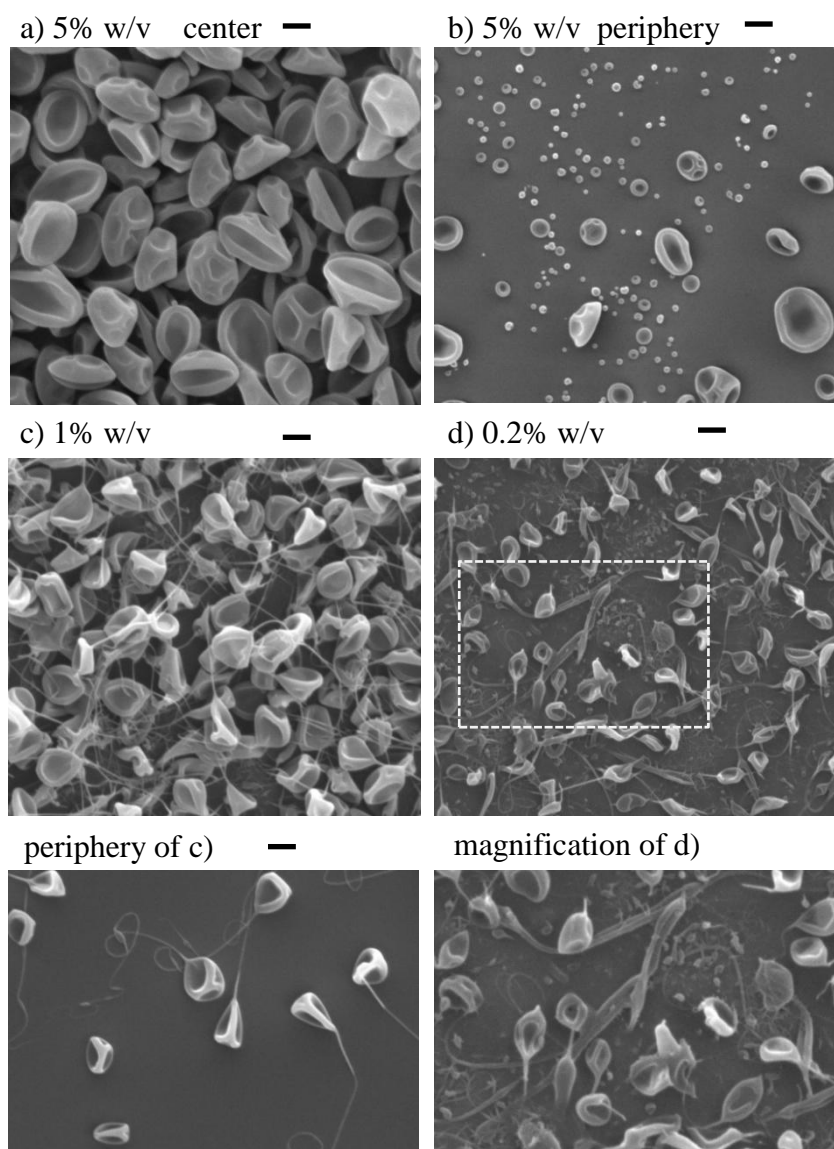
#### *350 kDa PS / MEK*

Figure 2-7 shows the morphologies obtained from high molecular weight (350 kDa) PS/MEK solutions, The electrospray was run at 2  $\mu\text{L}/\text{min}$ , except for 1 w/v% and 0.2% w/v cases, for which the flow rate was raised in order to attain stable conditions. This means that in these cases the flow rate was close to the minimum stable value ( $Q_{\text{min}}$ ; see Chapter 1). However, because of the higher flow rate, the deposits had a wet center surrounded by a white band containing dry main particles. In these cases, the images are from this band.

Turning off the solvent vapor co-flow resulted in incomplete jet breakup for the 5% w/v PS-350 solution, as shown earlier in Fig. 2-3(a). With the co-flow on, the jet broke up into main and satellite droplets. The satellite droplets segregated to the periphery of the



spray, leaving a central round spot of main particles (Fig. 2-7(a)) surrounded by a circular band of much smaller particles. Fig. 2-7(b) shows one area from the beginning of this band, showing a few main particles, and also intermediate sizes (whose contribution to the size distribution is not statistically relevant). The main particles are buckled (deflated) shells, whereas the satellite particles are predominantly cup-like.



**Figure 2-7** Particle morphologies obtained from 350kDa PS/MEK solutions; scale bars: 1  $\mu$ m.

For the next lower polymer concentration, 1% w/v (Fig 2-7(c)), the main particle size reduces, as expected, given the similar initial droplet size (see Table 2-2). These particles often have fibers attached which can be quite long and curl on the collector, as

shown in the inset of panel (c). Since the EHD microjet contains less polymer than just needed to prevent complete jet breakup (5% w/v), the jet breakup must also be complete at this lower concentrations, and the fibers must be due to droplet coulombic instability.

At 0.2% w/v, Fig. 2-7(d), the trend toward smaller main particles size continues. Droplets in this spray underwent coulombic instability, as shown by the mixed pointed and elongated morphologies, as well as by the significant fraction of the deposited mass in the form of small nanoparticles (much greater than for the 1% w/v sample). Some main particles are pointed on two opposite ends, either with a short or a long fiber attached. Mixed with these are long stretched particles, also double pointed, and typically flat (ribbon-like). These shapes are reminiscent to the ones encountered with PMMA-350 at the same initial polymer concentration (Fig. 2-7(c)).

High molecular weight PS-MEK solutions show similar trends in the transitions between morphologies to the PMMA-MEK high molecular weight solutions, as the initial polymer concentration is reduced: Incomplete jet break up (turning off the co-flow) → complete jet breakup without coulomb instabilities → Coulomb instabilities without progeny particles → extensive coulombically unstable main particles and progeny particles (progeny particles might be connected by nanofilaments). However, for PS, the transitions happen at slightly higher polymer concentrations.

#### *35 kDa PS / MEK*

Particle collections from the 35 kDa PS/MEK solutions are shown in Fig. 2-8. The main particles get smaller as initial polymer concentration is reduced (again, as expected, since the initial droplet size is expectedly similar; Table 2-2). All particles present little or no buckling, unlike the high molecular weight solutions, or any of the PMMA solutions.

In the most dilute solution (0.2% w/v), the amount of progeny particles increases, and many of the main particles hold a single fiber (Fig. 2-8(d)).

In the three most dilute cases, the particles become more elongated pointed/elongated towards the fiber as polymer concentration decreases.

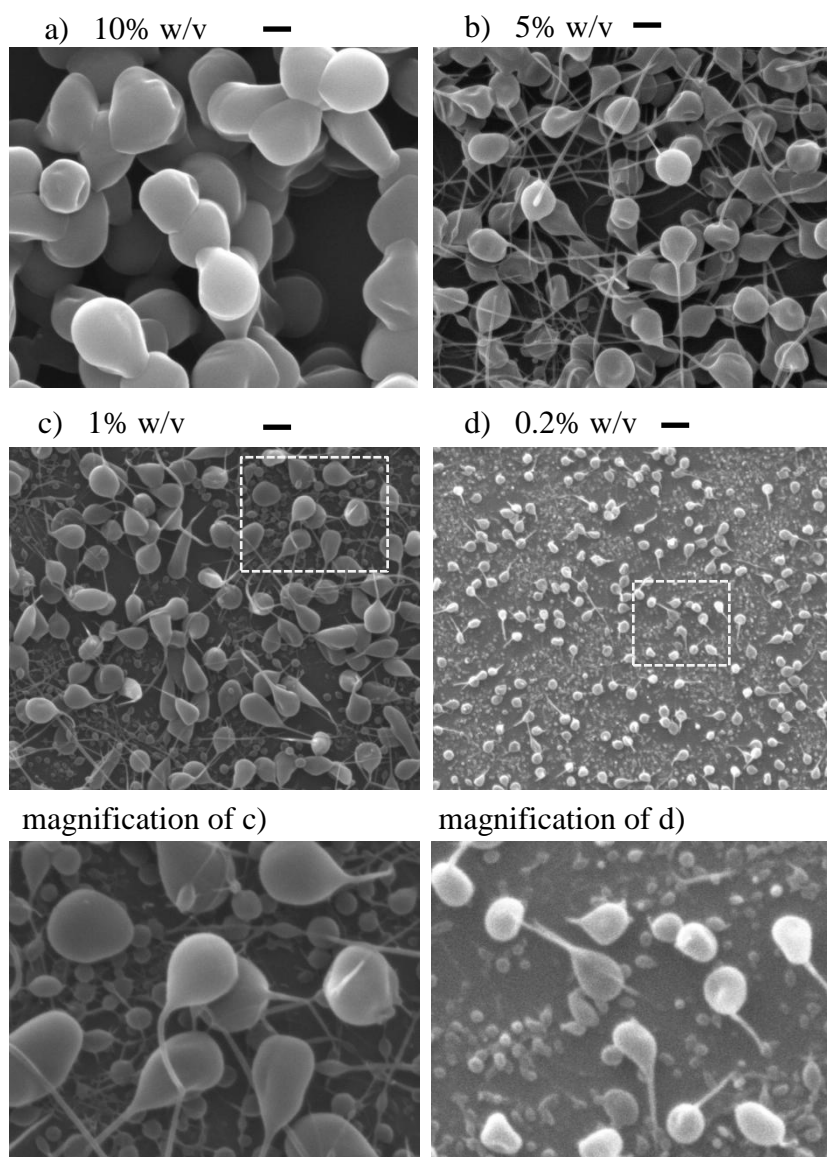


**Figure 2-8** Particle morphologies obtained from 35 kDa PS/MEK solutions; scale bars: 1 $\mu$ m.

### *35 kDa PS / DCM*

We also sprayed 5% w/v PS-35 in DCM. DCM has lower boiling point than MEK; therefore, we expect faster droplet evaporation rate than MEK solutions, at least initially. Another key difference is in the electrospaying. In order to electrospay it stably at 2  $\mu$ L/min we had to raise the conductivity of this solution, done by adding rhodamine (see section 2.2.1).

Fig. 2-9(a) shows that main particles of mixed elongated shapes, which indicate formation (solidification) during coulombic instabilities. In order to pick the predominant shape, we imaged the particles collected while moving the silicon substrate

under the spray (Fig. 2-9(b)). The predominant shape is dumbbell like, namely two terminal beads connected by a fiber. Round (flat) particles are also found. The particle flatness and lack of progeny particles suggest a very thin shell formed early in the droplet history, before or during the first coulomb instability. Fig. 2-9(c) shows the periphery of the deposition spot, where the main particles (of similar size to the main particles of Fig. 2-9(a) are all double pointed (have two opposite fibers), with 5-10  $\mu\text{m}$  long nanofibers, the longest of which have beading. This behavior is similar to that found for the same polymer in butanone (1% w/v concentration), where the main particles at the periphery predominantly had two fibers, while those in the center had one.

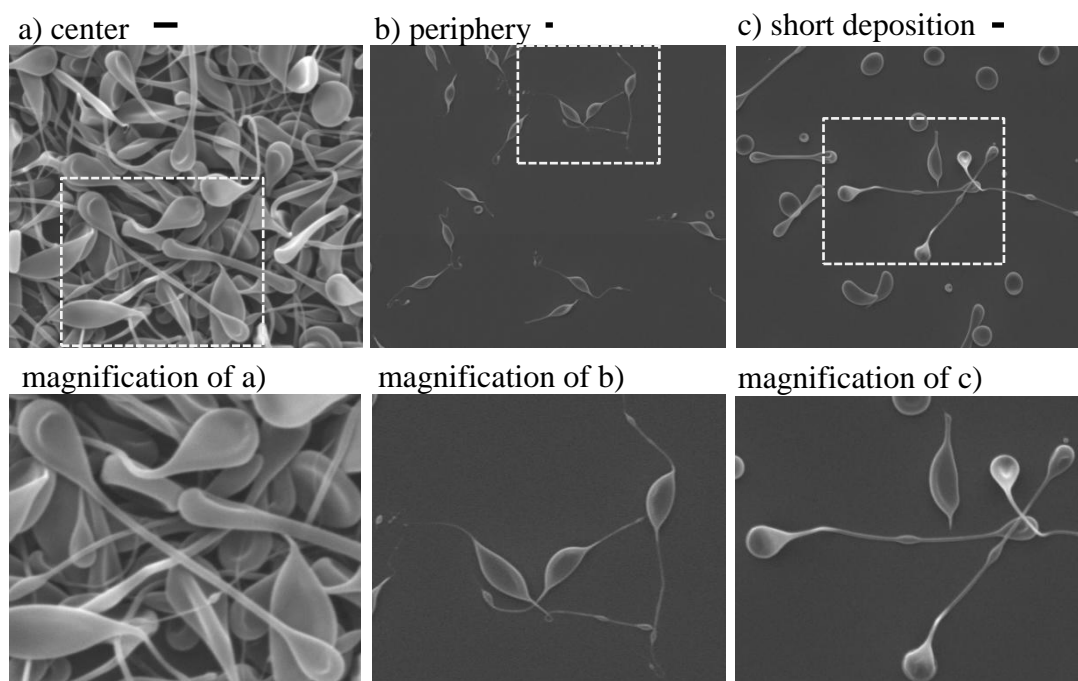


**Figure 2-9** Particle morphologies obtained from 35 kDa PS/DCM solution; scale bars: 1  $\mu\text{m}$ .

These morphologies differ from those from the MEK solution of this polymer at the same initial concentration (Fig. 2-9(f)). First, the flowrate in the PS/DCM system was not required to be close to the minimum; possibly being why the main particles come in many sizes (expected from a whipping EHD microjet; Chapter-1). Second, the elongated shapes suggest a coulombic instability pathway which does not involve jet emission.

### 2.3.3.3. *Ethyl cellulose morphologies from MEK and DCM solutions*

Electrospraying high molecular weight EC in butanone resulted in a variety of particle shapes: circular, elongated, sometimes pointed but usually without long fibers (Fig. 2-10). The 5% w/v and 1% w/v EC solutions were the most difficult ones to handle in this work, as they became sticky fast upon drying. With the 5% w/v solution, the main particles showed mixed forms (circular, elongated or pointed). Most are very flat, indicating that they were made by a thin collapsed shell, which formed early and flattened on drying. The absence of much smaller particles indicates that the main droplets do not undergo coulombic fission before they dry up to form particles. Fig. 2-10(b) is from just outside of the white central area of the deposit, made of main particles. This outer region is populated by much smaller particles, strongly suggesting that Rayleigh jet breakup into two distinct droplet sizes took place and led to segregation of the satellite droplets, which led to satellite particles. Interestingly, the satellite particles are very long with either one or two pointed ends, due likely to coulombic instability.

For the 1% w/v solution (Fig. 2-10(c)), the predominant shape is elongated and pointed towards one side. However, some of the particles are globular (without fibers), and some are pointed along two opposite sides (double pointed). In addition, some much smaller particles are collected, which must be progeny particles resulting from coulombic instabilities (Chapter-1). Such progeny particles are elongated, like the satellite particles of (Fig. 2-10(b)).

For the 0.2% w/v solution, except for the size of the particles, the picture is similar to the previous solution, with main particles are surrounded by progeny particles.

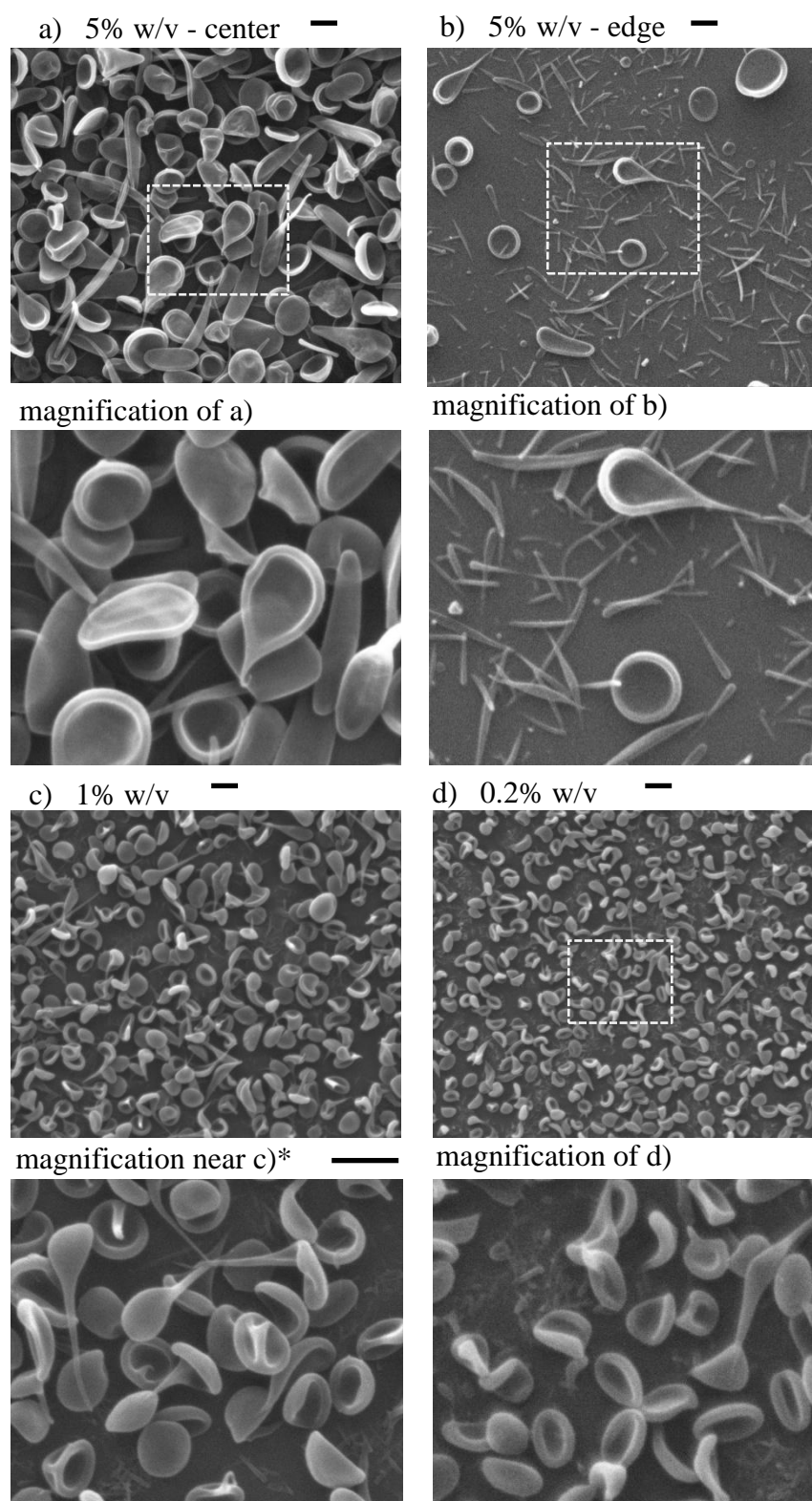


**Figure 2-10** Particle morphologies obtained from 100 cps EC/MEK solutions, \*same sample as c), from a slightly different spot; scale bars: 1 μm.

### *14 kDa EC / MEK*

For the 5 and 1% w/v initial concentrations (Fig. 2-11(a-b)), the particles are also cup like, though rounder and more uniform (in size and shape) than for the high molecular weight. Size uniformity suggests Rayleigh jet break up. The particles are surrounded by debris. A few particles are pointed. Again, these elements suggest that the debris are not jet fragments but are due to Coulomb fissions. (The particle size is smaller for the 1% w/v as expected.) At the lowest concentration, 0.1% w/v (Fig. 2-11(c)), the particles are much smaller and elongated.

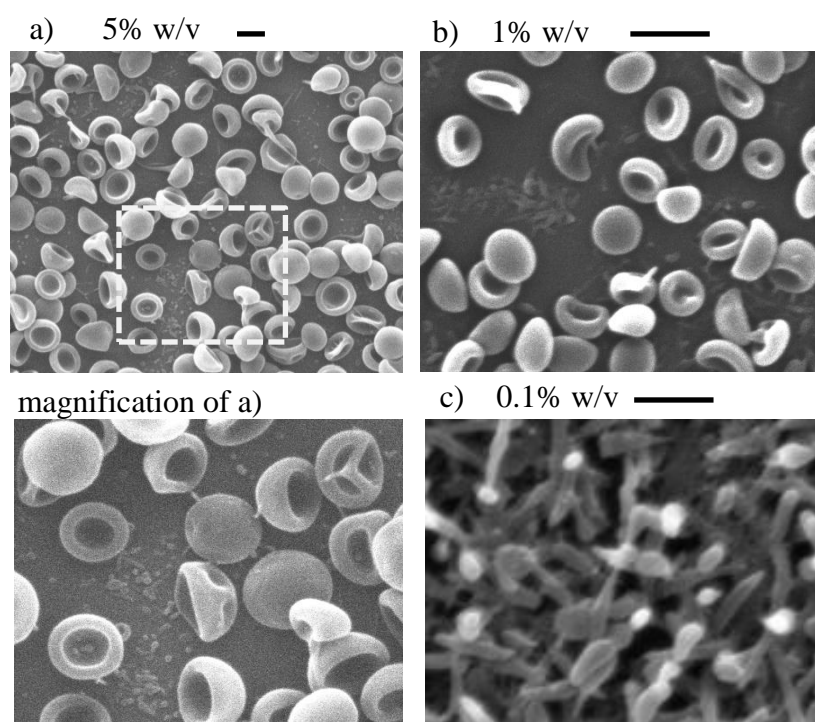


**Figure 2-11** Particle morphologies obtained from 4cps EC/MEK solutions b-c: b-c: ancillary tests (described in section 2.2.2) without co-flow; scale bars: 1  $\mu\text{m}$ .

### *EC in DCM*

We electrospayed 5% w/v low molecular weight EC/DCM and 1% w/v EC/DCM with low and high molecular weights in an ancillary setup (described as ancillary tests in section 2.2.2).

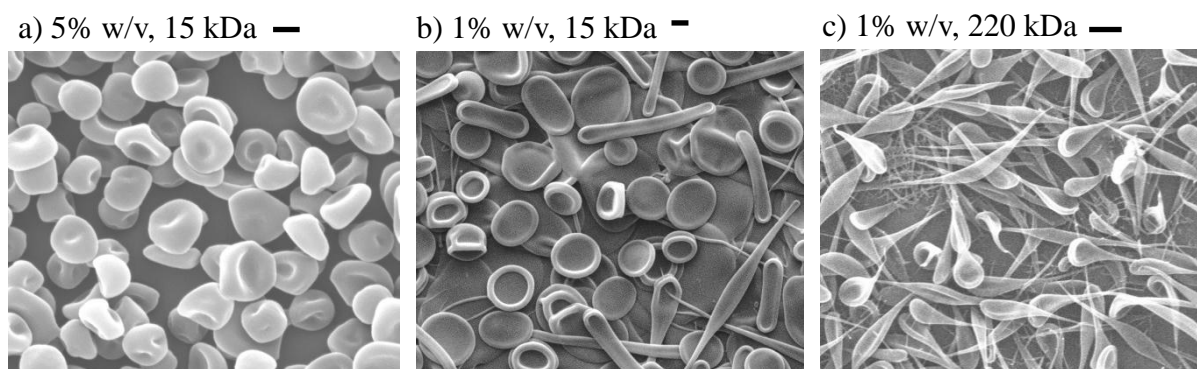


**Figure 2-12** Particle morphologies obtained from EC/DCM solutions, a with co-flow, b-c: ancillary tests (described in section 2.2.2), b: without co-flow c: with co-flow, scale bars: 1  $\mu\text{m}$ .

5% w/v 15 kDa EC solution led to globular particles without fibers (Fig2-12(a)). In fact the particles are quite uniform in size, and no satellite droplets were found for this electrospray. The regime led to true monomodal and nearly monodisperse production of particles.

1% w/v 15 kDa EC in DCM without co-flow and the 220 kDa EC in DCM with co-flow show elongated main particles, with big deformation towards one or two fibers, and absence of smaller particles. In the absence of co-flow (Fig. 2-12 (b)) the DCM evaporated quickly, forming a skin of EC at the meniscus liquid-gas interface (the cone dried up). In both cases the particles are very thin as hinted by the “transparency” of their shapes under SEM imaging, suggesting the formation of a skin early in the droplet’s evaporation history. The skin resists coulombic fission but not coulombic instability.

## 2.4. Discussion

Our experiments and others’ show that many different solid morphologies can be produced by electrospraying polymeric solutions. This variety attests to the complex interplay of variables thermodynamic, transport, mechanical, and electrical variables. A complete physical model that can predict the detailed evolution of an electrospray droplet from its birth till the formation of the final solid relic is beyond our scope. However, we aim to understand why different morphologies are observed when changing the initial polymer concentration, or the polymer molecular weight, or the



kind of polymer used. Our interpretations should be consistent with prior knowledge about the mechanical and physico-chemical behavior of polymer solutions.

#### **2.4.1. Fluid dynamic-to-solid structure transformation**

Solid morphologies are formed when polymer vitrifies from liquid structures. However, in the presence of a polymer, the properties of the viscoelastic solution will change with time as polymer concentration increases due to solvent evaporation. In turn, the fluid motions involved in instabilities (EHD jet breakup and droplet coulombic instabilities) will be strongly affected by these viscoelastic properties. And the slowing down of these motions will make solvent evaporation more important. Therefore, the theoretical prediction of these complex coupled transport mechanisms is not trivial, and has not been tackled yet. In addition, with currently available methods it is virtually impossible to experimentally probe the evolution of the fluid properties in situ in the spray, especially for micro- and nano-droplet sizes. In sum, we must resort to isolate and analyze parts of the problem. In this sense, an understanding of the various regimes is key.

Our results shown a repeating pattern in the transitions between different collected morphologies. As the initial polymer concentration is reduced, we have observed: Incomplete jet break up → Complete jet breakup without coulomb instabilities → Coulombic instabilities without progeny particles → Extensive coulombically unstable main particles and progeny particles. However, the concentration at which these transitions happen depend on the polymer, and on its molecular weight.

These transitions are consistent with the currently accepted mechanisms for polymeric nanostructure formation from electro-hydrodynamic (EHD) jetting (electrospray and electrospinning). These are summarized in Figure 2-13. The history of a liquid microstructure as released from an EHD cone-jet is followed left-to-right in the diagram, as solvent evaporates from it. Different scenarios A to E are considered, depending on the initial polymer concentration ( $c_0$ ), where in A at the top the dilute-solution regime main drops are released and undergo a series of Coulomb explosions, and in E at the bottom a concentrated solution leads to electrospinning. In scenario A, at each coulombic fission of the main drops, one or two symmetric nanojets form transiently, emitting a train of significantly smaller progeny droplets which relieve charge and electric tension from

the parent droplet (Chapter-1). The Coulomb instabilities can occur to the progeny droplets, as well, but are not followed in the schematic. At an ultimate stage (not shown), the electrical field on a droplet's surface becomes high enough (of order 1 V/nm) to desorb ions by field emission/evaporation, or a charged residue of one or several solute molecules is left [24, 25]. Such ions are the basis for electro spray ionization mass spectrometry [26, 27]. Charged-residue ions can also be formed from very large solute species. Nanoparticles are also expected to form when the last parent droplets dry up, or become too viscous to be able to undergo more fission.

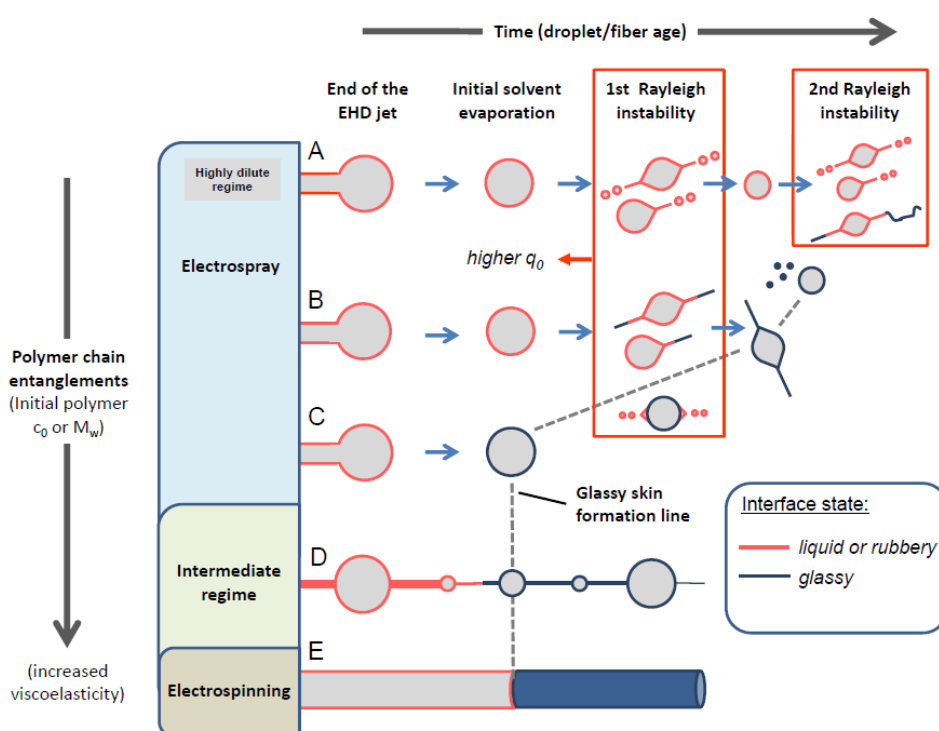


**Figure 2-13** Mechanisms for polymeric nanostructure formation from electro-hydrodynamic (EHD) jetting.

In scenarios B-C, for higher initial polymer concentration, solute precipitation happens earlier in the droplet's history. In B, polymer precipitation starts at the emitted nanojet during the first coulomb explosion. Two effects take place: Viscosity and viscoelasticity result in a long jet which does not break up, and the nanojet thinness results in rapid evaporation of the solvent from the nanojet. Therefore the nanojet could be vitrified at its leading end while it is still being emitted, and before the droplet surface polymer

vitrifies. Eventually, polymer accumulated on the droplet surface vitrifies to form a glassy skin.

In scenario C, solute precipitation happens even before the first Rayleigh droplet radius is reached, resulting in fiber-free spheres. When the EHD microjet breaks up in Rayleigh mode (Chapter-1), these spheres are uniformly sized, and they are not surrounded by smaller particles on the collected sample.

For sufficiently high initial concentration (scenarios D and E), the jet will not break up as a result of viscoelastic stabilization of the bridges connecting the beads formed during jet breakup, due to polymer chain overlaps and entanglements [28]. In scenario D the beads-on-string fluid structure is formed as a result of viscoelasticity (see Chapter-1). According to Shenoy et al. [Sh05] this regime requires a minimum average entanglement number per polymer chain of about 2:  $(n_e)_{\text{soln}} > 2$ . In scenario E, the polymer chains are sufficiently entangled to resist the growth of capillary axisymmetric perturbations. The concentration of polymer chain entanglements depends on the polymer concentration and the critical minimum molecular weight needed for entanglements in the melt (see [29,30]). Shenoy et al. claim that the polymer chains must entangle with an average number of chain entanglements per chain exceeds  $\sim 3.5$ :  $(n_e)_{\text{soln}} > 3.5$  [29].

However, beaded fibers and fibers (scenarios D & E) has also been produced with polymers of low enough molecular weight, which are not expected to entangle [31]. In this case, vitrification of the jet is due to solvent evaporation from the jet, before capillary waves can grow. Solvent boiling point has a strong influence on this outcome. However, in our experiments, the use of solvent co-flowing stream delays solvent evaporation from the jet. Another important note is that the determinations of minimum critical entanglement numbers for the appearance of beads-on-string or the formation of electrospinning, are referred to the initial solution concentration.

The exact path which an electrospray droplet follows to become a particle depends on other variables. For example, the initial electrical charge on the droplet determines how much solvent must be evaporated from the droplet before its first CE. Almería et al. [10] show that lowering the liquid flowrate in their PLGA-TFE systems lowers the charge to Rayleigh limit charge ratio of the initial droplet, thus promoting the formation of spherical particles (scenario C).

## 2.4.2. Polymer precipitation during jet breakup

As shown in Figure 2-3(d), while seeking particle production using initial polymer concentration of 5% w/v, the PMMA-MEK solution led to polymer precipitation during jet breakup (unlike the other solutions at this concentration). We know that this formed during jet breakup instead of coulombic instabilities, because when lowering the polymer concentration from 5% to 3%, the nanofibers disappear and no progeny particles are collected. And, on further lowering of the initial polymer concentration to 1%, the regime of coulomb instabilities was reached (Fig. 2-5(a)). The  $(n_e)_{\text{soln}}$  for this solution is 1.33, significantly lower than the onset value of 2 established by Shenoy et al. [29, 32]. One possible reason for this deviation is solvent evaporation from the jet despite the use of solvent co-flow around the Taylor cone. The solvent vapor jacket would prove ineffective to prevent solvent evaporation from the very (several mm) long EHD microjet (see Fig.2-2) This effect is compounded by the fact that a drier jet is more viscous, thus more stable and, thus longer.

Similar situations are found in the literature. Hogan et al. [6] find incomplete jet breakup from a solution for which  $(n_e)_{\text{soln}} = 0.79$  (56kDa polyvinyl pyrrolidone (PVP) at 0.237 volume fraction in 1:1 v/v water-ethanol). These solvents have similar volatilities to our case, and the flow rates used and jet sizes obtained are also similar to our case.

Eda and Shivkumar [31] determined (or bracketed) the critical concentrations for the two transitions from fiber-free particles to bead-free fibers in THF and DMF solutions of polystyrenes of different weight-average molecular weights ( $M_w$ ). They conclude that the solvent has minimal effect on the critical concentrations for  $M_w > 100$  kDa, where they are consistent with the entanglement model of Shenoy et al. [29]. For  $M_w < 100$  kDa, on the other hand, fibrous structures can be obtained at concentrations appreciably lower predicted by the model; and attribute this departure to rapid jet solidification. Interestingly, however, the only samples showing fibers as thin as we have found in the PMMA-MEK experiment (relative to bead size) correspond to  $M_w > 100$  kDa.

None of these works used solvent co-flow. However, Eda and Shivkumar [31] use much higher flow rates, while Hogan et al. [6] use similar flow rates.

Finally, we should also point out that the beaded jet morphology in Figure 2-3 shows extremely thin fibers, with extensive secondary beading. The ratio of bead (particle)

diameter to fiber diameter is in this case of about 50. Studies on the fluid dynamics of the thinning of the beads-on-string structure formed in electrically neutral jets (of dilute solutions of high molecular weight polymers) show that the “string” attains zero diameter in finite time (it eventually breaks under the “squeezing” of capillary stresses). In the case of an unbroken EHD jet, the charged main beads soon depart from the initial axial trajectory due to their electrical repulsions. These repulsive forces on the main beads should transfer tensile stresses (pull) on the connecting nanofibers. If, at this stage, the nanofibers are still rubbery (viscoelastic) they can undergo further thinning; whereas, if the polymer vitrifies, they may break.

### 2.4.3. Production of non-filamented particles

The term “non-filamented” is used here to identify particle shapes which are globular, namely are devoid of any filaments resulting from incomplete jet break up or coulombic instabilities. Such shapes include (i) spheres, solid or porous, or else, (ii) corrugated particles. Uniformly sized globular particles are of great interest to diverse applications. For example, corrugated particles of low effective density are of interest for pulmonary drug delivery [33]. Therefore, it is important to understand the conditions that lead to polymer precipitation before coulombic instability.

In electrospray particle production, non-filamented particle morphologies appear in the regime of “complete jet breakup without coulomb instabilities” identified in section 2.4.1. Solution polymer concentration must be intermediate: low enough to allow the EHD microjet to break up, but high enough for the polymer shell to become strong enough (or viscous enough) before reaching or at the first coulombic instability. The window of concentration depends on the polymer (and its molecular weight) and the solvent. However, it does not depend on the *rate* of solvent evaporation, since the condition for coulombic instability is the reaching of a critical diameter  $d^*$  which is a fraction of the droplet initial diameter,  $d_0$ . Provided the droplet surface tension stays nearly constant during the evaporation process, the ratio of the two diameters  $d^*/d_0$  is mostly a function of the ratio of the initial droplet charge  $q_0$  to the Rayleigh limit charge  $q_{0R}$  (Chapter-1), such that if we define  $a=q_0/q_{0R}$ , then  $d^*/d_0 = a^{2/3}$ . When this ratio is closer to the Rayleigh limit, the droplet will reach the limit radius sooner (i.e. will have to shrink less).

A theoretical model is beyond the scope of this discussion, but we can point out some of the important elements that such model should have. As described by Vehring et al [33] for uncharged droplets, solvent evaporation rate determines the solute enrichment at the droplet surface, as solvent evaporates. Solute surface concentration depends on the rate at which solute is transported by diffusion from the droplet surface to its interior, and the rate at which solute accumulates on the surface as the gas-liquid interface advances towards the droplet center, as solvent evaporates. The ratio of the two solute mass transport fluxes is called the Péclet number:

$$Pe_i = -\frac{r_s \partial r_s}{D_i \partial t} = \frac{\kappa}{8D_i}, \quad (2-1)$$

where  $Pe_i$  is the Péclet number of solute  $i$ ,  $r_s$  is the droplet radius,  $D_i$  is the diffusion coefficient of solute  $i$ , and  $\kappa$  is the evaporation rate defined as  $d^2(t) = d_0^2 - \kappa t$ , where  $d$  is the droplet diameter,  $d_0$  is the initial droplet diameter.

Interestingly, this number does not depend on droplet radius. For a given polymer/solvent combination, higher Péclet numbers will lead to greater accumulation of polymer at the surface radius. Therefore, increases in Péclet number should lead to greater surface solute concentration, if all other factors are the same (such as initial solute concentration profile in the initial droplet).

In our experiments, the Péclet numbers range between 2 and 15. From this perspective it is clear why, for every polymer/solvent combination we have tested, the highest concentration leading to coulombically unstable particles is higher for the low molecular weights. Lower molecular weight polymers experience faster diffusion from the droplet surface, thus must evaporate more until a critical concentration of polymer builds on the droplet surface. In addition, all else being equal, a low molecular weight polymer will lead to a mechanically weaker shell than a high molecular weight polymer. Therefore there will be a range in initial concentration (w/v) in which the low molecular weight polymer leads to coulombic instability while the high molecular weight leads to globular particles.

Another element of the model should be the understanding the conditions preventing the Coulombic instability. This would require also solving the linear stability analysis of the motions of a charged droplet with a polymer rich layer in an electrocapillary instability, along the lines of the famous charged-drop analysis by Rayleigh for a simple fluid [34,

35, 36]. However, whereas Rayleigh's analysis has been extended to viscous liquids, too [45], the new model would have to include both viscosity and elasticity. Furthermore, the new model would have to consider inhomogeneous liquid properties, caused by the inhomogeneous composition so long as a polymer rich layer is allowed to build on the particle surface. The spherical symmetry condition could also be questioned for an electrospray droplet which travels relative to the surroundings, and thus experiences inhomogeneous solvent evaporation [37].

Solute solubility is another important factor. It has been said that small Péclet numbers ( $Pe < 1$ ) will necessarily lead to solid spherical particles, that is particles with zero porosity [11]. However, simple arguments lead to the conclusion that a solid particle cannot form at any Péclet number. Depending on solution thermodynamics, the polymer may precipitate at lower or higher concentrations. Since the precipitation will occur first at the surface of the droplet, where solute concentration is always the highest regardless of the Péclet number, polymers with low solubility will lead to early precipitation, forming a thinner shell. However, recirculation of the droplet, while it is liquid, could change this picture, particularly if the nucleation and growth of a new polymer-rich phase is slow enough. Therefore all of these elements could also be important.

Let us examine the special case when the formed particles have spherical shape (e.g. see [6, 10, 38]). We can show that such spherical porous particles will be porous, provided the droplet stops shrinking before or at the theoretical Rayleigh limit radius is reached. We compute the increase in average polymer volume fraction (concentration)  $c$  from its initial value  $c_0$  as the droplet evaporates from its initial diameter  $d_0$  to the Rayleigh limit diameter  $d^*$ . Taking as typical range for  $a = q_0/q_{0R}$  between 0.5 and 0.9,  $c$  would increase between 4 and 1.23 times its initial value  $c_0$ , respectively. (We have assumed that the surface tension stays approximately constant). In order to electrospray polymeric solutions, it is necessary to use relatively low initial polymer concentration  $c_0$  to allow for jet break up (section 2.4.1). For example, in our experiments with high 350 kDa PMMA, the upper limit for  $c_0$  is 5% w/v. Taking  $c_0 = 0.04$  as an example, and worst-case scenario for  $a$  of 0.5, the average volume fraction of the polymer when the droplet reaches the Rayleigh limit diameter would be  $c = 0.16$ , which is still in the soluble range for many polymers. However, the Péclet number is typically larger than one, and therefore, the concentration at the surface would be significantly greater, leading hypothetically to a stable spherical skin or shell which resists deformation. Therefore,

assuming no further shrinking of the droplet, a hollow or porous inner structure with a porosity of 84% ( $=1-0.16$ ) would be obtained. If the droplet shrinks, however, this porosity would be reduced. However, it would have to shrink many times from the moment it has formed a stable shell, before it can be said to be compact (attain zero porosity).

In conclusion, in electro spray droplet drying, the spherical morphology is likely to involve the intermediate formation of a stable spherical skin or shell which resists deformation, thus leading to a porous inner structure.

One example of spherical particles by electro spray are the PLGA particles made by several groups [6, 39, 10, 38]. Although the porosity of electro spray-generated PLGA particles has not been studied systematically, Almería et al. [38] find large voids in such spherical particles. It is possible that the dimpled texture of these particles reflects their porous inner structure. It is also unclear the role of the drug mixed in these particles on the shell formation and its mechanical properties. For example, Hong et al. [39] find that adding drug to PLGA particles changes their morphology from spherical to wrinkled.

The formation of voids within the spherical particle by electro spray can be explained by either ingress of ambient gas or solvent boiling [40]. After stabilization of the shell, solvent evaporation will continue. In the formation of spherical particles voids could form by ingress of gas into the droplet by diffusion through the shell or transport through nanopores. Porosity in electro spray particles can also be produced within the shell by other mechanisms involving the non-solvent action of a vapor (such as water from ambient humidity), as shown in next chapter.

## **2.5. Conclusions**

We have electro sprayed different polymeric solutions, studying the effect of the following factors on particle morphology: polymer, solvent, initial polymer concentration, and polymer molecular weight (with weight mean in the 15-350kDa range), in order to identify the role of these factors on the drying process of the electro sprayed polymer solution droplets. As polymers we have used poly(methyl)methacrylate, polystyrene, and ethyl cellulose; and as solvents, butanone and dichloromethane. In these experiments, it has been essential to use a co-flowing



stream of solvent saturated gas around the electrospray needle, in order to prevent drying of the Taylor cone, particularly in the case of high molecular weight polymers above a polymer concentration (of a few % w/v typically).

The collected deposits have been analyzed by scanning electron microscopy, revealing many particle morphologies. We show that these morphologies present transitions as the initial polymer concentration is reduced, depending on the fluid dynamic regime at which polymer vitrification happens. Four regimes have been identified as: (1) Incomplete jet break up, (2) complete jet breakup without coulomb instabilities, (3) coulombic instabilities without emission of progeny droplets, and (4) coulombic instability of main droplets with emission of progeny droplets (coulombic fission).

The first regime leads to main particles surrounded by thin nanofibers, which present secondary beading. This regime happens only at the high end of the concentration range for the high molecular weight solutions. The second regime is characterized by globular particles, which may be buckled to different extent depending on the polymer and its molecular weight. These particles do not have filaments attached. The solution concentration for this regime has a narrow range.

In the third regime, obtained at lower concentrations, the particles have one or two opposite filaments, or display elongated shapes, such as dumbbell shapes. These shapes reflect different coulombic instability pathways, some occurring with jet emission, and some without. The absence of additional nanoparticles in any of these deposits indicates that the polymeric solution dried while the particle was undergoing coulomb instability, before fragmentation. The filaments are interpreted as vitrified Rayleigh nanojets that did not break up into progeny droplets.

The fourth regime, encountered only with low molecular weight polymers, led to deposits which had particle residues from progeny droplets arising from coulombic droplet fissions. In the case of high molecular weight polymers, this regime was not observed, as the third regime extended to the lowest concentrations (0.2% w/v).

In all four regimes the polymer accumulated on the droplet surface during droplet drying, where it vitrified forming a shell. The capsule thus formed deflated as solvent evaporated from its interior. As a result, none of our polymeric solutions led to spherical particles. We argue that spherical particles made by electrospray (in other

polymer/solvent systems) will have hollow or porous interior. The shell thickness depends, among other factors, on the rate of polymer accumulation relative to the rate of polymer diffusion to the droplet interior (or their ratio, the Péclet number). The shell thickness on the collected particles was dependent on the polymer and on its molecular weight, but only slightly (or not) on the initial polymer concentration.

## 2.6. References

- [1] Xie, J., Jiang, J., Davoodi, P., Srinivasan, M. P., Wang, C.-H. (2015). Electrohydrodynamic atomization: A two-decade effort to produce and process micro-/nanoparticulate materials. *Chemical Engineering Science*, 125, 32-57.
- [2] Bock, N., Dargaville, T.R., Woodruff, M. A. (2012). Electro spraying of polymers with therapeutic molecules: State of the art. *Progress in Polymer Science*, 37, 1510-1551.
- [3] Tang, K., Gomez, A. (1994). On the structure of an electrostatic spray of monodisperse droplets. *Physics of Fluids*, 6(7), 2317-2332.
- [4] Gamero-Castaño, M. (2008). The structure of electrospray beams in vacuum. *J. Fluid Mech.*, 604, 339-368.
- [5] Cloupeau, M., Prunet-Foch, B. (1990). Electrostatic spraying of liquids - Main functioning modes. *Journal of Electrostatics*, 25(2), 165-184.
- [6] Hogan, C. J., Yun, K. M., Chen, D.-R., Lenggoro, I. W., Biswas, P., Okuyama K. (2007). Controlled size polymer particle production via electrohydrodynamic atomization. *Colloids and Surfaces A: Physicochem. Eng. Aspects*, 311, 67-76.
- [7] Bodnár, E., Rosell-Llompart, J. (2013) Growth dynamics of granular films produced by electrospray. *J. Colloid Interface Sci.*, 407, 536-545.
- [8] Larsen, G., Spretz, R., Velarde-Ortiz, R. (2004). Use of coaxial gas jackets to stabilize Taylor cones of volatile solutions and to induce particle-to-fiber transitions. *Adv. Mater.*, 16, 166-169.
- [9] Meng, F., Jiang, Y., Sun, Z., Yin, Y., Li, Y. (2009). Electrohydrodynamic liquid atomization of biodegradable polymer microparticles: Effect of electrohydrodynamic liquid atomization variables on microparticles. *J. Appl. Polym. Sci.*, 113, 526-534.

- [10] Almería, B., Deng, W., Fahmy, T.M., Gomez, A. (2010). Controlling the morphology of electrospray-generated PLGA microparticles for drug delivery. *J. Colloid Interface Sci.*, 343, 125-133.
- [11] Yao, J., Lim, L. K., Xie, J., Hua, J., Wang, C-H. (2008). Characterization of electrospraying process for polymeric particle fabrication. *J. Aerosol Sci.*, 39, 987-1002.
- [12] Luo, D., Wang, T., Palo, A., Culhane, D., Castro, M., Mercado, C., Frischberg, P. (2007). High gloss non-feathering lip product. Patent EP 1768642 A1.
- [13] Do, T.-A.L., Mitchell, J. R., Wolf, B., Vieira, J. (2010). Use of ethylcellulose polymers as stabilizer in fat-based food suspensions examined on the example of model reduced-fat chocolate. *Reactive & Functional Polymers*, 70, 856-862.
- [14] Fetters, L. J., Lohsey, D. J., Colby, R. H. (2007). Chain dimensions and entanglement spacings, Chapter 25 in *Physical Properties of Polymers Handbook* (2nd edition). James E. Mark (Ed.). Springer, New York.
- [15] Barton, A.F.M. (1990). *Handbook of Polymer-Liquid Interaction Parameters and Solubility Parameters*. CRC Press, Boca Raton.
- [16] Mark, J.E. (2009). *Polymer Data Handbook*. Oxford University Press, Oxford.
- [17] Eggers, J. (1997). Nonlinear dynamics and breakup of free-surface flows. *Rev. Mod. Phys.*, 69(3), 865-929.
- [18] Reneker, D. H., Yarin, A. L. (2008). Electrospinning jets and polymer nanofibers. *Polymer*, 49, 2387-2425.
- [19] McKee, M. G., Wilkes, G. L., Colby, R. H., Long, T. E. (2004). Correlations of solution rheology with electrospun fiber formation of linear and branched polyesters. *Macromolecules*, 37, 1760-1767.
- [20] Díaz, J. E., Barrero, A., Márquez, M., Loscertales, I. G. (2006). Controlled encapsulation of hydrophobic liquids in hydrophilic polymer nanofibers by co-electrospinning. *Adv. Funct. Mater.*, 16, 2110-2116.
- [21] Clasen, C., Eggers, J., Fontelos, M. A., Li, J., McKinley, G. H. (2006). The beads-on-string structure of viscoelastic threads. *J. Fluid Mech.*, 556, 283-308.
- [22] Oliveira, M. S. N., McKinley, G. H. (2005). Iterated stretching and multiple beads-on-a-string phenomena in dilute solutions of highly extensible flexible polymers. *Phys. Fluids*, 17, 071704.
- [23] Fernández de la Mora, J. F., Loscertales, I. G. (1994). The Current Emitted by Highly Conducting Taylor Cones. *Journal of Fluid Mechanics* 260, 155-184.

- [24] Fenn, J. B., Rosell, J., Nohmi, T., Shen, S., and Banks Jr., J. F. (1996). Electro spray ion formation: desorption versus desertion. ACS Symp. Ser., 619, 60-80.
- [25] Fenn, J. B., Rosell, J., Meng, C.K. (1997). In electro spray ionization, how much pull does an ion need to escape its droplet prison? J. Am. Soc. Mass Spectrom., 8(11), 1147-1157.
- [26] Fenn, J. B., Mann, M., Meng, C. K., Wong, S. F., and Whitehouse, C. M. (1989). Electro spray ionization for mass spectrometry of large biomolecules. Science, 246 (4926), 64-71.
- [27] Fenn, J. B. (2003). Electro spray wings for molecular elephants (Nobel Lecture). Angew. Chem.-Int. Edit., 42(33), 3871-3894.
- [28] Eggers, J., Villermaux, E. (2008). Physics of liquid jets. Rep. Progr. Phys., 71(3), 036601.
- [29] Shenoy, S. L., Bates, W. D., Frisch, H. L., Wnek, G. E. (2005). Role of chain entanglements on fiber formation during electro spinning of polymer solutions: good solvent, non-specific polymer-polymer interaction limit. Polymer, 46, 3372-3384.
- [30] Munir, M. M., Suryamas, A. B., Iskandar, F., Okuyama, K. (2009). Scaling law on particle-to-fiber formation during electro spinning. Polymer, 50, 4935-4943.
- [31] Eda, G., Shivkumar, S. (2007). Bead-to-fiber transition in electro spun polystyrene. J. Appl. Polym. Sci., 106, 475-487.
- [32] Shenoy, S. L., Bates, W. D., Wnek, G. (2005). Correlations between electrospinnability and physical gelation. Polymer, 46, 8990-9004.
- [33] Vehring, R., Foss, W. R., Lechuga-Ballesteros, D. (2007). Particle formation in spray drying. J. Aerosol Sci., 38, 728-746.
- [34] Rayleigh, J. W. S. (1882). On the equilibrium of liquid conducting masses charged with electricity. Phil. Mag., 14, 184-186.
- [35] Rayleigh, J. W. S. (1945). The Theory of Sound. Vol. II. Dover, New York. Unabridged republication of the second edition of 1896.
- [36] Fernández de la Mora, J. (2007). The fluid dynamics of Taylor cones. Annu. Rev. Fluid Mech., 39, 217-243.
- [37] Arumugham-Achari, A., Grifoll, J., Rosell-Llompart, J. (2015) A comprehensive framework for the numerical simulation of evaporating electro sprays, Aerosol Sci. Tech., 49(6), 436-448.

- [38] Almería, B., Gomez, A. (2014). Electropray synthesis of monodisperse polymer particles in a broad (60 nm–2  $\mu$ m) diameter range: guiding principles and formulation recipes. *J. Colloid Interface Sci.*, 417, 121-130.
- [39] Hogan Jr., C. J., Pratim, B. (2008). Porous Film Deposition by Electrohydrodynamic Atomization of Nanoparticle Sols. *Aerosol Sci. Tech.*, 42(1), 75-85.
- [40] Arai, S., Doi, M. (2012). Skin formation and bubble growth during drying process of polymer solution. *Eur. Phys. J. E*, 35, 57.
- [41]: Santamaría A., Lizaso M. I., Muñoz M. E. (1997). Rheology of Ethyl cellulose solutions, *Macromol. Symp.* 114, 109-119.
- [42]: Wagner, H.L. (1987). The Mark-Houwink-Sakurada Relation for Poly(Methyl Methacrylate), *J. Phys. Chem. Ref. Data*, 16, 2, 165-173.
- [43]: Wagner, H.L. (1985). The Mark-Houwink-Sakurada Equation for the Viscosity of Atactic Polystyrene, *J. Phys. Chem. Ref. Data*, 14, 4, 1101-1106.
- [44]: Mark, J.E. (2007). *Physical Properties of Polymers Handbook*, Springer-Verlag, New York
- [45] Saville, D. A. (1997). Electrohydrodynamics: The Taylor-Melcher leaky dielectric model. *Ann. Rev. Fluid Mech.*, 29, 27-64.

# 3. Polymeric nanostructures by electro spraying in non-solvent water vapor environment

## 3.1. Introduction

The function of polymeric micro and nanoparticles is strongly dependent on their internal and surface porosity. Electro spray have been used to make particles with many different morphologies [1,2]. In particular, porous particles made by electro spray have been reported from various polymer solvent systems: poly(methylmethacrilate) (PMMA)/methylene chloride (MC) [3], poly(lactic-co-glycolic acid) (PLGA)/acetonitrile [4], polystyrene (PS)/tetrahydrofuran (THF) [5-8], Polycaprolactone (PCL)/chloroform [9], PMMA/THF [8], polylactic acid/chloroform [10], PLGA/acetone [11], PLGA/MC [12], ethylcellulose (EC)/butanone (methyl-ethyl-ketone, MEK) [13], Polyhydroxybutyrate/chloroform [14], and PLGA/trifluoroethanol [15]. Hollow particles with torn thin shells have been also found in other systems: PMMA/THF and PS/THF [8], PLGA/acetonitrile [11], and PMMA in various solvents [16].

Understanding the mechanisms responsible for the different morphologies of electro sprayed particles should be important for advanced particle engineering. However, we found only a few studies on such mechanisms. One is [7], where they change the tetrahydrofuran (THF)/ dimethylformamide (DMF) solvent ratio and they

find bigger porous particles for THF and smaller smooth and compact particles for DMF. Xie et al. in a recent review [1] qualitatively explain pore formation as depending on the solvent vapor pressure: fast solvent evaporation reduces the time available to the polymer chains to re-arrange themselves within the droplet during rapid solidification [1].

Some studies suggest that relative humidity is also an important factor. [13] report that ethylcellulose (EC) particles with smooth surface are formed at low RH and particles with surface porosity are formed at high RH in EC/MEK solutions. Ikeuchi et al [10] have studied the effect of RH in polylactic acid (PLA)/chloroform system, and found smooth, buckled particles at low RH, and porous globular particles at high RH. They explain the effect of RH with electrostatic expansion of the droplet. They found also that when instead of pure chloroform, they use a mixture of chloroform/ethanol they got smaller particle diameter and filamented particles. Except [13,10,5], none of the other mentioned electro spray works identify the role of relative humidity and did not control this parameter.

In the electrospinning field, forming porous fibers is well studied. Using of water vapor environment has proven to be a convenient and versatile tool to create nanostructures on polymer fibers [5,17-28]. Polystyrene (PS) is the polymer that has received overwhelming attention, mostly in tetrahydrofuran (THF) [5,19,20,23,25-28] or in dimethylformamide (DMF) [18,20-24], or mixtures of these. Similar studies on other polymer systems are: poly(acrylonitrile) and (polysulfone) from DMF solutions [17], poly(methyl methacrylate) (PMMA) from DMF/dichloromethane (DCM) mixture [29], PMMA from DCM, Ethyl acetate, acetone, THF, DMF [30], PCL from Chloroform, DCM, THF and formic acid [31]. The PS/DMF and PS/THF works are described more extensively in the next subsection (3.1.1.).

Given the similarities between electro spray and electrospinning, in the present work we have hypothesized that water vapor can also be used as a tool to engineer micro and nanoparticles made by electro spray.

Therefore, in the present work we study the effect of relative humidity in different polymer-solvent systems. The water insoluble polymers chosen in this study are polystyrene (PS), poly(methyl methacrylate) (PMMA), and ethylcellulose (EC). Primarily we have used a water soluble solvent, butanone (methyl-ethyl-ketone, MEK)

which has a moderate boiling point (80°C). In a few additional tests, we have used dichloromethane (DCM) which has a lower water solubility and lower boiling point (40°C). We use three different initial concentrations and two different molecular weights per polymer (“high” molecular weight ranging from 220-350 kDa and a “low” molecular weight ranging from 15 kDa to 35 kDa) in order to find out which are the important parameters that lead to porous polymeric particles at high RH.

### **3.1.1. Pore formation at high RH in electrospinning of PS solutions**

Several electrospinning studies have recognized and studied the role of RH as the responsible factor for pore formation in polystyrene fibers [5,18-28]. We can distinguish two types of fiber structures. The first type is typically found in PS/DMF studies, where usually a glassy skin and a porous internal structure are found. The skin surface is either smooth with a thin glassy skin [22,24] or porous or wrinkled [18]. Pore formation in PS/DMF system is explained by Vapor Induced Phase Separation (VIPS) mechanism [18,20-23]. During VIPS the non-solvent vapor (typically water) diffuses into the fiber, where it is absorbed and, as more solvent evaporates, eventually leads to phase separation by liquid-liquid demixing (see more detailed description in section 3.1.2). Because DMF evaporates slowly (boiling point: 152°C) the phase separation can happen before drying. Transport and phase-separation model exists for this system [18].

On the other hand, electrospinning PS/THF solutions in water vapor environment, generally leads to fibers with compact internal structure and a porous surface [5,19,20,23,25-28]. These studies (PS/THF) clearly show that water vapor is responsible for the surface porosity where water is not able to diffuse deeper into the core of the fiber. However, there is no consensus on how the water exactly leads to the porous structure. Some authors claim the key mechanism is similar to Breath Figure Formation (BFF) which is the formation of patterns template by condensed non-solvent (water) droplets [20, 23] (see more detailed description in section 3.1.2). THF is a volatile solvent (boiling point: 66°C) thus water can easily condense on the solution surface, as it does in BFF (see section 3.1.2). Other authors claim, that the key mechanism is liquid-liquid demixing [21,26], and others yet a combination of these mechanisms [25,27]. Table 3-1 shows the studied factors influencing surface porosity in PS/THF studies and their interpretation about pore formation. We have included studies where porosity is controlled by the DMF/THF at high RH.



**Table 3-1** Factors influencing surface porosity in PS-THF electrospinning studies and their interpretation about pore formation, up/down arrows indicate increase/decrease (RH: relative humidity, T: temperature,  $M_w$ : polymer molecular weight).

Ref.	RH ↑	T ↑	polymer conc. ↑	THF/DMF ratio ↑	$M_w$ ↑	Interpretation
[19]	pore size ↑	-	pore size uniformity ↑	surface porosity ↑	-	Combination VIPS and BFF
[27]	pore size ↑ pore density ↑	-	-	-	pore size <sup>(a)</sup> ↑	Combination VIPS and BFF
[5]	-	pore size ↓	pore size uniformity ↑	fiber diameter ↑	-	VIPS or BFF
[26]	-	-	-	-	-	TIPS
[23]	pore size ↑	-	-	surface porosity ↑	-	mechanism similar to BFF
[20]	pore size ↑	pore size ↓	pore size ↑	surface porosity ↑	-	BFF
[25]	pore density ↑	-	-	-	-	TIPS(BF) or VIPS
[21]	pore size ↑	-	-	-	-	VIPS most dominant
[28]	-	-	-	surface porosity ↑	-	TIPS+water imprint

BFF: Breath Figure Formation mechanism, VIPS: vapor induced phase separation, TIPS: thermally induced phase separation; a) at lowest  $M_w$ : secondary pores

### 3.1.2. Description of VIPS/TIPS and BFF

Theoretical background is provided here for convenience of the reader. This section can be skipped by those knowledgeable in vapor induced phase separation (VIPS)/thermally induced phase separation (TIPS) and Breath Figure Formation (BFF).

The mechanisms proposed in the electrospinning literature for pore formation are i) liquid-liquid demixing by VIPS/TIPS and ii) water imprinting by BFF. A schematic comparison between VIPS and BFF is provided in Fig. 3-1.

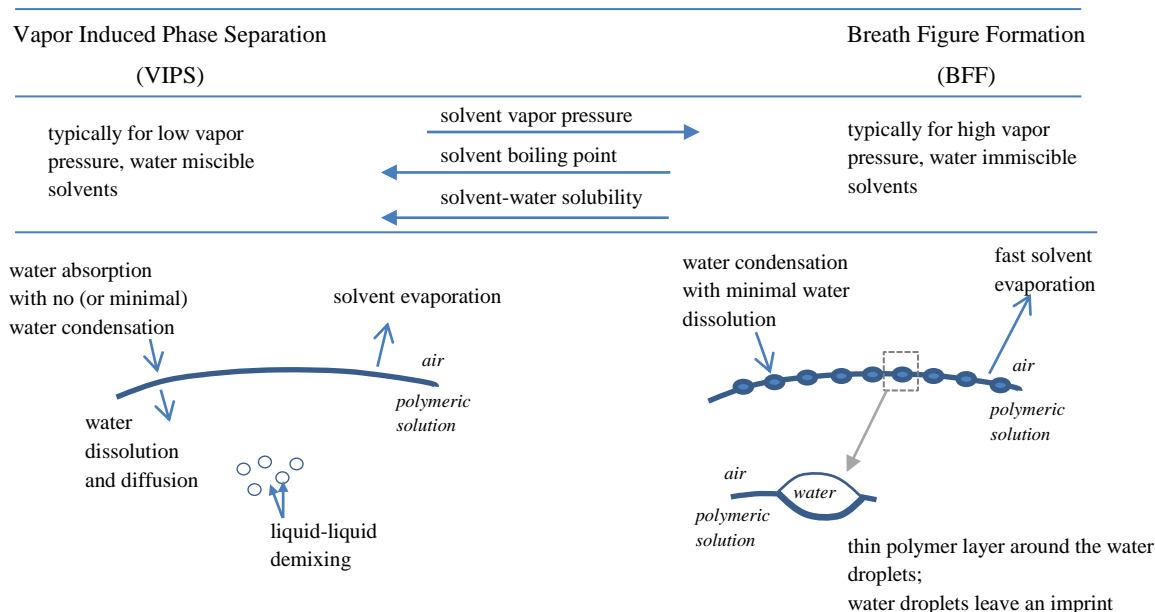


**Figure 3-1** Schematic comparison between VIPS and BFF.

*i) liquid-liquid demixing by VIPS/TIPS*

It is well-known in membrane technology that porous polymeric structures can form by phase separation from an originally homogenous solution into two liquid phases: one liquid phase being polymer-rich and the other polymer-poor [32-34]. Drying of the liquid-liquid phase separated solution would lead to porous or nodular polymeric structures. Liquid-liquid phase separation can be achieved by two main approaches [35]: (1) cooling down the homogeneous polymer solution below the upper critical solution temperature (UCST), so-called thermally induced phase separation (TIPS, Figure 3-1(a)) or (2) introducing a non-solvent into the polymer solution, so-called non-solvent induced phase separation (NSIPS, Figure 3-1(b)). NSIPS is usually explained using equilibrium phase diagrams in a ternary polymer-solvent-non-solvent (P-S-NS) system, such as in Fig. 3-2(b), where the solution composition in the region of the demixing gap is thermodynamically unstable. The size (and shape) of the demixing gap depends on the interaction parameters of the compounds [34,35]. Lu et al. show that it is not likely to form porous fibers in PS/THF systems solely by TIPS, because they observed porous structures only at high RH, but not at low RH [21]. Of course, temperature still can play a role, as T has an effect on glass transition concentration and on the miscibility gap.

A special case of non-solvent induced phase separation is vapor induced phase separation (VIPS). This is when the non-solvent is introduced into the polymer solution from the vapor phase by absorption or/and condensation [36]. The nonsolvent uptake and mixing into the polymer solution (along with the solvent evaporation), changes the solution composition, and with further solvent evaporation, it leads to thermodynamic unstable solution composition and thus liquid-liquid demixing.

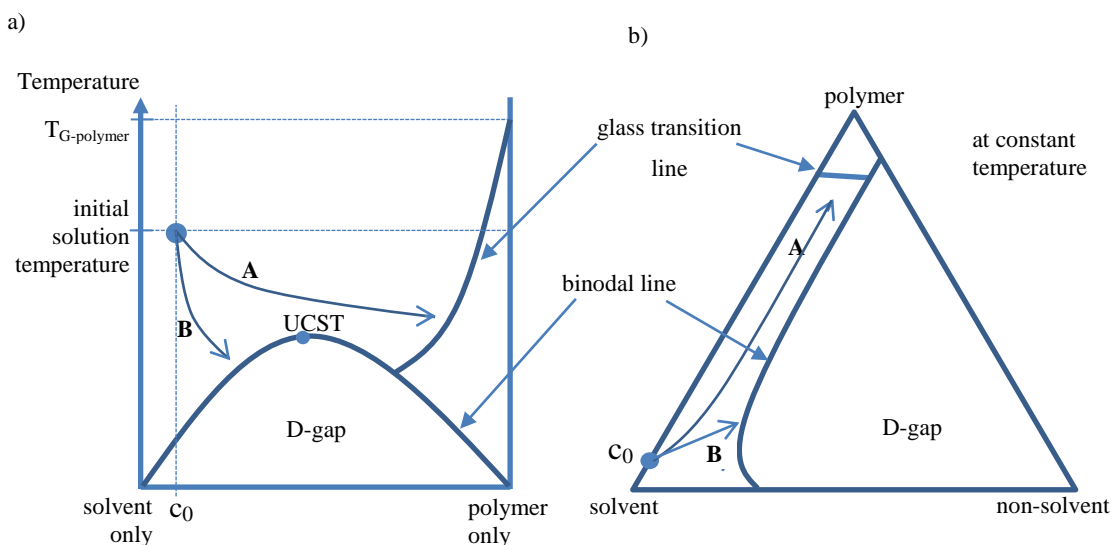


**Figure 3-2** Phase separation trajectories (A, B) in a) binary (solvent/polymer) systems by TIPS, and b) ternary solvent/non-solvent/polymer system by VIPS; A: glass transition without demixing, B: liquid-liquid demixing on reaching the binodal decomposition line; D-gap stands for demixing-gap.

As the composition changes at the surface layer, the composition also changes inside the droplet (or fiber) due to polymer, solvent and water transport (considering only diffusion, but recirculation inside the droplet is also possible). Fig. 3-3. shows the trajectory of a material element on the droplet surface in the ternary phase diagram and the corresponding concentration profiles along the droplet radius. As the solvent evaporates and water diffuses into the solution, the ternary composition is shifted from its initial binary composition at  $t=0$  towards point A, at  $t=t_1$ , where it meets the binodal decomposition line. The solution decomposes into two separate phases, represented by points B and C, at  $t=t_2$ . On the concentration radial profile of Figure 3-2(a) the radius of the droplet also changes. For glassy skin formation the polymer concentration should reach a critical value, the vitrification concentration,  $c_{vitr.}$ . When a skin forms, the water

and solvent transport through the skin are slowed down. A clear example of this kind of phase separation is the PS/DMF system in electrospinning experiments, where DMF is water miscible and evaporates slowly. Before the skin forms water can be absorbed deeply into the fiber, and dissolved into the solution. Later, with more DMF evaporation and water absorption the composition inside the fiber reaches the binodal line and will phase separate (demix) into polymer-rich and polymer-poor liquid domains. In the next stage the polymer-rich phase vitrifies into an internally porous structure.

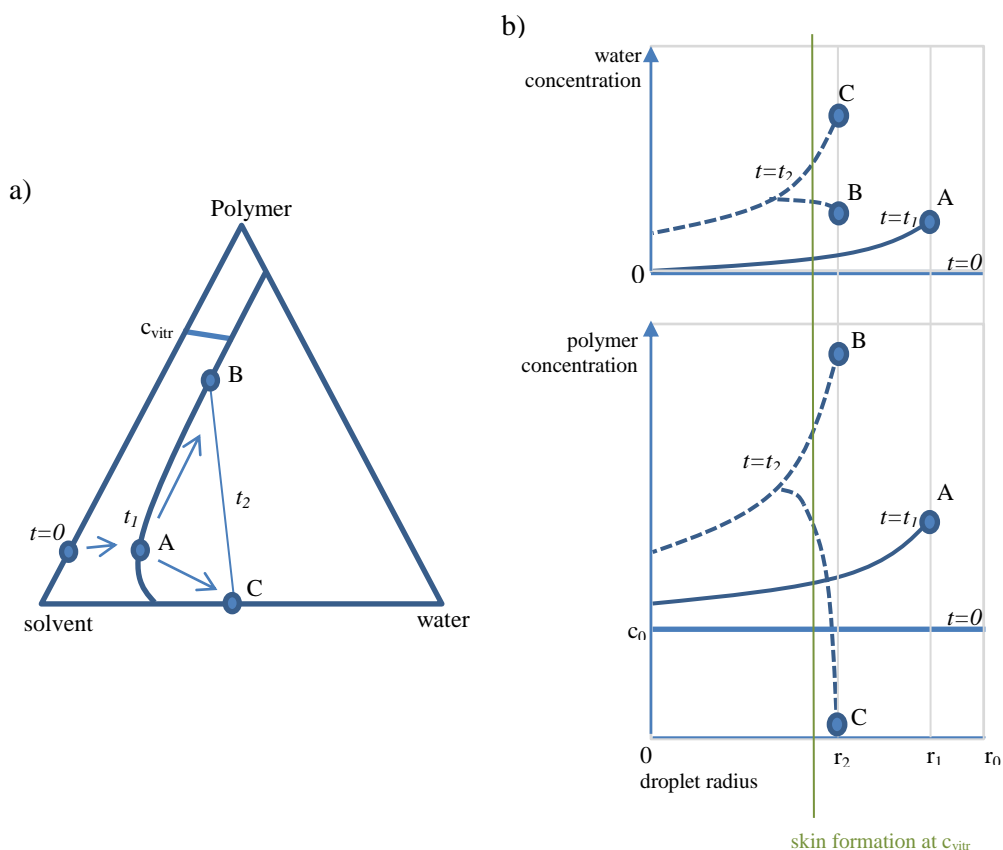


**Figure 3-3** (a) Composition change in a material element on the droplet surface represented in a ternary phase diagram and (b) a corresponding theoretical concentration profiles along the droplet radius.

*ii) water imprinting by BFF*

Breath Figure Formation in membrane technology and electrospinning refers to the arrangement of water droplets formed by condensation of water vapor on a polymer solution surface and their subsequent role as templates during polymer precipitation [37-39]. The monodisperse droplets can arrange into a hexagonal array and sink into the

polymer solution forming Breath Figure (BF) patterns. The condensation is caused by the temperature difference between the atmosphere and the surface of the solvent, which is colder due to solvent evaporation. Therefore the physical properties of solvents, such as vapor pressure, latent heat of evaporation and surface tension are fundamental [38, 40]. The typical solvents used in BFF are highly volatile and water-immiscible [38]. Ferrari et al studies different solvents (including MEK, DCM, THF) for PS solutions and they point out that the solvent affinity between the polymer and the solvent is a key parameter, too. They agree with Tian et al. [41], who concluded that a thin polymer film is formed on the surface of the condensed water droplet only for polymeric solutions in a good solvent. This thin polymer film decreases the surface tension between the solvent and the water droplets, and as a consequence hinder the coalescence of the water droplets. In a poor solvent, the migration of the polymer chains to the water/solution interface is restricted, and the water droplets coalesce resulting poor regularity of pores or no BFF [40].

## 3.2. Materials and Methods

### 3.2.1. Materials

Polystyrene, PS ( $M_w=350,000$ , and  $35,000$ ), Poly(methyl methacrylate), PMMA ( $M_w=350,000$  and  $15,000$ ), Ethyl cellulose, EC, (48% ethoxyl content, 100 cP viscosity grade,  $M_w\sim 220,000$  and 48% ethoxyl content, 4 cP viscosity grade,  $M_w\sim 15-20,000$ ) were purchased from Sigma-Aldrich and used without further purification. ACS grade butanone (MEK) and reagent grade dichloromethane (DCM) (stabilized with ethanol - 0.3 v%) were purchased from Scharlau. Some solvent properties are in Table 3-2. We added rhodamine 6G (Rh6G, Sigma-Aldrich) at 1:1250 Rh6G:polymer weight ratio to the DCM solutions in order to raise the electrical conductivity of the solution. Polymeric solutions of different concentrations (50, 10 and 2 mg/ml solvent) were prepared at room temperature and stirred with magnetic stirrer for at least 6 hours. After preparation the solutions were stored at room temperature. The electrical conductivity of the solution was measured (shown in Table-2-2). We measured the cloud point of the solutions by titration method as follows, 500  $\mu$ l of the prepared solutions was placed in a glass vial and added water by 10  $\mu$ l portions (Fig. 3-4). Cloud point was taken when

the solution phase separated and did not dissolved back to one phase after mixing it well (shaking).

**Table 3-2** Some solvent properties

	solubility in water <sup>(a)</sup> @ 20 °C (g/100 mL)	interfacial tension with water <sup>(a)</sup> @ 25 °C (mN/m)	boiling point <sup>(a)</sup> (°C)
MEK	29	1.0	80
DCM	2	28.3	40
THF*	miscible	-	65
DMF*	miscible	-	153

\* used in cited electrospinning works, a) [38]

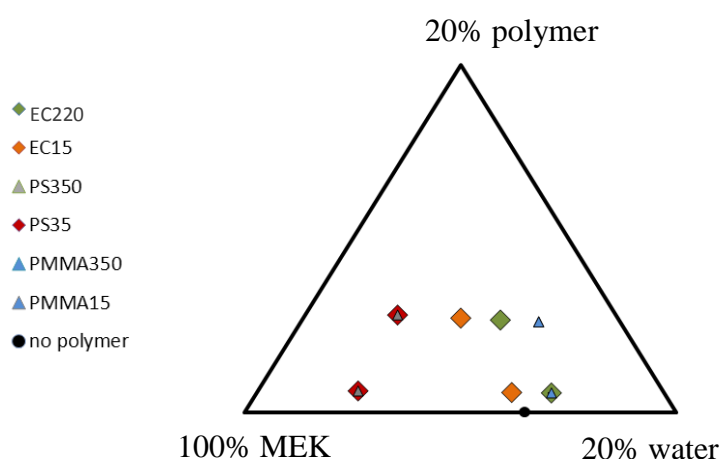


**Figure 3-4** Cloud point boundaries represented in ternary phase diagram.

### 3.2.2. Electrospaying

We used the same electrospay setup as in Chapter-2 with the addition of humid N<sub>2</sub> flow. A schematic diagram of the electrospaying arrangement is shown in Figure 3-5(a). We electrospayed in a chamber of glass walls and a methacrylate top plate, of about 10 cm size. The setup rested on an aluminium bottom plate. Thin slits exist under two of the chamber walls, through which collection substrates are moved in and out of the chamber, and drying gas flows out of the chamber. We introduced and dispersed N<sub>2</sub> (Carburos Metálicos, Premier grade) flow into the chamber at ~0.5 slpm at the top of

the chamber. We increased the relative humidity (for the high RH tests) by adding water vapor to the N<sub>2</sub> gas through a bubbler. The humidity in the chamber was monitored using a Vaisala HM34 meter probe inserted through the bottom plate. We considered RH values below 10% as “low RH” and values above 60% as “high RH”. The measured low RH values (<10%) was higher than in the pure N<sub>2</sub> gas, due to mixing with ambient air through the slits at the bottom of the chamber. A syringe pump was used to generate liquid flow. Polymeric solutions were sprayed typically at a flow rate of 2 μL/m. The needle was a square-terminated stainless steel needle (400 μm OD, 165 μm ID), and the tip was polished with diamond paste (Figure 3-5(b)), which was passed through a tee and was centered in a glass capillary (ID:1.16 mm) from which the needle protruded by ~0.22 mm. Nitrogen gas containing (saturated with) solvent vapor flowed through the tee to create a sheath flow around the silica capillary of ~18 cc/min (linear exit gas velocity near needle ~340 mm/s). The distance between needle and collector plate was 20 mm. Positive high voltage from a HV power supply (Ultravolt HV-RACK-4-250-00228) was applied to the SS capillary. An additional electrode ('back plate/electrode'), a 10 cm diameter circular brass plate was placed 17 mm behind the needle end and connected to the same potential as the needle. The back electrode contained several 3 mm holes, letting the chamber flow go through, but the holes did not change the electric field. The bottom aluminium plate was connected to a home-made nanoammeter. The signal from the nanoammeter and the applied voltage was recorded on a personal computer equipped with a National Instruments data acquisition board (NI-DAQ-PCI6221).

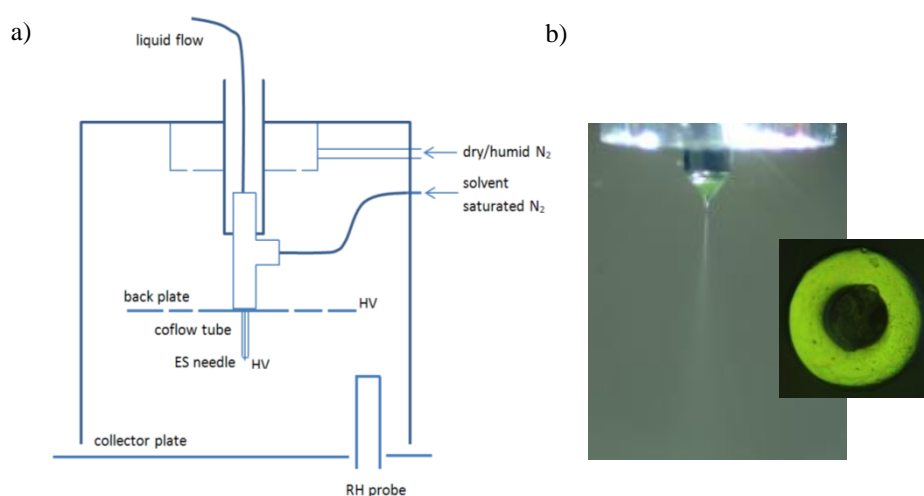


**Figure 3-5** Electro spray setup, a: chamber, b: ES needle with co-flow exit during ES, and photo of the polished needle end, needle OD: 400 μm.

Conditions were adjusted in order to produce a cone-jet mode – see Figure 3-6 for the 5% w/v concentrations. The liquid meniscus was monitored throughout the experiments. Needle voltage was found to vary slightly for the different solutions used.

The room temperature during the experiments was around 27 °C.

### **3.2.3. Particle collection and imaging**

The particles/polymeric residues were collected on pieces of silicon wafer (SiMat, prime grade, P/Boron, <100>, 500 µm thickness, 1-30 ohm•cm) of approximately 20x20 mm size, for 10 seconds. The Si wafers were slid under the spray during stable ES conditions (without disturbing the cone-jet).

All samples were gold coated (~10 nm) for SEM imaging and imaged at the center of the collection spot, using a Quanta 650 apparatus (run typ. at 30kV, ~10 mm working distance).

## **3.3. Results and Discussion**

In all of our systems the ES jet broke up into separate droplets, in accordance with our expectations, except for the high  $M_w$  PMMA at the highest 5% w/v concentration (Chapter-2).

Figure 3-6 shows the liquid meniscus during electro spray at the highest, 5% w/v concentration at low and high relative humidity (left and right panels, respectively). It shows that humidity did not change the shape of the cone-jet. However, we measured much higher electro spray current above a certain humidity level (~50% RH). The fact that the shape of the meniscus was not affected by high humidity suggests the appearance of an electrical leak, perhaps over the chamber walls.



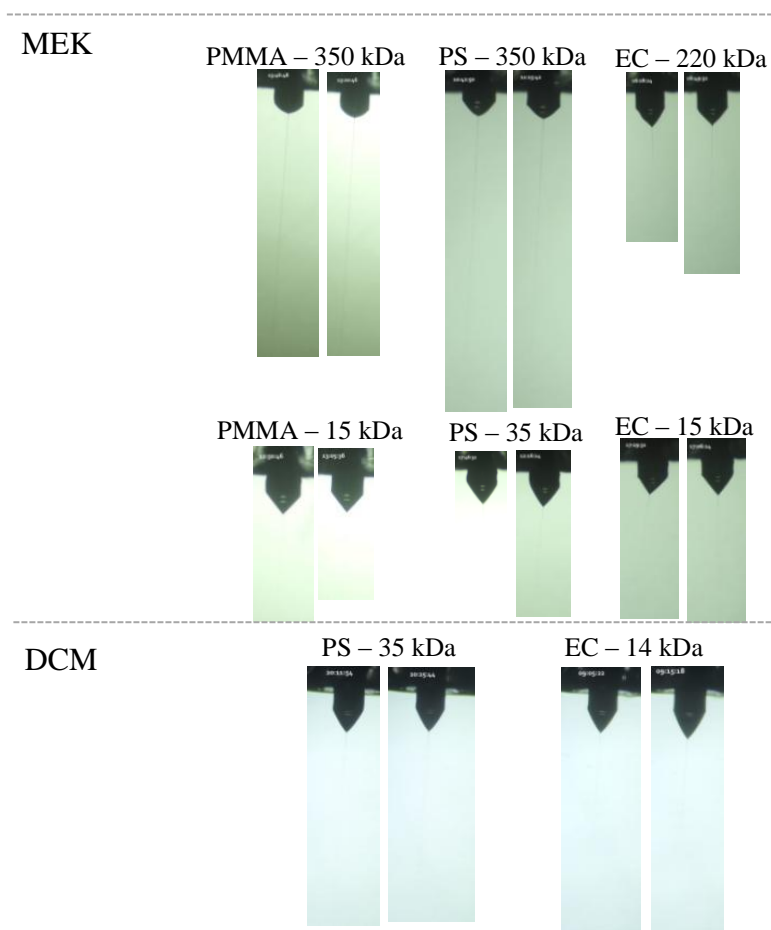


**Figure 3-6** Cone and jet photos at low (left) and high (right) RH. Initial polymer concentration: 5% w/v.

### 3.3.1. PMMA-350 morphologies from MEK solution at low and high RH

In the case of the highest initial concentration, 5% w/v PMMA350 (Fig. 3-7(a)) we found thin fibers with secondary beading suggesting that the jet did not break up completely, probably due to the long viscoelastic jet in this case. The jet break-up point falls outside of the region protected by the co-flow and some solvent evaporation from the jet takes place (see Chapter-2). The transition from electrospinning and electrospay depends on the viscoelasticity of the solution/or entanglement between the polymer chains [42]. In the case of volatile solvents the solvent evaporation also plays a significant role, as Larsen et al showed studying a solvent saturated gas-jacket [43]. The particles (beads) are about 2  $\mu\text{m}$  in size, they have a cup-like shape and are smooth. The shape is cup-like in agreement with other electrospay studies of PMMA electrospayed particles [16, 44]. The cup-like shape and the smooth surface show that a glassy skin formed on the surface of the droplet during solvent evaporation and droplet shrinking.

The polymer glass transition happened as the polymer accumulated on the surface due to relatively slow diffusion of the polymer chains (detailed description in Chapter-2) and as the droplet cooled down due to evaporative cooling. After skin formation, the solvent evaporation slows down (as it has to diffuse through the skin layer). The skin formation may prevent the droplet from further shrinking. However if the formed skin is flexible enough the capsule defined by the skin will buckle or wrinkle as the solvent continues to evaporate, or it can deflate. These changes can occur during flight, or after arriving to the collector.

When we increase the RH in the same system (PMMA-350; 5% w/v), the particle shape and size are very similar, and the thin filaments are present, too (Fig. 3-7(b)). The most obvious difference is the surface porosity. The pores are relatively small and uniformly distributed.

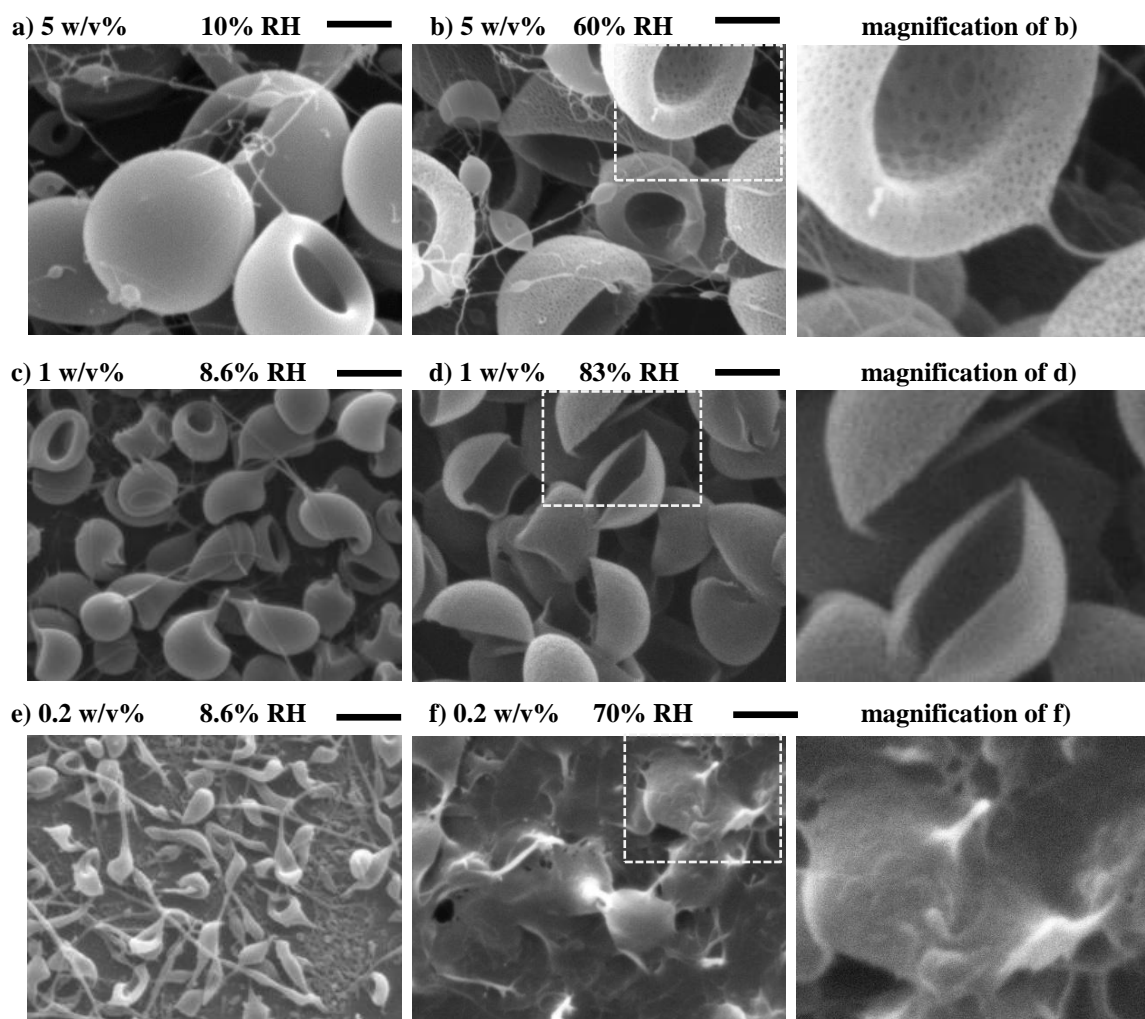


**Figure 3-7** Effect of RH on the deposited morphologies obtained by electrospaying solutions of 350 kDa PMMA-MEK at different initial concentration; flow rate: a-e) 2  $\mu\text{l}/\text{min}$ , f) 3.5  $\mu\text{l}/\text{min}$ , scale bar: 1  $\mu\text{m}$ .

Lowering the initial concentration (1.0% w/v) of the high  $M_w$  PMMA solution (Fig. 3-7(c-d)), the jet broke up into droplets at both low and high RH. At low RH (Fig. 3-7(c)) we found filaments connected to the particles, which were formed due to coulombic instability during the drying stage. We think that the filaments are not remnants from uncomplete jet breakup because the polymer concentration is low, the entanglement number is low, and additionally the jet was shorter, than for the 5% w/v concentration, so it could break up in the co-flow protected region (see also in Chapter-2). Additionally we can see that at high RH (Fig. 3-7(d)) there are no filaments, which strongly suggest, that at low RH the jet broke-up, too. Thus the filaments seen at low RH are present because at the droplet shrunk below the Rayleigh instability diameter, and the droplet ejected a viscoelastic liquid jet which dried up without disintegration into progeny droplets (Chapter 2). At low RH the collected particles are deflated (again cup-like) and a little bit stretched toward the filaments. The particle size gets smaller as the initial concentration decreases, as expected, since the computed initial droplet sizes are similar (see table 2-). The particle surface is smooth again.

At high RH (Fig. 3-7(d)) at 1% w/v polymer concentration, the shape is very different from the shape obtained at low RH. The filaments are missing, the particle diameter is slightly larger with open shell (probably thinner) and the surface is rough with nanopores. At high RH the skin formed before the droplet reached the Rayleigh instability diameter during shrinking, disallowing jet emission. We also see that the particles are hollow inside, they consist of a thin shell. Probably the shell wanted to deflate similarly to the higher concentration or lower RH case (before or after losing the charge) but it was mechanically weaker, and it torn/broke instead. At 1% w/v the surface is not as porous as at the 5% w/v.

At the most dilute PMMA350 solution (0.2% w/v) at low RH, we see particles which went through extensive stretching due to Coulomb forces during the drying. They are elongated with smooth surface (Chapter-2). At high RH a film of fused structures forms, which appear to be thin shells. It is difficult to distinguish what was the shape of the individual particles.

### 3.3.2. PMMA-15 morphologies from MEK solutions at low and high RH

We repeated the same sequence of experiments (low and high RH, three concentration levels) with MEK solutions of a lower molecular weight PMMA, 15 kDa. Due to the fact that this molecular weight is close to the entanglement critical value (Table 2-1), the polymer chain entanglement is very low. Also the polymer diffusion can be faster in the same butanone solvent than for the higher molecular weight polymer.

In general at low RH (Fig. 3-8(a,c,e)) the main particle shape is similar to the PMMA-350 case (section 3.3.1.2), but a little bit more compact, which is in accordance with the faster diffusion for the low molecular weight polymer (Chapter-2).

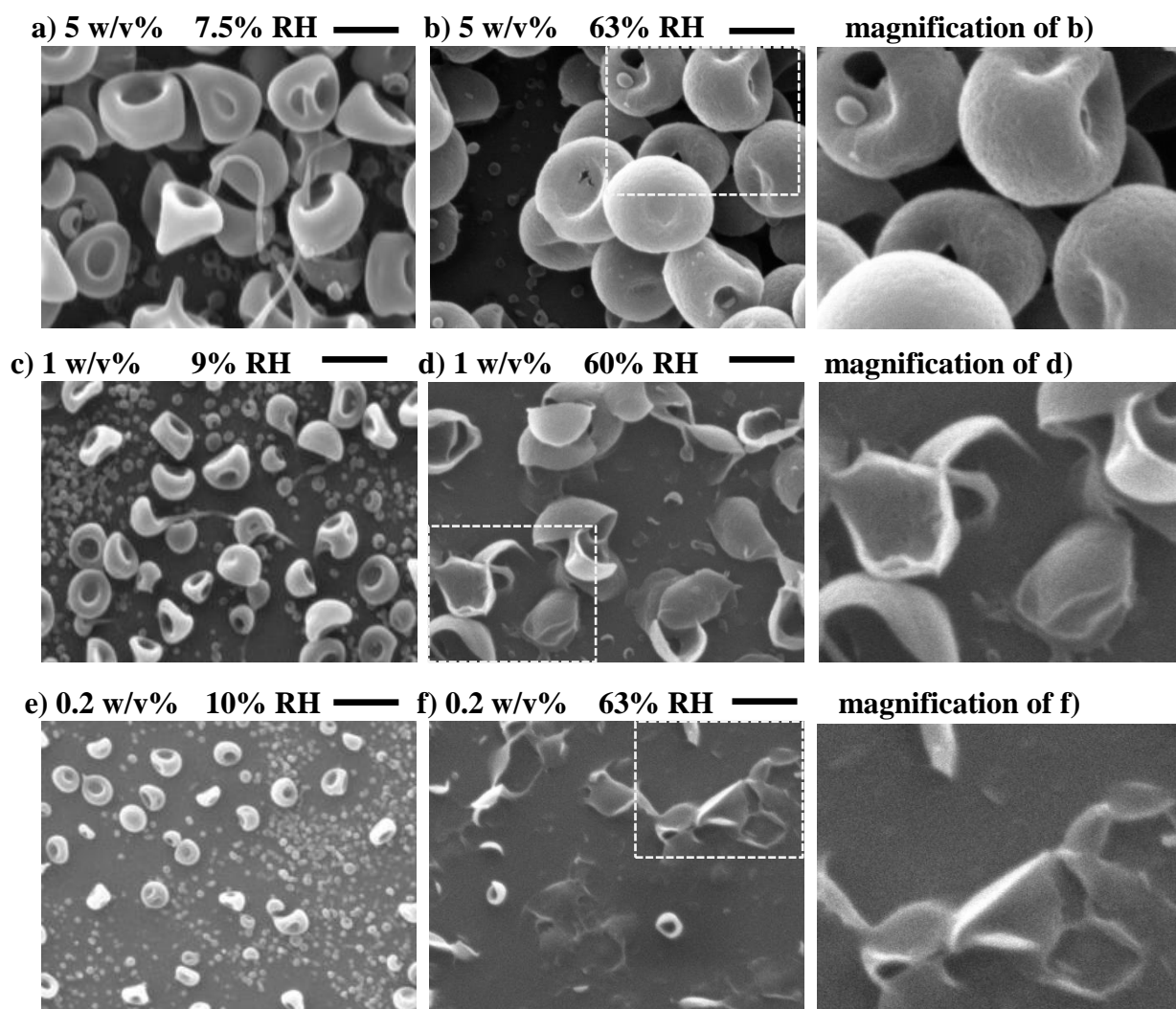


**Figure 3-8** Effect of RH on the deposited morphologies obtained by electrospaying solutions of 15 kDa PMMA-MEK at different initial concentration; flow rate: 2  $\mu\text{l}/\text{min}$ , scale bar: 1  $\mu\text{m}$ .

At high RH at 5% w/v initial concentration (Fig. 3-8(b)) we see bigger particle size than at low RH indicating earlier polymer precipitation. The lack of fibers means that no Coulomb explosion happened at high RH, similarly to the PMMA-350 case. The particle surface is textured instead of a smooth, but not porous (maybe nano-pores) as in the case of high  $M_w$  (Fig 3-7). The buckling is less extensive, than for the low RH case, the shell remained more spherical. At the same time, the shell is torn at some places showing that the shell/skin is weaker and less elastic, than at low RH. It can also be seen from/through the surface holes that the particles are hollow inside.

At 1% w/v concentration at high RH particle size also increases compared to the low RH case, the progeny particles disappear, and the shell is also open (perhaps torn apart) and a bit sticky (Fig. 3-8(d)). At the lowest concentration (0.2% w/v – Fig. 3-8(f)) wet shell residues were collected similarly to the PMMA-350 case of the same lowest concentration (Fig. 3-7(f)). Only pieces of shells can be identified, it seems that the particles/shells were still wet when they were deposited and fused together extensively.

### **3.3.3. EC morphologies from MEK solutions at low and high RH**

We studied another polymer, ethyl cellulose (EC), in butanone, to see whether similar trends happen when changing RH. We studied high  $M_w$  EC at three concentration levels, and a low  $M_w$  only at the highest concentration (5% w/v) level. At low RH the collected particles are smooth both for high and low  $M_w$  (Fig. 3-9(a) and Fig. 3-10(a)). The particles are flattened instead of cup-like shape in the case of EC-220 (Fig. 3-9(a)), suggesting thinner shell for EC than for PMMA. Some of the droplets vitrified while undergoing coulombic instability at both  $M_w$ , at all concentrations, as the pointed, tailed or elongated particles show (Figs. 3-9(a,c,e) and 3-10(a)). For the lower concentration levels of high  $M_w$  EC (Fig 3-9(e)), we found progeny particles, as a result of Coulomb explosions (see Chapter 2).

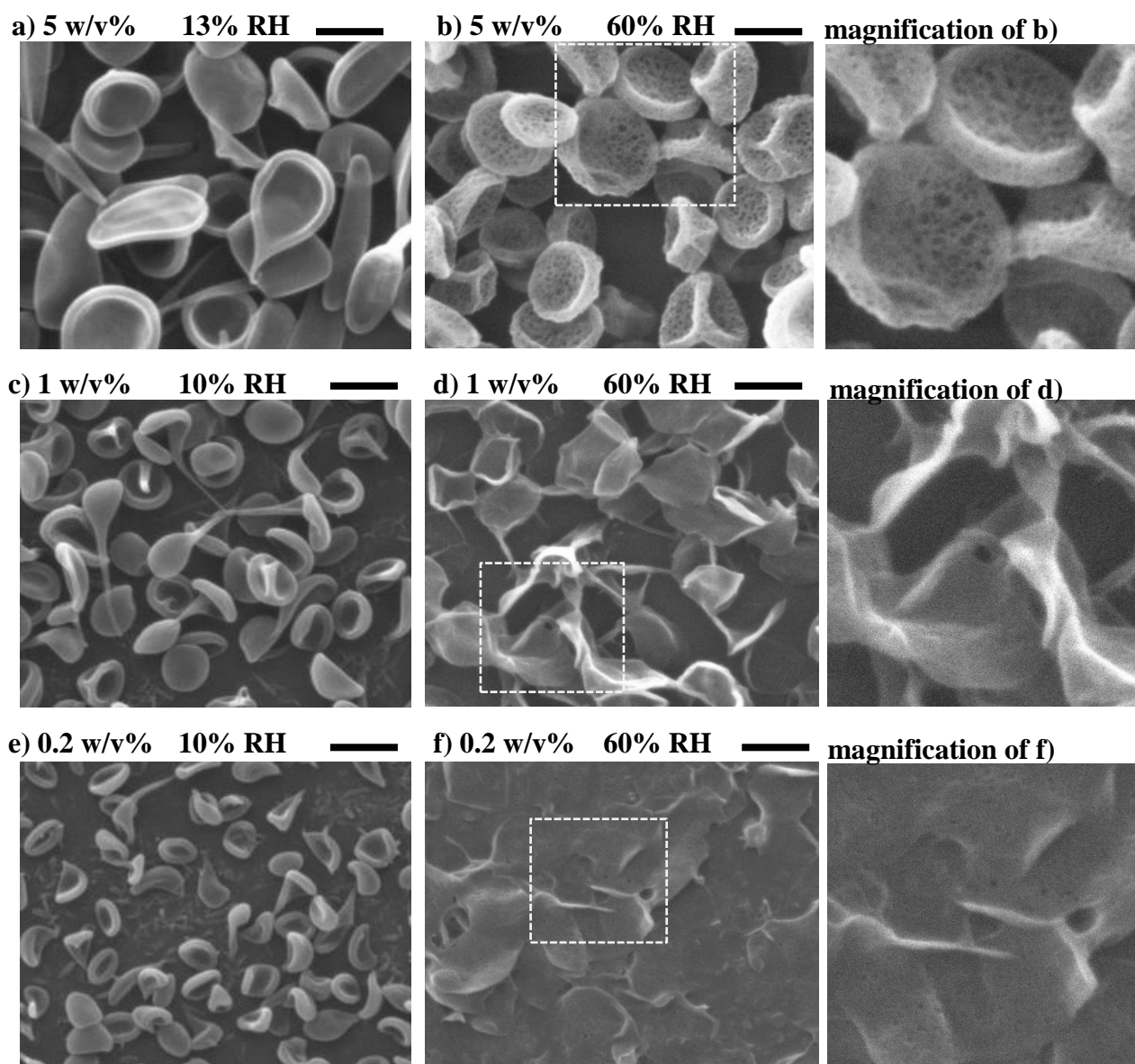


**Figure 3-9** Effect of RH on the deposited morphologies obtained by electrospaying solutions of 220 kDa EC-MEK at different initial concentration; flow rate: a-d) 2  $\mu\text{l}/\text{min}$ , e) 2.5  $\mu\text{l}/\text{min}$ , f) 3.5  $\mu\text{l}/\text{min}$ , scale bar: 1  $\mu\text{m}$ .

At high RH at 5% w/v initial concentration (fig. 3-9(b)), the size did not change significantly from the low RH case, but the elongated and pointed shapes have disappeared, and we find small pores on the surface, similarly to the high Mw, high concentration PMMA case (Fig 3-7(b)). At 1% w/v (Fig. 3-9(d)) the effect of RH is also similar to the PMMA case (Fig. 3-7(d)). The polymer precipitated out on a bigger droplet, before the first coulombic instability happened, thus protecting the droplet from fission and the surface is not as porous as in the case of 5% w/v. At 0.2% w/v the particles are again fused, clearly indicating that they arrived “wet” at the collector (Fig.

3-9(f)), following the general trend we observed for the lowest concentration high humidity cases. Since EC, like PMMA, are not water soluble, the particles must have retained some solvent (MEK).

For low molecular weight EC, 5% w/v concentration (Fig. 3-10(a-b)), the RH has a similar effect. At low RH particles went through coulombic instability and deflated into cup-shape capsules. At high RH no signs of Rayleigh instability are found, instead very corrugated shapes. Small pores at high RH are visible on some of the particle surfaces. The pores are smaller and much less apparent than for the high molecular weight spray shown in the magnification of Fig. 3-9(b).

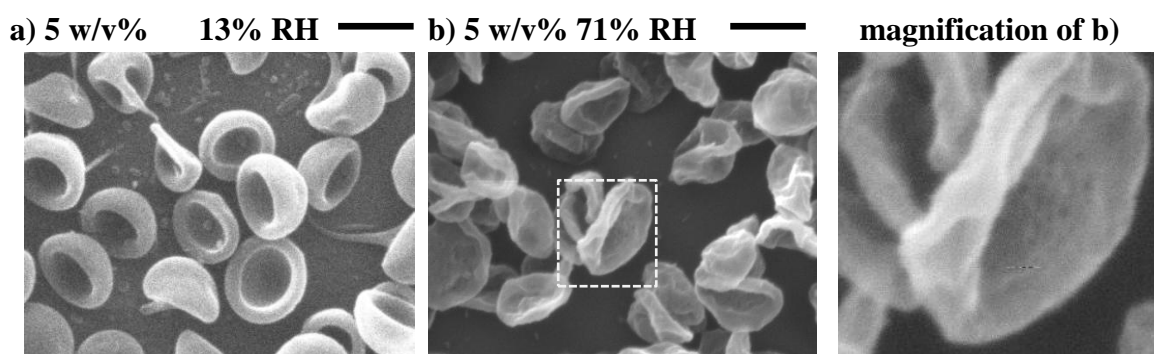


**Figure 3-10** Effect of RH on the deposited morphologies obtained by electrospaying solutions of 15 kDa EC-MEK; flow rate: 2  $\mu$ l/min.

### 3.3.4. PS-350 morphologies from MEK solutions at three RH levels

We also studied polystyrene (PS) of high and low molecular weights at three concentration levels. PS is a non-polar polymer with very low affinity for water. We included intermediate humidity levels in these experiments, too.

For PS-350 in butanone at 5% w/v initial concentration we got bucked, deflated particles with a smooth surface (Fig. 3-11(a)). As we have shown in the previous chapter, the polymer precipitated out forming a shell before the Rayleigh instability diameter could be reached during droplet shrinking.

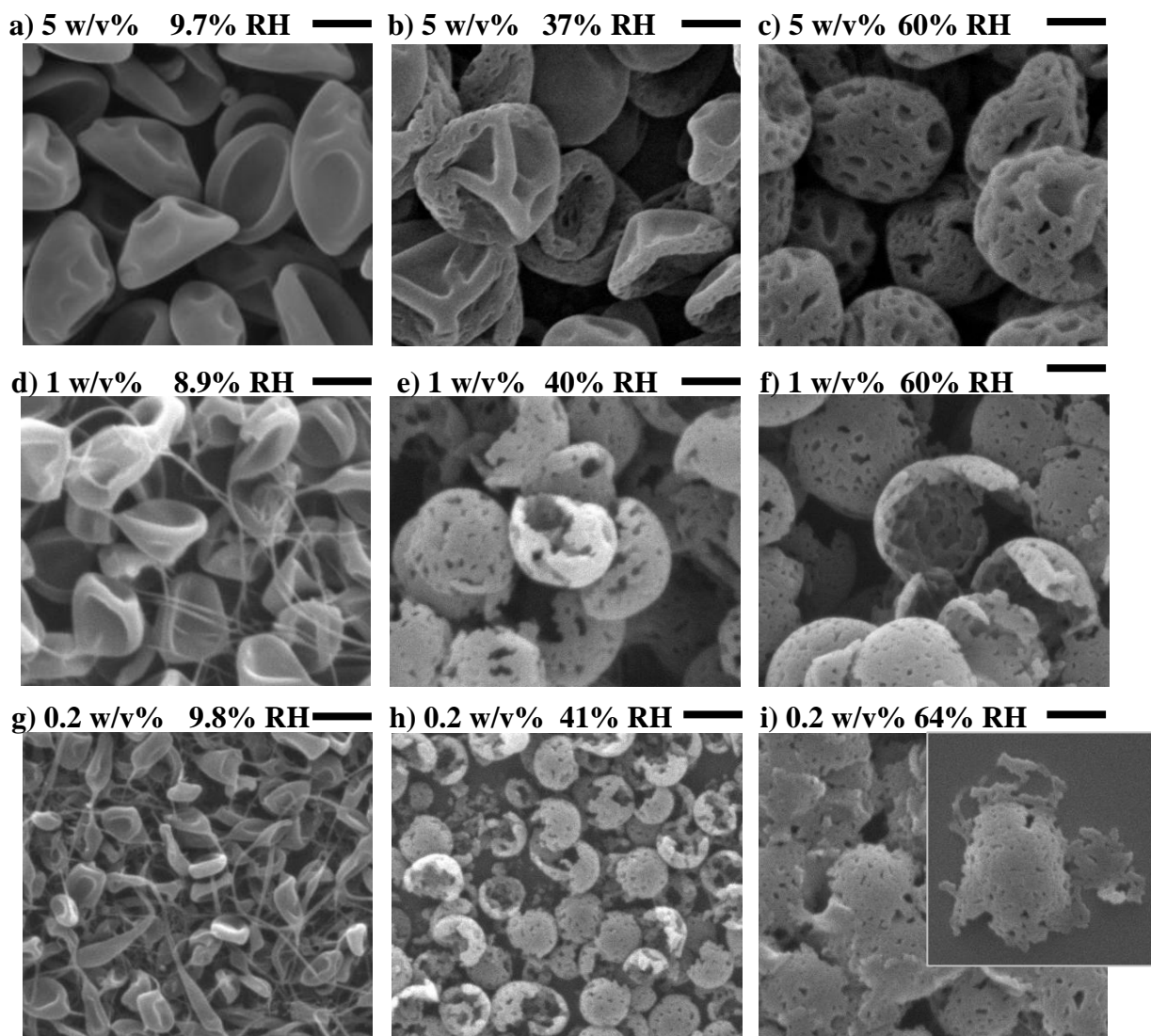


**Figure 3-11** Effect of RH on the deposited morphologies obtained by electrospaying solutions of 350 kDa PS-MEK at different initial concentration; flow rate: a-c) 2  $\mu\text{l}/\text{min}$ , d) 2.5  $\mu\text{l}/\text{min}$ , e-i) 3.5  $\mu\text{l}/\text{min}$ , scale bar: 1  $\mu\text{m}$ . Inset in i) shows a single main particle from the periphery of this collection.

At high RH (Fig. 3-11(c)) the particles become globular and present extensive surface porosity. The pore sizes are non-uniform, as well unevenly distributed over the particle surface. We speculate that the particles remained more spherical than in the previous systems we studied because pores connecting through to the interior would keep the inner and outer pressure of the microcapsule in equilibrium during solvent evaporation. The structure at intermediate RH (Fig. 3-11(b)) was unexpected. The particles show asymmetric porosity and buckling. The porous side is bent concave and the smooth side buckled similarly to the low RH case. It appears as though the exposure to moisture was consistently greater on one side of the droplets during their travel (at least while the



outer, porous shell formed). Later, as more solvent evaporated, the asymmetric shell mechanical properties led to asymmetric buckling. The random orientation of the shapes indicates that the microstructure formed prior to deposition.

For 1.0 and 0.2% w/v initial polymer concentration solutions sprayed at low RH the particles carry filaments (Fig. 3-11(d) and (g)) or are elongated (Fig. 3-11(g)) showing that Rayleigh instability has been reached during droplet shrinking (Chapter-2). Upon increasing RH the filaments disappear (Fig. 3-11(e) and (h)), and porous thin spherical shells form, many of which appear to be broken. The pore size decreases with reduced initial polymer concentration. In Figure 3-11(f) we see that the concave “inside” surface of the shells is also porous. Shell breaking could mean a more fragile structure than at low RH, and could be broken by (i) electrostatic disintegration (a sort of Coulomb fission in the solid state), or (ii) compressive failure (breakage) induced by mechanical stresses generated on collision with the particulate film. At very low concentration at the highest RH the droplets again arrived sticky (Fig. 3-11(i)), but they kept the porous shell structure.

### **3.3.5. PS-35 morphologies from MEK solutions at three RH levels**

For the lower molecular weight PS (35 kDa) at low RH at all the concentrations tested (Fig. 3-12(a,d,g)) we find filamented deflated particles with smooth surface. At 5 and 1% w/v initial concentration the filaments do not disappear at intermediate RH (37%), but their frequency is reduced. In addition holes appear on the particle shell (Fig. 3-12(b,e)). At the highest RH (Fig. 3-12(c,f)) the filaments have mostly disappear and hollow particles are formed with a shell with holes. At the lowest concentration intermediate RH (35%) the particles arrive wet again, we assume that at high RH the particles to be wet, but we do not have data for high RH.

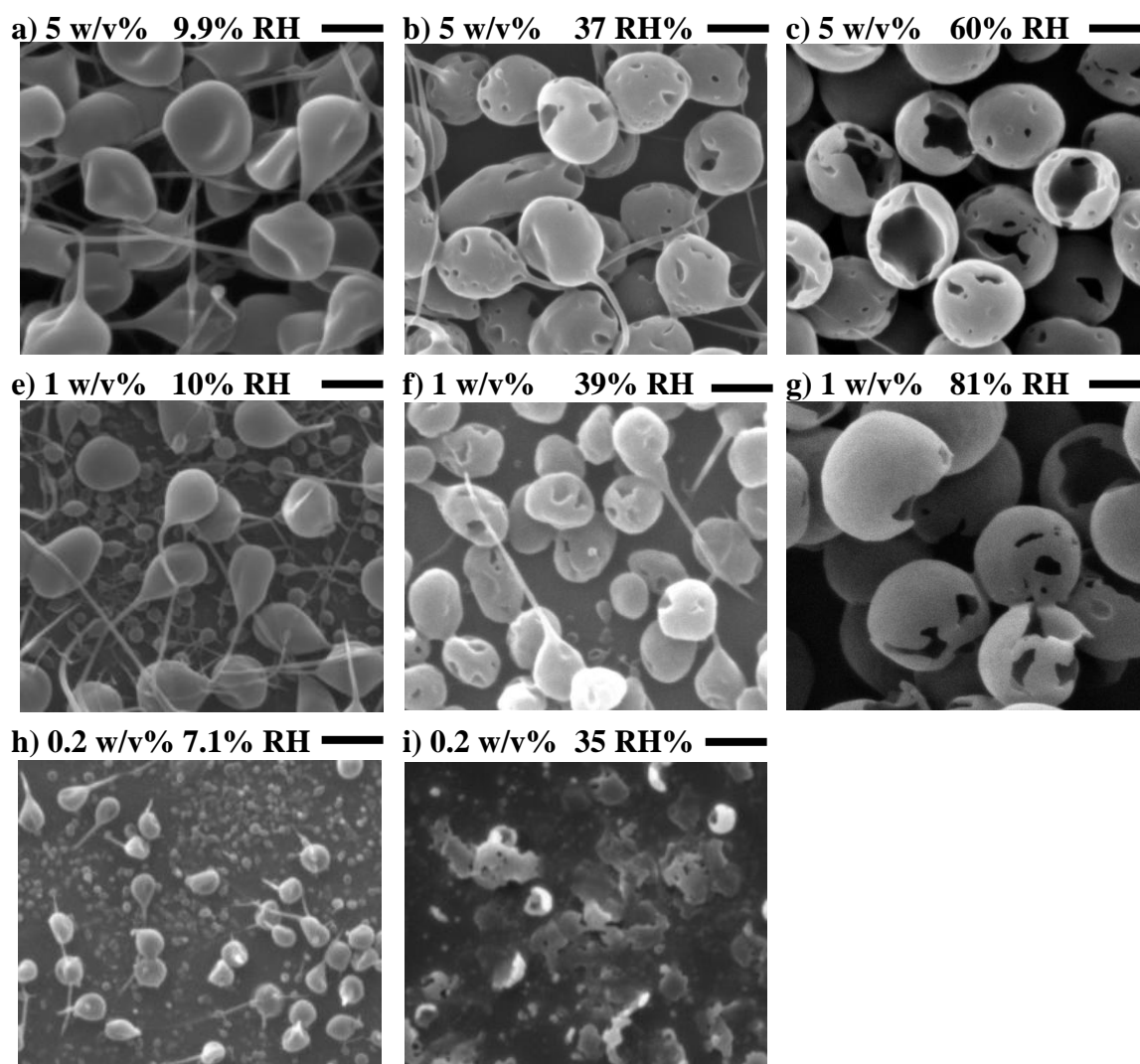


**Figure 3-12** Effect of RH on the deposited morphologies obtained by electrospinning solutions of 35 kDa PS-MEK at different initial concentration; flow rate: 2  $\mu$ l/min, scale bar: 1  $\mu$ m.

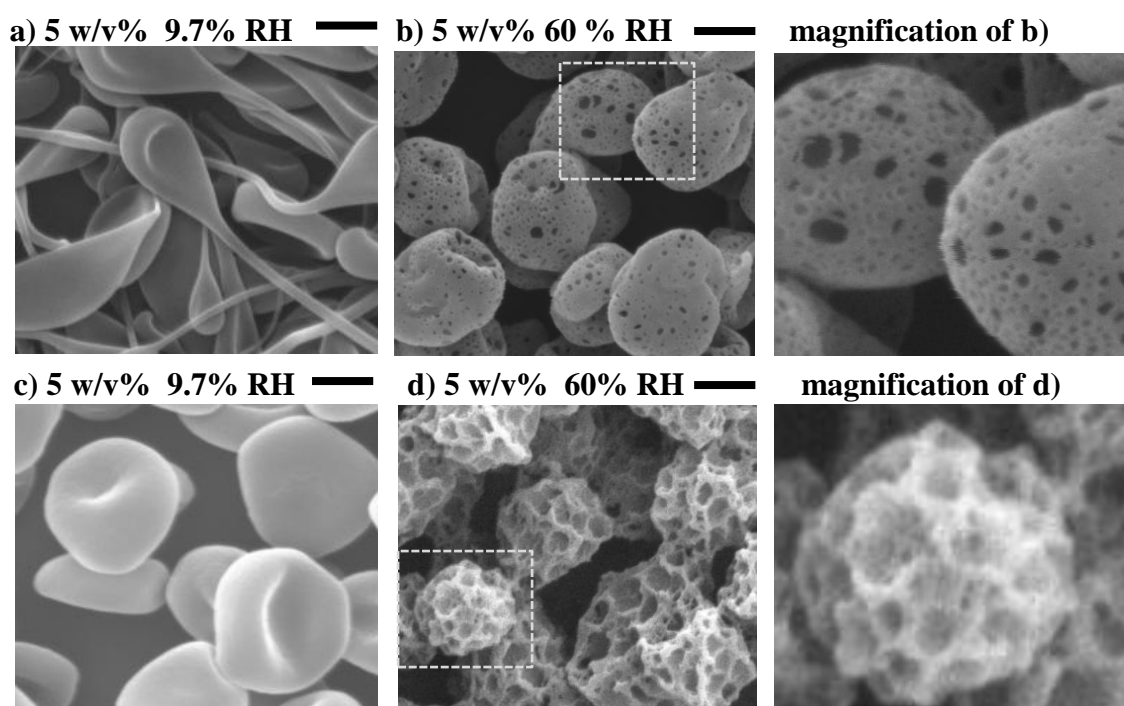
### 3.3.6. PS-35 and EC-15 morphologies from DCM solution at low and high RH

We tested the effect of humidity in the case of low molecular weight PS and EC with another water-immiscible solvent, DCM at 5% w/v initial concentration. DCM has a lower boiling point and lower water solubility, than butanone (Table 3-2).

At low RH we again got smooth particles (Fig. 3-13(a,c)). The ethyl cellulose particles were more spherical (Fig. 3-13(c)) than the PS particles, which clearly reached Rayleigh instability as we can see from the elongated, dumbbell shapes of Fig. 3-13(a). The effect of RH is remarkably different for the two polymers. At elevated RH (60%) the PS

particles are porous and globular with a small degree of buckling (Fig. 3-13(b)). Again, the fact that at high RH we got spherical particles supports the hypothesis, reached in Chapter-2, that the particle shapes at low RH are the results of coulombic instabilities, rather than incomplete jet break-up. (As shown in Figure 3-6, the cone-shapes and the jet lengths are similar.)

In the case of EC, the particles are porous with a quasi regular cell structure at the surface (Fig. 3-13(d)). The magnification of Fig. 3-13(d) shows that the cell wall itself is porous. High molecular weight EC in DCM was attempted but could not be stabilized easily. So those tests were not pursued further. Nevertheless 1% w/v EC-220 in DCM at ~60% RH gave very similar structures to the low molecular weight EC solution shown in Fig. 3-13(d).

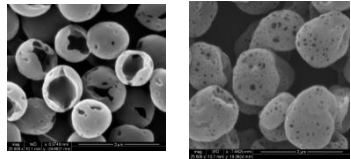
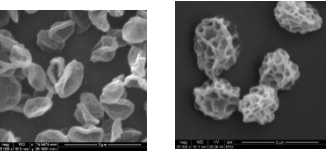
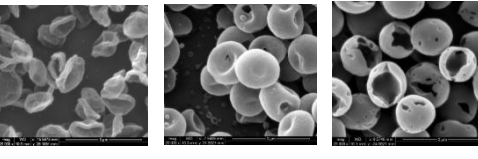
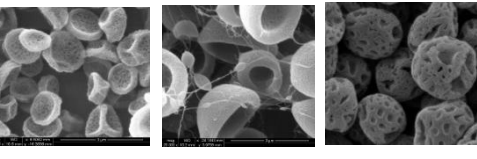
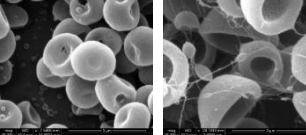
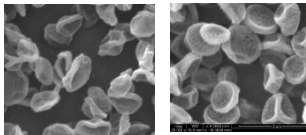
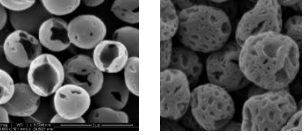


**Figure 3-13** Effect of RH on the deposited morphologies obtained by electrospaying solutions of 35 kDa PS/DCM (a,b) and 15 kDa EC/DCM (c,d); flow rate: 2  $\mu$ l/min, scale bar: 1  $\mu$ m.

### 3.3.7. Proposed mechanisms

Similarly to electrospinning works (see section 3.1.1) we have found differences in microstructure (of the particle in this case) depending on the type of polymer, its initial concentration, its molecular weight, and the solvent.

**Table 3-3** Main trends in particle surface topography observed in the present study, changing different factors at high RH.

<p>(1) effect of solvent (<math>c_0 = 5\%</math> w/v)</p>	<p>PS-35 MEK                      DCM</p> 		<p>EC-15 MEK                      DCM</p> 		
<p><b>DCM gives more porous structures for PS and more “holey” for EC</b></p>					
<p>(2) effect of polymer in MEK (<math>c_0 = 5\%</math> w/v)</p>	<p>low <math>M_w</math> polymer EC-15                      PMMA-15                      PS-35</p> 			<p>high <math>M_w</math> polymer EC-220                      PMMA-350                      PS-350</p> 	
<p><b>EC (most deflated, corrugated) → PMMA → PS (most rigid/spherical)</b></p>					
<p>(3) effect of concentration in MEK</p>	<p><b>From wet, sticky shell like particles → hollow particles, thin shells → thicker shells for low <math>M_w</math>/porous surface for high <math>M_w</math></b></p>				
<p>(4) effect of polymer <math>M_w</math> in MEK (<math>c_0 = 5\%</math> w/v)</p>	<p>PMMA 15 kDa                      350 kDa M</p> 		<p>EC 15 kDa                      220 kDa</p> 		<p>PS 35 kDa                      350 kDa</p> 
<p><b>higher <math>M_w</math> results in more porous surface than low <math>M_w</math></b></p>					

The most obvious effects due to RH in our experiments are the disappearance of nanojets arising in coulombic instabilities, the appearance of surface porosity and the

wet deposition at the lowest initial polymer concentrations. In addition to these morphological changes, we observe differences in extent of corrugation (buckling).

The four most important effects caused by RH on particle porosity (or surface topography) versus the studied factors are summarized in Table 3-3, and are listed in more detail next:

- (1) The primary effect of solvent is for DCM to give more porous structures than MEK, (both in PS and in EC).
- (2) The main effect from the polymer is that PS (the tested polymer with the lowest affinity for water) forms more globular particles than EC or PMMA, and high molecular weight PS has the biggest tendency to form porous microstructure.
- (3) The main effect from initial polymer concentration is to form a wet, sticky deposition at low (0.2% w/v) concentration; less sticky or solid, thin sometimes porous shell at intermediate (1% w/v) concentration, and thicker, sometimes porous shells at high (5% w/v) concentration. Pore size increases with initial polymer concentration in the case of the high molecular weight polymers (PS-350, PMMA-350, EC-220). For the low molecular weight polymers (PS-35 and PMMA-15) increasing the initial concentration did not give more porous structures, the effect of initial concentration is reflected only in a thicker shell for the higher initial concentration.
- (4) The main effect from polymer molecular weight (at least at high concentration) is to give more porous structures for the high Mw than for the low Mw. This trend is observed for the 5% w/v polymer concentration, but is not present in the moderate (1% w/v) concentration case.

A complete physical model and its mathematical formulation would be quite complex, and is therefore beyond the scope of this work. Instead we attempt a qualitative explanation of the major effects based on expected mechanisms and phenomena leading to the observed trends.

Our model starts by considering the droplet temperature. Our solvents, MEK and DCM are water immiscible and quite volatile. The surface temperature of the evaporating droplets can be easily estimated considering pure solvents. Using the relation between the solvent's wet bulb temperature and its boiling point, proposed by Miller et al [45]

the droplet surface temperature for MEK is around 9°C and for DCM is -18°C. At these temperatures and at any of the elevated RH test conditions used, water vapor is expected to condense on the droplets. So water condensation is expected to be the dominant mechanism for the water getting the droplet surface (while the droplet is liquid and the polymer remains dilute on the droplet surface). The net charges on the droplet surface may act as nucleation sites for water.

One candidate location for the start of polymer precipitation (vitrification) on the electro sprayed droplets is just underneath the nanodrops of condensed water. Since this is where the water and the polymer concentrations are the highest, therefore where thermodynamic instability would first occur. It is more likely for the polymer to precipitate (or vitrify) at the water-solution interfaces between the droplet and its many nanodrops of condensed water. At the same time the water nanodrops are expected to imprint dimples on the droplet surface due to the higher surface tension of water. The dimples will act as templates during polymer precipitation similarly to BFF. Therefore, one way to explain the observed differences in porosity is to predict differences in nanodrop size at the time of polymer precipitation.

The rate of water condensation on a DCM droplet ought to be faster, for a given RH, than on a MEK droplet of equal initial size. The reason is that the water vapor concentration gradient will be steeper next to a DCM droplet because the water vapor concentration at the colder droplet surface will be lower. As more water accumulates (per amount of solvent lost) in the case of DCM, the condensed nanodrops will grow in size and perhaps coalesce. Furthermore, water solubility in DCM is negligible, while it is finite in MEK. This means that water will diffuse into MEK droplet more readily. As a result, the condensed water nanodrops on a MEK droplet will grow slower, if at all, than on a DCM droplet. In addition, in the case of a faster evaporating droplet (DCM), the polymer Péclet number would be higher, resulting in higher polymer concentration at the droplet surface (for a given % loss of the solvent). In conclusion, it seems more probable to find imprints left by water nanodrops on DCM droplets than on MEK droplets, for the same polymer and initial concentration (considering similar polymer solubilities in the two solvents). This is indeed found in the experiments; see Table 3-3 and Figures 3-12(b) and 3-13(b) (PS-35) and Figures 3-10(b) and 3-13(d) (EC-15).

This model would predict that a polymer with less affinity for water, such as PS in our experiments (i.e. having lower cloud-point water concentration), would precipitate earlier (on the solution/water interface), when the nanodrops are smaller (see row (1) in the Table 3-3).. If these nanodrops cause templating smaller pore size would be obtained with such polymer. This may explain why smaller pores form for PS-35 than for EC-15 in DCM, a solvent for which the templating scenario is more probable (as argued before).

In the low concentration samples in MEK, we would not expect significant surface porosity by BFF. In these cases, although water condensation is expected, templating by this water may not be happening, either because (1) water diffuses into the solution phase (more so in MEK than in DCM, as mentioned earlier), or because (2) the polymer does not precipitate forming a layer around the water nanodrops. Thus, significant amount of water can get into the core of the droplet at low polymer concentration. The presence of water in the core may explain the hollow particle formation (found typically at 1% w/v concentration), as it may slow down the polymer diffusion into the core (compared to the low humidity cases). It is also possible, that at low concentrations MEK and water phase separate in the process due to their low affinity (immiscibility) before polymer precipitation takes place. The wet particle (or droplet) deposition at the lowest concentration indicates that polymer vitrification was delayed by the presence of water in these cases.

As we discussed earlier, the mechanism for surface pore formation is possible by nanodrop templating for high molecular weight samples at the highest concentration. However, for the lower molecular weight samples we have not found surface porosity, but hollow particles, instead. Similarly to the low relative humidity cases, we would expect less polymer accumulation on the droplet surface for low than for high molecular weight polymers. According to the discussed model, the higher polymer concentration on the surface would prevent the condensed water nanodrops to coalesce. The higher viscoelasticity of the high molecular weight polymers may also play a role in preventing such coalescence. However, for the lower molecular weight samples the water may coalesce forming a bigger template in the polymer solution droplet.

### 3.4. Conclusions

We have studied the effect of ambient relative humidity (RH) on the particle formation mechanism during electrospray with different solutions of non-water soluble polymers (PMMA, EC, and PS) having either “low” (~10-35 kDa) or “high” (220-350 kDa) molecular weight, and a volatile, water immiscible solvent (either butanone or dichloromethane), at different initial concentration (0.2, 1.0, or 5.0% w/v).

We have found that the most notable effect due to RH is the prevention of coulombic instabilities (while at low RH we found Coulombic instabilities only with a few exceptions). We interpret that water from the ambient is transported into the polymer solution phase, accelerating the formation of a glassy polymer phase, which becomes a shell that is rigid enough to prevent the reaching of the Rayleigh instability diameter.

The surface porosity of the particle also differs much at low and high RH comparing the corresponding initial solutions. At low RH (very dry ambient) the particle surface is smooth, while at high (~60-70%) RH, it is not smooth, being porous at high molecular weight and high initial polymer concentrations. At lower concentrations, the surface pores become smaller and less obvious, even disappearing. For the low molecular weight solutions, the porosity is not present or visible. Under high RH, the solutions with lowest polymer concentration (0.2% w/v) leads to wet collection at the same collection distance from the electrospray needle as used at other concentrations. This result (not described before, or attributed to the presence of high RH in any electrospray works) is surprising, and might be related to plasticization by the water in the solution.

When using butanone as solvent, the pores are significantly smaller than when dichloromethane is used. We think that water condenses on the surface of the droplet and interacts with the solution in different ways. In the case of dichloromethane solvent evaporation and water condensation are faster than for butanone. Therefore, we attribute the formation of the marked porous structure to the templating of the droplet surface by condensed water nanodrops, leaving an imprint. This proposed mechanism is similar to the phenomenon called breath figure formation, which has been described to explain similar structures on spin coating films, as well as on electrospun nanofibers. However, this mechanism is not as prominent for the case of butanone, where the pores are smaller and occupy a smaller fraction of the particle envelope, or do not form.



### 3.5. References

- [1] Xie, J., Jiang, J., Davoodi, P., Srinivasan, M. P., Wang, C.-H. (2015). Electrohydrodynamic atomization: A two-decade effort to produce and process micro-/nanoparticulate materials. *Chemical Engineering Science*, 125, 32-57.
- [2] Bock, N., Dargaville, T.R., Woodruff, M. A. (2012). Electro spraying of polymers with therapeutic molecules: State of the art. *Progress in Polymer Science*, 37, 1510-1551.
- [3] Liu, J., Kumar, S. (2005). Microscopic polymer cups by electrospinning. *Polymer*, 46(10), 3211-3214.
- [4] Xie, J., Lim, L. K., Phua, Y., Hua, J., Wang, C.-H. (2006). Electrohydrodynamic atomization for biodegradable polymeric particle production. *J. Colloid Interface Sci.*, 302, 103-112.
- [5] Zheng, J., He, A., Li, J., Xu, J., Han, C. C. (2006). Studies on the controlled morphology and wettability of polystyrene surfaces by electrospinning or Electro spraying. *Polymer*, 47, 7095-7102.
- [6] Eda, G., Shivkumar, S. (2007). Bead-to-fiber transition in electrospun polystyrene. *J. Appl. Polym. Sci.*, 106, 475-787.
- [7] Park, C. H., Lee, J. (2009). Electro sprayed polymer particles: effect of the solvent properties. *J. Appl. Polym. Sci.*, 114, 430-437.
- [8] Hirose, Y., Natori, I., Sato, H., Tanaka, K., Usui, H. (2011). Fabrication of fine particles of semiconducting polymers by electro spray deposition. *IEICE Trans. Electron.*, E94-C(2), 164-169.
- [9] Bock, N., Woodruff, M. A., Hutmacher, D. W., Dargaville, T. R. (2011). Electro spraying, a reproducible method for production of polymeric microspheres for biomedical applications. *Polymers*, 3, 131-149.
- [10] Ikeuchi M., Tane R., Ikuta K. (2012). Electro spray deposition and direct patterning of polylactic acid nanofibrous microcapsules for tissue engineering. *Biomed. Microdevices*, 14, 35-43.
- [11] Bohr, A., Yang, M., Baldursdóttir, S., Kristensen, J., Dyas, M., Stride, E., Edirisinghe, M. (2012). Particle formation and characteristics of Celecoxib-loaded poly(lactic-co-glycolic acid) microparticles prepared in different solvents using electro spraying. *Polymer*, 53(15), 3220-3229.

- [12] Nath, S. D., Son, S., Sadiasa, A., Min, Y. K., Lee, B. T. (2013). Preparation and characterization of PLGA microspheres by the electrospaying method for delivering simvastatin for bone regeneration. *Int. J. Pharmaceutics*, 443, 87-94.
- [13] Bodnár, E., Rosell-Llompart, J. (2013) Growth dynamics of granular films produced by electrospay. *J. Colloid Interface Sci.*, 407, 536-545.
- [14] Mahaling, B., Katti, D. S. (2014). Fabrication of micro-structures of poly [(R)-3-hydroxybutyric acid] by electro-spraying/-spinning: understanding the influence of polymer concentration and solvent type. *J. Mater. Sci.*, 49, 4246-4260.
- [15] Almería, B., Gomez, A. (2014). Electrospay synthesis of monodisperse polymer particles in a broad (60 nm-2  $\mu$ m) diameter range: guiding principles and formulation recipes. *J. Colloid Interface Sci.*, 417, 121-130.
- [16] Liu, J., Rasheed, A., Dong, H., Carr, W. W., Dadmun, M. D., Kumar, S. (2008). Electrospun Micro- and Nanostructured Polymer Particles. *Macromolecular Chemistry and Physics*, 209, 2390-2398.
- [17] Huang, L., Bui, N.-N., Manickam, S. S., McCutcheon, J. R. (2011). Controlling Electrospun Nanofiber Morphology and Mechanical Properties Using Humidity. *J. Polym. Sci. B Polym. Phys.*, 49, 1734-1744.
- [18] Pai, C.-L., Boyce, M. C., Rutledge, G. C. (2009). Morphology of Porous and Wrinkled Fibers of Polystyrene Electrospun from Dimethylformamide. *Macromolecules*, 42, 2012-2114.
- [19] Megelski, S., Stephens, J. S., Chase, D. B., Rabolt, J. F. (2002). Micro- and Nanostructured Surface Morphology on Electrospun Polymer Fibers. *Macromolecules*, 35, 8456-8466.
- [20] Zheng, J., Zhang, H., Zhao, Z., Han, C. C. (2012). Construction of hierarchical structures by electrospinning or Electrospaying. *Polymer*, 53, 546-554.
- [21] Lu P., Xia, Y. (2013). Maneuvering the Internal Porosity and Surface Morphology of Electrospun Polystyrene Yarns by Controlling the Solvent and Relative Humidity. *Langmuir*, 29, 7070-7078.
- [22] Demir, M. M. (2010). Investigation on glassy skin formation of porous polystyrene fibers electrospun from DMF. *eXPRESS Polymer Letters*, 4(1), 2-8.
- [23] Fashandi, H. Karimi, M. (2012). Pore formation in polystyrene fiber by superimposing temperature and relative humidity of electrospinning atmosphere. *Polymer*, 53, 5832-5849.
- [24] Kiselev, P., Rosell-Llompart, J. (2012). Highly aligned electrospun nanofibers by elimination of the whipping motion. *J. Appl. Polym. Sci.*, 125, 2433-2441.

- [25] Nezarati, R. M., Eifert, M.B., Cosgriff-Hernandez, E. (2013). Effects of Humidity and Solution Viscosity on Electrospun Fiber Morphology. *Tissue Engineering, Part C*, 19(10), 810-819.
- [26] Dayal, P., Liu, J., Kumar, S., Kyu, T. (2007). Experimental and Theoretical Investigations of Porous Structure Formation in Electrospun Fibers. *Macromolecules*, 40, 7689-7694.
- [27] Casper, C. L., Stephens, J. S., Tassi, N. G., Chase, D. B., Rabolt, J. F. (2004). Controlling Surface Morphology of Electrospun Polystyrene Fibers: Effect of Humidity and Molecular Weight in the Electrospinning Process. *Macromolecules*, 37, 573-578.
- [28] Liu, W., Huang, C., Jin, X., (2014). Tailoring the grooved texture of electrospun polystyrene nanofibers by controlling the solvent system and relative humidity. *Nanoscale Res. Lett.*, 9(1), 350.
- [29] Bae, H.-S., Haider, A., Kamruzzaman Selim, K. M., Kang, D.-Y., Ki, E.-J., Kang, I.-K. (2013). Fabrication of highly porous PMMA electrospun fibers and their application in the removal of phenol and iodine. *J. Polymer Res.*, 20, 158.
- [30] Li, L., Jiang, Z., Li, M., Li, R., Fang, T. (2014). Hierarchically structured PMMA fibers fabricated by electrospinning. *Royal Society of Chemistry Advances*, 4, 52973-52985.
- [31] Katsogiannis, K. A. G., Vladislavljević, G. T., Georgiadou, S. (2015). Porous electrospun polycaprolactone (PCL) fibres by phase separation. *European Polymer Journal*, 69, 284-295.
- [32] Pinnau, I., Freeman, B. D. (Eds.) (2007). *Membrane Formation and Modification*. (ACS Symp. Ser. 744.) American Chemical Society, Washington, D.C.
- [33] Peng, N., Widjojo, N., Sukitpaneinit, P., Teoh, M. M., Lipscomb, G. G., Chung, T.-S., Lai, J.-Y. (2012). Evolution of polymeric hollow fibers as sustainable technologies: Past, present, and future. *Progr. Polymer Sci.* 37(10), 1401-1424.
- [34] Mulder, M. (1996). *Basic Principles of Membrane Technology*. Kluwer Academic Publishers, Dordrecht.
- [35] van de Witte, P., Dijkstra, P.J., van den Berg, J.W.A., Feijen, J. (1996). Review Phase separation processes in polymer solutions in relation to membrane formation. *J. Membrane Sci.*, 117, 1-31.
- [36] Guillen, G. R., Pan, Y., Li, M., Hoek, E. M. V. (2011). Preparation and Characterization of Membranes Formed by Nonsolvent Induced Phase Separation: A Review. *Ind. Eng. Chem. Res.*, 50, 3798-3817.

- [37] Bunz, U. H. F. (2006). Breath Figures as a Dynamic Templating Method for Polymers and Nanomaterials. *Adv. Mater.*, 18, 973-989.
- [38] Ferrari, E., Fabbri, P., Pilati, F. (2011). Solvent and Substrate Contributions to the Formation of Breath Figure Patterns in Polystyrene Films. *Langmuir*, 27(5), 1874-1881.
- [39] Park, M. S., Kim, J. K. (2004). Breath Figure Patterns Prepared by Spin Coating in a Dry Environment. *Langmuir*, 20, 5347-5352.
- [40] Ruffo, G. A. (2011). Geometrical features induced in polymer structures by self-assembly and their exploitation for biomedical use. Doctoral Thesis. University of Trento, Italy.
- [41] Tian, Y., Jiao, Q., Ding, H., Shi, Y., Liu, B. (2006). The formation of honeycomb structure in polyphenylene oxide films. *Polymer*, 47, 3866-3873.
- [42] Shenoy, S. L., Bates, W. D., Frisch, H. L., Wnek, G. E. (2005). Role of chain entanglements on fiber formation during electrospinning of polymer solutions: good solvent, non-specific polymer-polymer interaction limit. *Polymer*, 46(10), 3372-3384.
- [43] Larsen, G., Spretz, R., Velarde-Ortiz, R. (2004). Use of Coaxial Gas Jackets to Stabilize Taylor Cones of Volatile Solutions and to Induce Particle-to-Fiber Transitions. *Adv. Mater.*, 16, 166-169.
- [44] Wang, H., Liu, Q., Yang, Q., Li, Y., Wang, W., Sun, L., Zhang, C., Li, Y. (2010). Electrospun poly(methyl methacrylate) nanofibers and microparticles. *J. Material Sci.*, 45(4), 1032-1038.
- [45] Miller, R. S., Harstad, K., Bellan, J. (1998). Evaluation of equilibrium and non-equilibrium evaporation models for many-droplet gas-liquid flow simulations. *Int. J. Multiphase Flow*, 24(6), 1025-1055.

## **4. Structure and growth of granular films produced by electrospray deposition**

This chapter is a revised and updated version of published article [56].

### **4.1. Introduction**

ElectroSpray Deposition (ESD) is suitable for preparing micrometer-thin or thinner layers as it is based on micro- or nano-droplets of uniform sizes. In addition, the high electrical charge on the droplets prevents their agglomeration in the spray, and allows electrophoretic precipitation onto electrically conducting substrates [1]. Films of different materials have been prepared by ESD in the context of different applications: (a) Inorganics (e.g. metals, ceramics, semiconductors, etc) have been prepared from electrosprays of nanoparticle suspensions (sols) and solutions of precursors which are pyrolyzed post deposition [1]. A 2005 review [1] cites ~90 articles dealing with ESD-coated inorganics for uses in diverse applications, like fuel cells, solar cells, lithium battery electrodes, gas sensors, optoelectronic devices, and ferroelectric materials. To these, we have found more recent works [2-9]. (b) Synthetic polymers constitute a second material category, which has been wet-coated to form continuous films for uses in organic photovoltaic structures [10], organic light emitting diodes (OLED's) [11-13], superhydrophobic or controllable wetting surfaces [14, 15], drug-eluting coatings of coronary stents [16, 17], PEM fuel cell membranes [18], coatings for SAW resonators

[19], and photoresist coatings over fragile thin films [20]. (c) Finally, Biopolymers (proteins, DNA, polysaccharides) have been electrosprayed for creating protein and DNA-based arrays for biosensors and cell research [21-24], and starch films [25]. Other materials are cited in [1].

In most ESD studies the function of the film depends on its film-averaged behavior, while the morphological characterization of the film is local. However, the distribution over the film of the variables characterizing morphology (such as thickness or porosity) is not investigated, or assumed to be uniform. However, electro spray studies by Rietveld et al. [20] and Morozova et al. [24] have shown that film thickness can vary significantly from the film center to its edge. Non uniform profiles of particle collection mass flux have also been predicted in numerical simulations of the ESD process, both for single electrosprays [26, 27] and multiple-electrospray systems [28-30]. Therefore, uneven distribution of the local film properties (thickness, porosity, etc) ought to be expected a priori, before any optimization of the process (e.g. electrical field) is attempted.

Therefore, the objective of this work is to investigate the factors which can influence the distribution of thickness, mass and porosity. Specifically, we characterize experimentally the growth dynamics of coatings by electro spray-generated ethyl cellulose (EC) particles. The EC particles form by drying of the electro spray droplets while in flight towards the collection surface. EC, a water-insoluble polysaccharide, has been chosen as the solute for this study because its coatings are highly stable under storage, thus convenient to work with, and because it leads to measurable effects. We follow the structure and dimensions of the granular coatings in time, and study how they are influenced by chamber relative humidity and collection mass flux. Mass flux is varied via the electrodes separation. These factors have been studied because they influence the accumulation of electrical charge on the coating. Indeed, the coatings grow not only thicker, but wider as well. We show the reason to be electrostatic buildup on the coatings, wherein electrical charges taken to the coating by the electro spray particles modify the electric field in the spray. ESD has long been performed over conducting substrates in order to prevent electrostatic charging [31]. However, we know of no research (experimental or numerical) that have looked into the question of how electrostatic charging of the coating affects its own growth dynamics.

## 4.2. Materials and Method

### 4.2.1. Materials

All reagents were used as purchased, without further purification. Ethyl cellulose (EC, Sigma-Aldrich, 4 cP viscosity, 48% ethoxyl content, density  $\rho_{EC} = 1.14$  g/ml) was dissolved at 50 g/L (5% w/v) in 2-butanone (MEK, Sigma-Aldrich, ACS reagent grade) at room temperature. From the viscosity a number-average molecular weight around 13-15 thousand Dalton has been estimated by applying the Mark-Houwink equation [32]. The electrical conductivity of the solution was measured by measuring the DC current through a narrow polyimide-coated fused silica capillary across which a low DC voltage was established. The measured value is  $5.9 \cdot 10^{-4}$  S/m at 25.3°C. Nitrogen (Carbueros Metálicos, Premier grade) is used as primary drying gas and as co-flow gas around the electrospray needle. Substrates used for particle collection were cut from p-type boron doped silicon wafers (Compart Technology Ltd., P/Boron, <100>, 500  $\mu\text{m}$  thickness), and were used without cleaning or removal of native  $\text{SiO}_2$ .

### 4.2.2. Electrospray deposition apparatus

The electrospray capillary tube ('needle') is a square-cut polyimide-coated fused-silica tubing (OD = 200  $\mu\text{m}$ , ID = 100  $\mu\text{m}$ , length ~80 mm). It is housed within a chamber, as shown in Fig. 4-1(a). The chamber is defined by four glass walls, a methacrylate top plate, and an aluminum plate (Al plate) at the bottom. Collection substrates are placed on the Al plate. Thin slits exist under two of the chamber walls (as shown in Fig. 4-1(a)), through which collection substrates are moved in and out of the chamber, and drying gas flows out of the chamber. A circular back plate electrode (back plate) is placed 17 mm behind the needle in order to better define a directional electric field in the space occupied by the electrospray. The distance between the electrospray needle and the collection plate ( $H$  in Fig. 4-1(a)) was adjusted by moving the needle and back plate together within the chamber.

The plate is perforated at several locations to allow nitrogen flow. However, nitrogen also flows in the space between the back plate and the chamber walls. The total nitrogen flow into the chamber is 1.0 slpm. Water vapor is sometimes added to the nitrogen stream in order to elevate the relative humidity (RH) in the chamber. The chamber RH

is monitored using a Vaisala HM34 humidity meter, whose probe (not shown) is inserted through the Al and teflon plates.

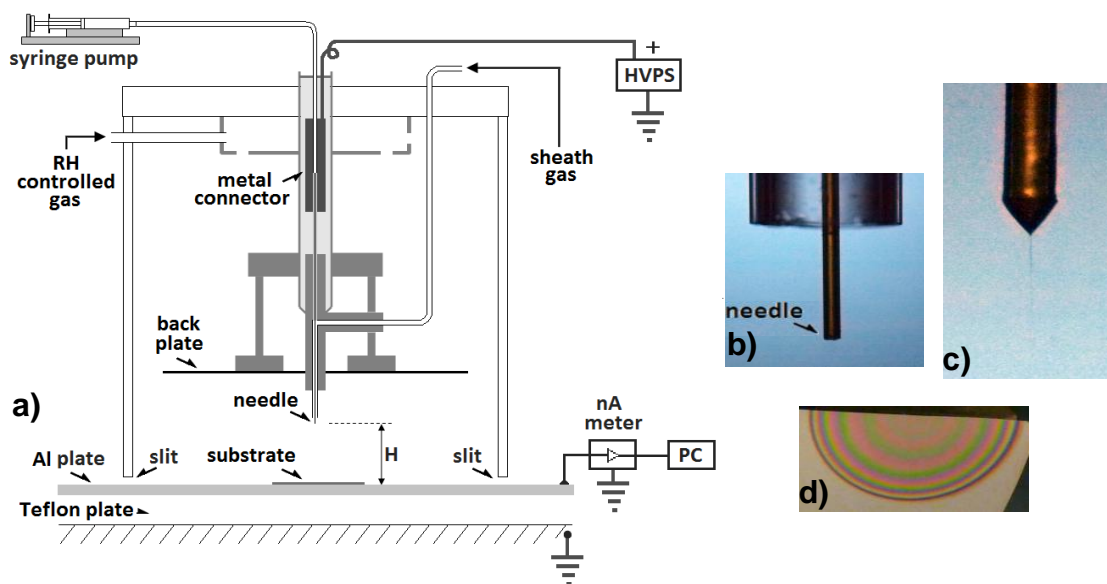


**Figure 4-1** (a) Electro spray deposition chamber (approx. to scale, with  $H = 20$  mm as shown) and surrounding equipment, (b) close up of the silica tube (“needle”) and sheath gas tube, (c) Taylor cone-jet meniscus at the end of the needle, (d) annealed film with Newton rings.

Concentric with the electro spray needle is a glass tube (1.3 mm ID, 1.8  $\mu$ m OD) (Fig. 4-1(b)) used for supplying a gentle stream (0.015 slpm) of solvent vapor-laden nitrogen, around the electro spray needle. Such sheath gas was found to be essential to prevent drying of the Taylor cone meniscus [33].

The collection substrates are sufficiently conductive to be at the same potential as the bottom plate. The electro spray current was determined by collecting the current on a homemade nano-ammeter connected to the Al plate. It was acquired at 10 Hz into a computer (PC).

EC/MEK solution is infused into the electro spray needle using a Harvard Apparatus HD-2000 syringe pump, at a constant volumetric rate of 2  $\mu$ L/min. High voltage was applied to the liquid at the metal connector shown in Fig. 4-1(a). The high voltage is generated with power supply (HVPS) Matsusada AMS-10B2-LC. It is fed through a safety resistor (not shown) to the metal connector and to the back plate (Fig. 4-1(a)). The voltage at these elements was measured using a high voltage probe.



### 4.2.3. Electrospray film deposition

In a typical experiment, the Taylor cone meniscus characteristic of the cone-jet electro spray mode was established at the needle end (Fig. 4-1(c)). A Si substrate was quickly positioned under the electro spray, and, after a desired length of time (*deposition time*), it was quickly removed. Metal foils were used as ancillary substrates to keep the Al plate clean. The chamber temperature during all of the experiments fell between 25.6 and 26.1 °C. The current-vs-time traces are collected to monitor the electro spray process. Since the motion of the substrates left a pulse on this trace, they could be used to obtain accurate determinations of the actual duration of each deposition.

The nitrogen flow pattern in the chamber did not cause non-circular depositions at  $H = 20$  mm, whereas at  $H = 40$  mm the deposits were slightly non circular (although this effect may not be due to the airflow pattern).

### 4.2.4. Deposits characterization

Local thickness (film thickness) was determined both on the granular films, and on the compact film obtained after thermal annealing. These data allow us to determine profiles of surface mass density (kg/m<sup>2</sup>) and film porosity. To determine these film thicknesses, the samples (substrate + film) were prepared as follows. The granular film sample as collected was placed onto a glass slide with its edge positioned under the desired fracture line. It was then nicked with a diamond tip, and gentle pressure caused the sample to fracture. The cut was aimed at the geometrical center (within 1 mm), and any samples with erroneous cuts were discarded. One half of the granular film sample was then saved for thickness measurement, while the other half (or, sometimes, a whole new film) was annealed on a hot plate at 160 °C for 30 s. This temperature is slightly higher than the softening temperature of the EC used (155 °C). When molten, a clearly visible light-interference pattern of Newton rings develops (Fig. 4-1(d)). The Newton ring pattern does not change even if the heating is sustained for much longer than the minimum time needed to develop the pattern (less than 1/2 min). This test demonstrates that the polymer collapses vertically under the heat, but does not flow along the film. After annealing the samples, they were then fractured along the symmetry plane at liquid N<sub>2</sub> temperature, using the already outlined procedure. All samples were gold coated (~10 nm) and imaged by SEM in top and cross section views in a Quanta 650

scanning electron microscope (run typically at 30kV, with a 10 mm working distance). This procedure is based on the circularity of the deposits, since the profiles are taken from the fractured films along two orthogonal symmetry planes.

#### **4.2.5. Spray imaging experiments**

The photos of the ES plume of 5.0 w/v% EC-butanone solution were taken in a separate experiment from the detailed thickness profile study. We used the same electrode configuration and the co-flow settings but we removed the walls of the chamber to obtain proper illumination and avoid light scattering from the glass walls of the chamber. Therefore, these experiments were carried out without the humidity controlled N<sub>2</sub> flow, and the ambient relative humidity was 60.1 %. Other conditions were similar to the other runs (see Table 4-1):  $H = 20$  mm, liquid flow rate = 2  $\mu$ l/min, applied voltage = 6.14 kV,  $T = 26.7$  °C. The measured DC current was 65 nA, and the film diameter after 14 min deposition was 20.75 mm.

The illumination was 1-point backlighting at  $\sim 45^\circ$  angle to the left to the camera objective. These settings were necessary to make the spray visible, but it also induced strong light scattering from the needle, and from the collected film itself, especially after longer collection time, as well as from other light scatterers (mostly dust particles and edges). Thus, the region close to the needle is clearly visible, but the bottom part of the spray is much more difficult to analyze. However, it is possible to see the outline of the spray. The digital camera exposure was 8 s, and the time reported ( $t$ ) marks the end of the exposure time.

### **4.3. Results and Discussion**

#### **4.3.1. Macroscopic features of the film**

Fig. 4-2 shows camera images of two samples collected for 15 minutes, which is the longest deposition time of this study, at two RH conditions, using normal and long exposures. Under normal exposure, spots or regions of uneven grayness can be clearly seen at the center of the film collected at low RH (Fig. 4-2(a)), suggesting uneven topography. On the other hand, the film at high RH (Fig. 4-2(b)) has uniform grayness,

indicating smooth topography. The overexposed images (Figs. 4-2(c-d)) reveal tracks left on the substrates as they were moved under the electro spray. These tracks are a few times narrower than the circular deposits, showing that the electro spray was narrower than the size of the particle deposit. This effect, noted in all samples of the study, is due to the spray expansion over time as the particles are collected on the same spot. Additionally, the low RH image (Fig. 4-2(c)) shows the presence of an uneven crown around the coating, which would appear to be made of particles ejected from the circular deposit (rather than deposited from the spray).

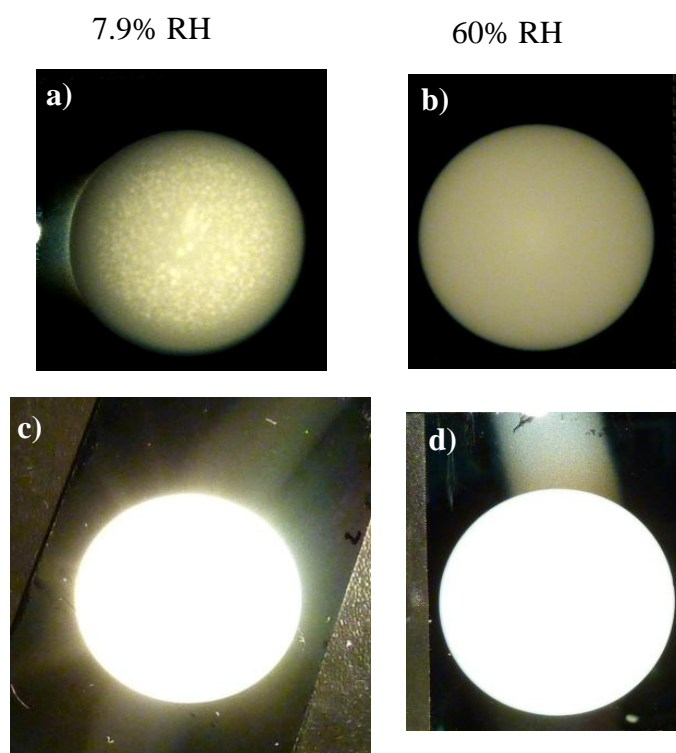


**Figure 4-2** Short exposure (top) and long exposure (bottom) photographs of 2 EC films collected during 15 minutes under dry (a, c) and under humid (b, d) chamber ambient conditions.  $H = 20$  mm.

### 4.3.2. Particle size, shape, and segregation by size

In order to optimize the spraying and collection conditions that allow for complete drying of the particles, the Si substrates have been electro spray-deposited for short time and the particles were inspected by SEM. The duration of the collection was kept short in order to avoid overlapping of the collected particles (droplet relics). Larger particles distributed in a main central region of the coating (Fig. 4-4(a)), and much smaller

particles are found at the periphery of the coating (Fig. 4-4(b)). Figs. 4-4(c-d) show magnified SEM images from these locations. The particles from the central region (Fig. 4-4(c)) are uniformly sized and are cup (or bowl) shaped, suggesting that they first form as capsules by formation of a polymeric skin at the droplet surface, and then the capsules deflate as solvent leaves from within the capsule. On the other hand, the smaller particles at the periphery of the coating are not uniform in size and shape (Fig. 4-4(d)), many of them being elongated or pointed (tear shaped) indicating that they underwent coulombic instability as they dried up (see chapter 2).

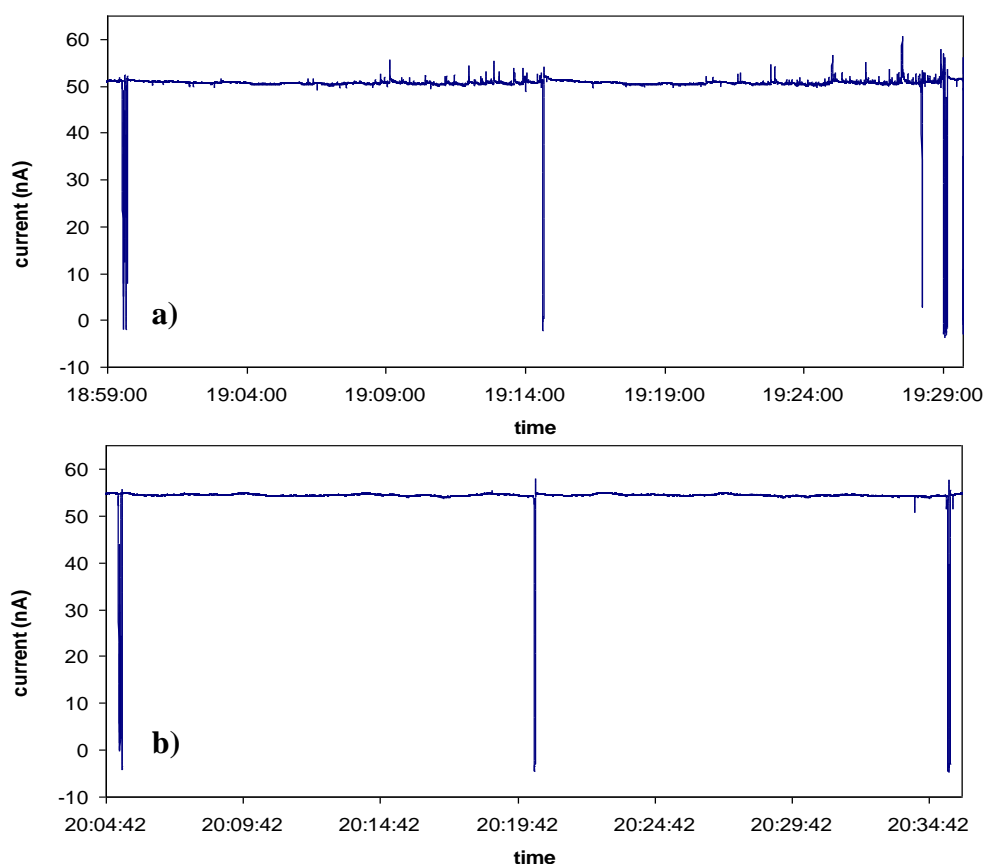


**Figure 4-3** Electrical current vs. time traces for two consecutive collections of EC/MEK electrospray coatings under dry and humid conditions. Same conditions as in Fig. 2.

The formation of two distinct size modes is characteristic of droplet formation by the breaking up of a liquid jet by growth of axisymmetric varicose waves, the so called Rayleigh jet break up mechanism [34, 35, 36]. The larger mode is made of so called main droplets (or primary droplets), while the smaller size mode is made of so called satellite droplets, The diameter of the main drops is fairly regular. Their mean diameter is about twice the jet diameter (theoretically, 1.89 times in the case of inviscid liquids;

see Chapter 1. Introduction). Satellite droplets are more variable in size, and grow in the liquid bridges that form between main droplets when they detach from the jet.

The distribution of our particles with large, uniformly sized, particles in the center of the collection region, and small, broadly sized, particles in the periphery is also consistent with the Rayleigh jet break up mechanism. Because of their smaller inertia, satellite droplets formed from EHD microjets typically migrate towards the periphery of the spray, while the main droplets remain within the spray core [35, 37].

When electrospaying under elevated chamber RH (Figs. 4-4(e)-(f)), the particles arising from the main droplets (Fig. 4-4(e)) become flatter, pancake-shaped, with a corrugated or dimpled wall. The particles from satellite droplets (Fig. 4-4(f)) are now round instead of elongated. As discussed in the previous two chapters, this is related to the difference in polymer precipitation mechanism, which facilitates the earlier formation of a glassy shell on the droplet surface. Thus, coulombic instability is thwarted for the satellite droplets.

Filaments are nearly absent from the main particles in the low RH case, and completely absent in the elevated RH case. Therefore, it is reasonable to conclude that the main particles in Fig. 4-4 form early in the droplet evaporation history, before the first coulombic instability is met. The mechanism of formation is polymer precipitation on the surface of the droplet, before the critical droplet radius for coulombic instability. Next, the solvent leaves the droplet by diffusion through the polymeric shell, wherefrom it evaporates into the gas surroundings. In doing so, the shell collapses, adopting a bowl shape, as found in the deposits. The mechanical strength of the initial polymeric shell prevents the development of coulombic instability, even despite the fact that during droplet collapse the electrical stresses will increase, as the net charges on the particle surface are brought closer together.

The shape change experienced by the satellite particles, from elongated to round, as the RH is elevated (Fig. 4-4(d) to 4-4(f)) suggests that ambient water vapor acts in this case as a non-solvent for the water-immiscible polymer, accelerating its precipitation on the droplet surface (see chapter 3).

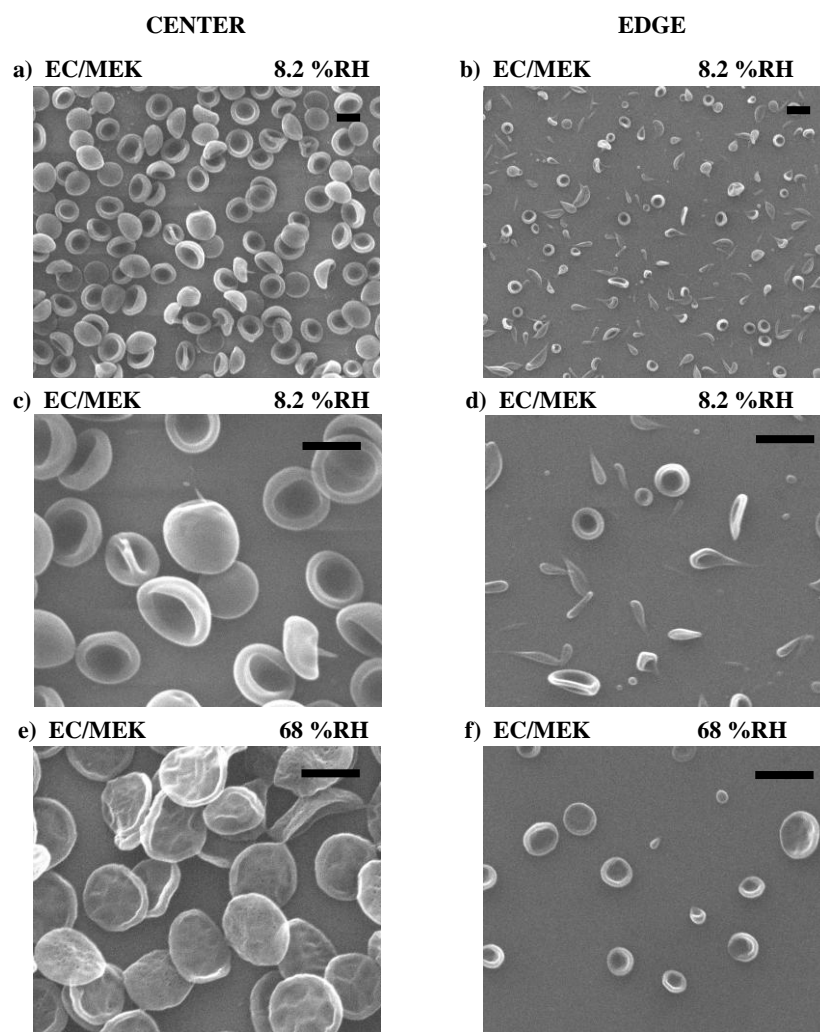


**Figure 4-4** SEM images of droplet residues collected from EC/MEK at dry (a – d) and humid conditions (e, f). Sampling locations: (a, c, e) are from near center of coating, (b, d, f) are from the edge of the coatings. Deposition time = 10 s;  $H = 20$  mm;  $2 \mu\text{L}/\text{min}$ . Scale bar =  $1 \mu\text{m}$ .

### 4.3.3. Local mass distribution on the particulate film

Coatings from EC/MEK electrosprays were collected under low and high chamber RH values ('low' being below 10%, and 'high' above 50%), and different combinations of needle-to-plate separation  $H$ , and deposition time  $t$ . At needle-to-plate separation  $H = 20$  mm, collection times were  $t = 1, 4,$  and  $15$  min; whereas the effect of reducing the deposition flux was studied by increasing  $H$  to 40 mm for  $t = 4$  min. Table 4-1 lists the conditions tested along with some film characteristics. Fifteen minute depositions at low

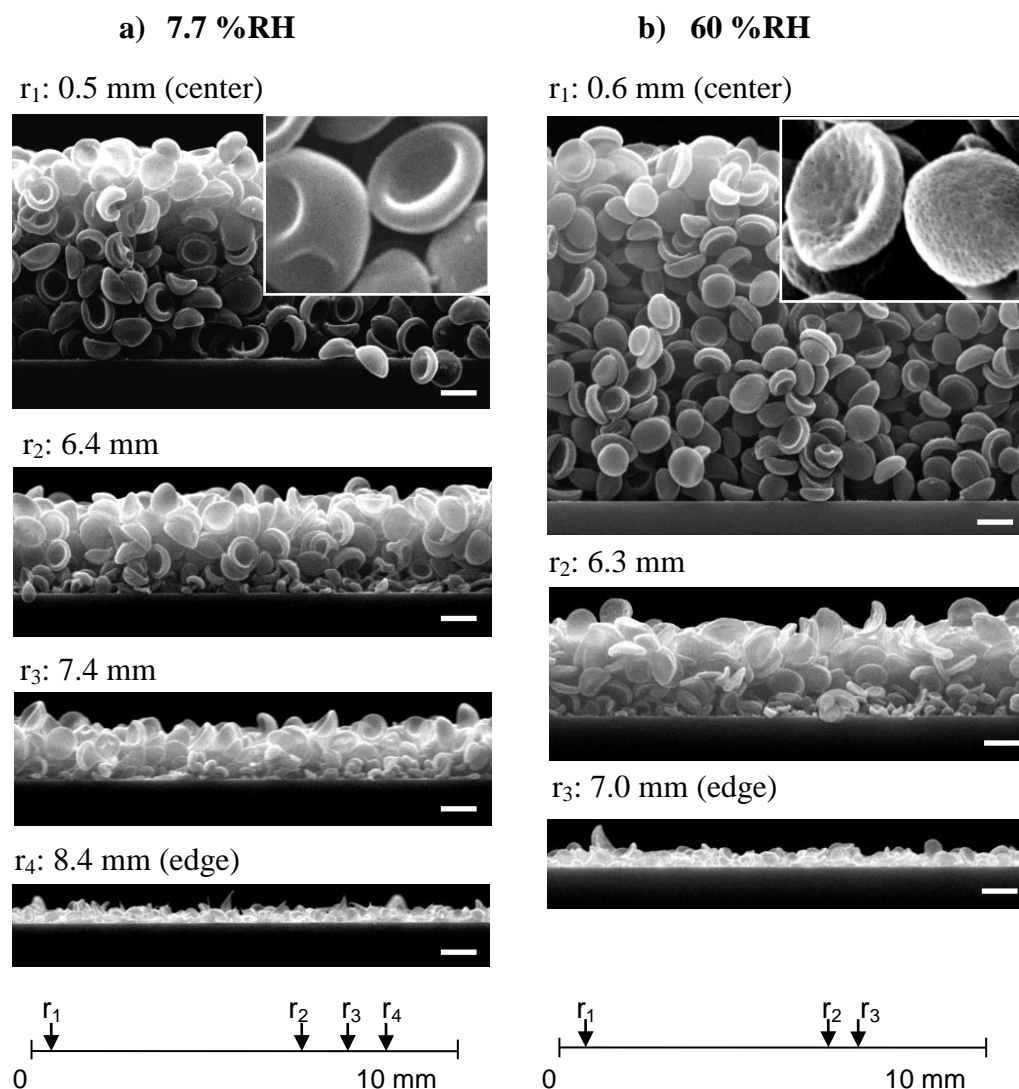
RH at  $H = 20$  mm were not analyzed by SEM because, as discussed earlier in the context of Figs. 4-2(a) and 4-3(a), they had unstable electrical current and variable topography and particle deposition beyond the deposit circular outline.

Fig. 4-5 shows SEM views of the cross sections at different radial positions, for one coating sprayed under low chamber RH (left side) and another under high RH (right side). Near the center of the coating (Fig. 4-5, top two images) the particles are uniformly sized and similarly shaped. However, a thin underlying sublayer made of relics from satellite droplets is found at more peripheral locations (in the two  $r_2$  images, as well as the  $r_3$  image on left side). The steadiness of the electrical current-time traces during these depositions (Fig. 4-3) proves that the electrospaying process was stable. Consequently, we conclude that the electrospray, made of a core of main droplets/particles and a shroud of satellite droplets/relics, must have widened throughout the duration of the deposition process.

Figure 4-5 also shows the influence of RH on the radial distribution of film thickness. At the center of the coating ( $r_1$ ), the film is much thicker at high than at low RH. Away from the center, at  $r_3$  and beyond, the reverse happens. In sum, the particulate mass spreads out more when electrospaying at low than at high RH; in other words, the electrospray appears to be widening.

Figure 4-5 also shows that the particle shape varies with radial location for the high RH collection. Particles are distinctly flatter at  $r_2$  ('pancake' like) than at  $r_1$  ('bowl' like). The reason for this effect is still unclear, but it indicates the high sensitivity to droplet history, perhaps also to initial droplet properties (size and charge, expected to be slightly different for the main droplets depending on deposition location).

The insets of the top images in Fig. 4-5 ( $r_1$ ) show the differences in particle texture depending on RH. The skin of the particles is smooth for low RH (Fig. 4-6(a)), but dimpled and pin-holed for high RH (Fig. 4-6(b)). Surface dimples are also visible at high RH at  $r_2$ .



**Figure 4-5** SEM micrographs of two EC deposits collected at dry conditions (on left side) and humid conditions (on right side), for different radial positions from the center ( $r = 0$ ). High magnification insets show differences in surface texture of the particles. Deposition time = 4 min.  $H = 20 \text{ mm}$ . Scale bar =  $1 \mu\text{m}$ .

The formation of pores has been observed when fibers are electrospun into humid air. It is believed that different mechanisms are at play, including the non-solvent action of water vapor during polymer precipitation, or of water condensed on the liquid-air interface by evaporative cooling (breath figure formation) [50].

Finally, the coatings in Figure 4-5 are relatively dense, having a rough surface, as is typical of ballistic deposition [49], namely particle deposition in which Brownian diffusion plays a negligible role. Ballistic deposition is characterized by large values of the dimensionless number called Péclet number,  $Pe = aU/D$ , which is the ratio of the



deposition speed of the particles  $U$  to the effective thermal speed associated with Brownian movement  $D/a$ , where  $a$  is the particles diameter, and  $D$  their diffusion coefficient [57]. This value can be estimated at about  $6.5 \times 10^5$ ; therefore, diffusion plays a negligible role on the deposition process.

#### 4.3.4. Film thickness, mass and porosity profile

Next, the EC deposits collected at different  $H$ , RH, and  $t$  were sectioned and annealed (as described in section 4.2), and the thicknesses of the granular and annealed films were determined at different radial locations. Film annealing consolidates the film without causing redistribution of the polymer from one radial location to another (as discussed in section 4.2). The local granular film thickness  $h_G$  has been determined from SEM images such as those of Fig. 4-5, averaging 17 measurements evenly distributed across each SEM image. Each measurement is taken from the Si substrate to the highest point of the uppermost particle in focus. This is equivalent to considering particles within a depth of two or three particle diameters, typically, from the focal plane (cross sectioned plane).

The *local depth-averaged porosity*  $P$  (or volume fraction of the matrix, gas phase) can be obtained easily from the thicknesses of the granular film  $h_G$  and of the annealed film  $h_A$  (at the same radial location):

$$P = \frac{h_G - h_A}{h_G} \quad (4.1)$$

$P$  equals 1 minus the depth-averaged *solid fraction* or *density*  $h_A/h_G$ . By using Eq. (4.1) to determine  $P$ , we assume that the density of the solid phase is the same in the granular (porous) film as in the annealed (consolidated) film. In other words, we assume that the annealed film does not have air bubbles. However, it is possible if not probable that the particles in the granular film will have some fraction of voids. If these disappear during annealing, these voids will contribute to the porosity  $P$ .

Radial profiles of  $h_G$ ,  $h_A$ , and of  $P$  are shown in Figure 4-6 for deposits formed with  $H = 20$  mm, at high and at low RH. The local porosity values have been computed from the polynomial fits of the radial profiles of the  $h$  data ( $h_G$  or  $h_A$ ) shown fitting the data

points. The  $h_G$ - and  $h_A$ -profiles (Figs. 4-6(a)-d) show that the films widen over time, both at high and at low RH. However, this expansion is slower when the RH is higher.

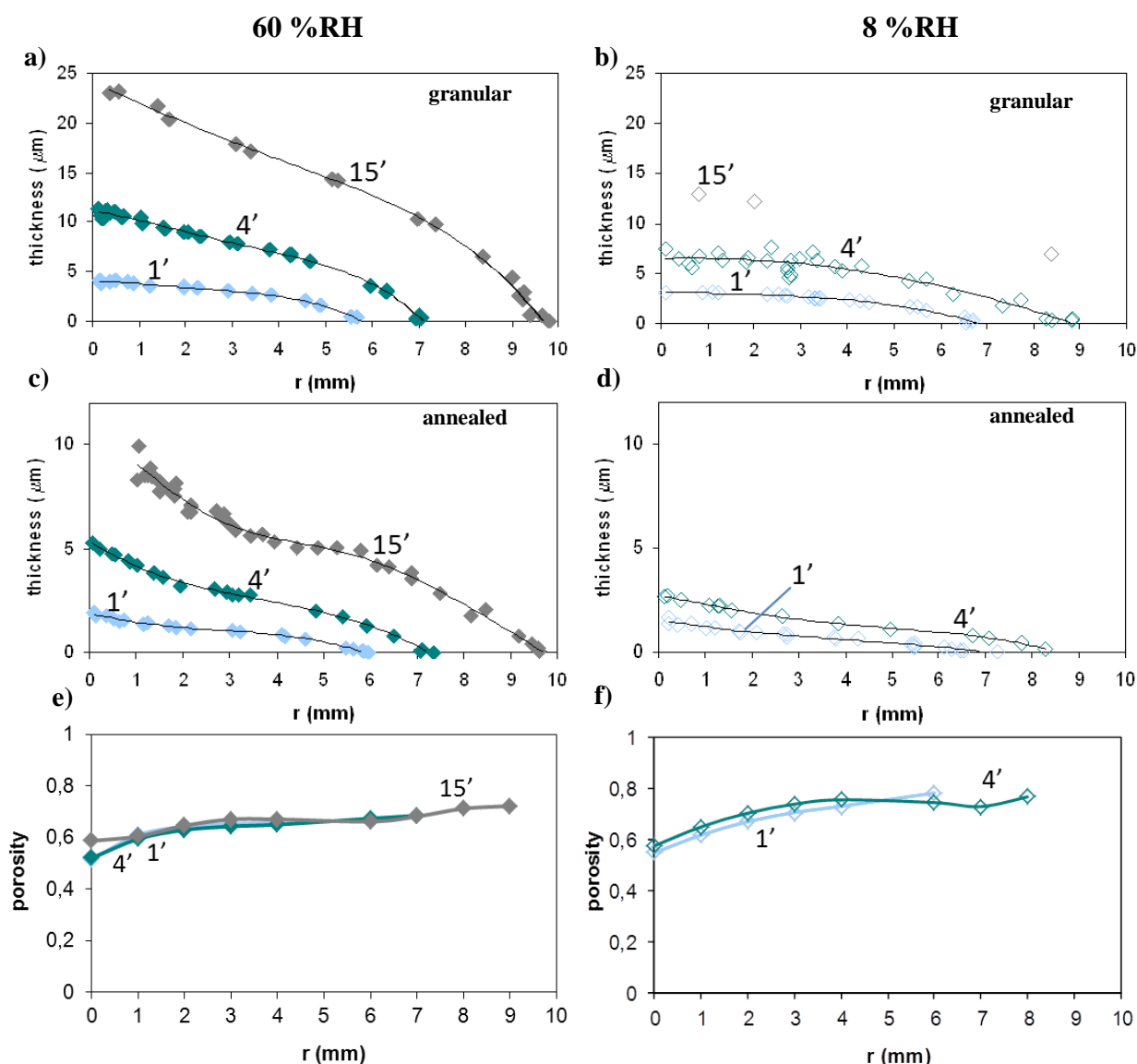


**Figure 4-6** Radial profiles of local thickness and porosity for granular coatings for different deposition times and RH, and local thickness for the annealed films.  $H = 20$  mm. The trend lines are best fit polynomials of different degrees, and are used to compute the porosity according to Eq. (4-1). Actual RH values are provided in Table 4-1.

Fig. 4-7 shows similar graphs for the films collected during 4 min at  $H = 40$  mm, at low and high RH. As before films show more spreading at low RH than at high RH. However, the spreading is less than in Fig. 4-6 ( $H = 20$  mm) for the same deposition time, because the mass flux is smaller at a larger  $H$ , such that the same electrostatic charge is distributed over a much wider area.

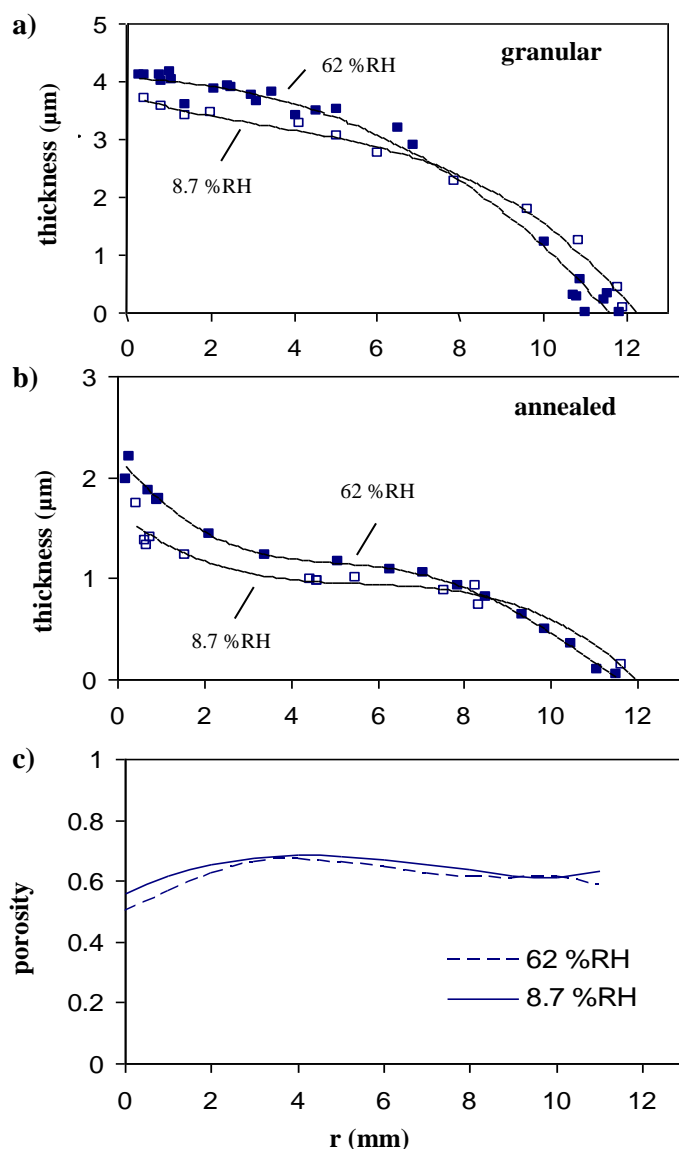


**Figure 4-7** Radial profiles of the local thickness of granular coatings and of annealed films, and the local porosity of granular coatings (Eq. 4-1), for  $H = 40$  mm and  $t = 4$  min, under high and low RH (as indicated). The data scatter near to the film edge in Fig. 4-7(a) is due to lack of roundness of these films.

An interesting feature of the annealed profiles in Figs. 4-6 and 4-7 is the non-zero slope at the film axis ( $r=0$ ). Any mass flux with zero slope at the axis should result in a mass profile with slope zero at the same location on the coating. Perhaps in the experiments, the slope at the axis is zero but this is not resolved. This explanation is consistent with greater mass flux within one or two millimeters from the spray axis, as predicted in numerical simulations by Arumugham-Achari et al. [51] who show that spray drag causes faster air motion near the spray axis (as also anticipated by Hartmann et al. [37]).

The radial profiles of porosity  $P$  are graphed at the bottom of Figs. 4-6 and 4-7, and show a local minimum of  $P$  at the spray axis, with a slightly greater porosity at the lower RH, more so at smaller  $H$ . Figs. 4-6(e-f) show that the porosity profiles are very similar for different deposition times, despite the fact that the film grows both in thickness and width.

The minimum  $P$  at the axis is consistent with the aforementioned stronger gas motion near the axis, as the droplets entrained by this part of the gas flow would be expected to collect with higher impact velocity.

Table 4-1 summarizes several film properties: film diameter, overall porosity, surface roughness, and collection efficiency. Overall porosity is defined consistently with Eq. (4.1) as  $(V_G - V_A)/V_G$ , where  $V_G$  and  $V_A$  are the total volumes of the granular and the annealed film. These volumes are obtained by integration of the  $h$  vs.  $r$  functions from Figs. 4-6 and 4-7. *Overall porosity* follows the same trend with humidity as the local porosity (Figs. 4-6(e), 4-6(f), 4-7(c)).

Surface roughness is the RMS roughness based on the thickness data:

$$R = \sqrt{\frac{\sum_{i=1}^N \sum_{j=1}^{n_i} (h_{ij} - \bar{h}_i(\bar{r}_i))^2}{\sum_{i=1}^N n_i}}, \quad (4.2)$$

where

$i$  = index of SEM image

$j$  = index of thickness measurement within each SEM image

$h_{ij}$  = local thickness of the film (for SEM image  $i$ )

$\bar{r}_i$  = radial position (center of SEM image  $i$ )

$\bar{h}_i(\bar{r}_i)$  = local average thickness (average for SEM image  $i$ )

$n_i$  = number of thickness measurements for SEM image  $i$  (= 17)

$N$  = number of SEM images considered determination of  $R$

Surface roughness is quite small in all cases (Table 4-1), being several times smaller than the particle cup diameter (1.2  $\mu\text{m}$ ). As mentioned earlier, this is expected for a compact granular film formed by ballistic deposition [49].

Collection efficiencies,  $\eta$ , are also shown in Table 4-1. They have been computed as the ratio of the mass in the annealed film and the polymer mass pumped through the electrospray needle, as

$$\eta (\%) = 100 \times \frac{V_A \rho_{EC}}{M} \quad (4.3)$$

Here, the mass in the annealed film is  $V_A$  times the density of EC,  $\rho_{EC}$ , divided by the mass of polymer infused into the electrospray needle during deposition  $M \approx c Q t$ , with  $c$  being the EC/MEK concentration (w/v),  $Q$  the infusion rate of solution (2  $\mu\text{l}/\text{min}$ ), and  $t$  the actual deposition time.

Table 4-1 shows that  $\eta$  values are as low as 67%, being less for the high RH condition (all else being equal). For a given {RH, H} combination, the efficiencies get smaller as the films get thicker (as collection time increases), showing that the trend is not due to errors from measurement for the thinnest films. However, the very lowest value of  $\eta = 67\%$ , found for the case of  $t = 4$  min and low RH at  $H = 20$  mm, may be explained in part by the large noise in the data for this case, as shown Fig. 4-6(b). Also, crown collection patterns forming outside the film as in Fig. 4-2(b), and any coarse liquid emissions associated to Taylor cone bursts observed during the longest low RH collections, may explain the mass defects, at least partly.

#### 4.3.5. Hypothesis of electrostatic charging

The existence of satellite particles sublayers (Fig. 4-5,  $r_2$  locations) and film growth over time (Figs. 4-6 and 4-7) strongly suggest that the electrospray becomes wider over time, during the film formation process. Spray widening is easily shown in images of the spray (Fig. 4-8). Fig. 4-8(a) shows the spray captured at the start of deposition, while Fig. 4-8(b) after 12.9 minutes from the start of collection. By overlapping the two spray outlines in Fig. 4-8(c), we see nearly coincident sprays near the needle, while the rest of the spray broadens significantly after 12.9 minutes. The other significant observation relates to the angle at which the spray outline, which coincides approximately with an electric field line (as expected for electrophoretic motion), meets the collection surface. At  $t = 0.13'$  the spray meets the collector at an angle of  $\sim 90^\circ$ , as expected for a conducting substrate. At  $t = 12.9'$ , however, the angle has been reduced

by a half, which indicates that the film has developed a strong parallel field component. In other words, the electrical potential is no longer uniform over the film. The radial component of the electric field must be comparable in magnitude to the axial component when the spray-collector angle is about  $45^\circ$ . Clearly, the radial field is created by electrostatic charging that has accumulated on the granular deposit.

The fact that the chamber relative humidity slows down the growth in film width (Fig. 4-6, and Table 4-1) is consistent with this hypothesis, since charge transport by conduction mediated by adsorbed water molecules on surfaces is an effective mechanism for “dissipation” of static electricity.

The electrical field caused by accumulated charge on the film should be noticed sooner near the film than near the needle, because (i) the electric field (total field) near the needle is dominated by the high potential gradients caused by needle curvature, and (ii) the field strength due to the film charge should weaken with distance from it. As argued below, the electrical field caused by the film charges and their images in the conductive substrate is dipolar, which has a faster decay with distance than the field caused by a monopolar distribution of charge.

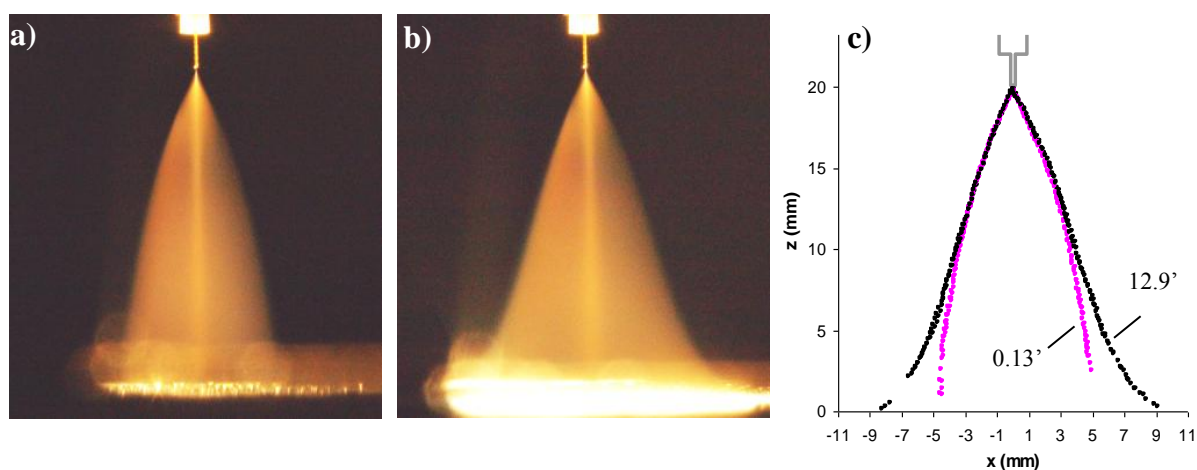


**Figure 4-8** Spray plume evolution during ES deposition. Photos of the plume correspond to collection times of (a) 0.13 min and (b) 12.9 min. c) Spray outlines at different collection times. The digital camera exposure was 8 s.

A detailed computation of the distribution of collected charge on the film, and its effects on the electric field and the spray dynamics is beyond the scope of this work. However, the following simplified calculation can be used to show that the total amount of charge deposited on the collector can be sufficient to perturb the spray electrostatically.

The electro spray can widen only if the contribution to the electric field strength due to the charge accumulated in the film  $E$  is comparable or exceeds the field strength without charge accumulation  $E_0$ , of order  $V/H_0 = 1.6 \times 10^5$  V/m, where  $V$  is the back plate voltage (6 kV) and  $H_0$  is the back plate-to-collection plate separation (37 mm). To compute  $E$  we follow Uecker et al. [52]. In truth,  $E$  is not only associated to the charges accumulated on the film. In addition to the collected “free charge”, the film will develop polarization charges which partly neutralize the free charge through an effective dielectric constant  $\varepsilon$ . Because, in the film, the free charges are localized at or near the interface between the gas and the polymer phases (except at the contacts between particles), the value of  $\varepsilon$  will lie between 1 (air) and 4 (dielectric constant of EC). In addition, the free and polarization charges induces “image” charges of the same amount and opposite polarity inside the substrate, effectively producing a charged double layer centered on the substrate-film interface. The field due to the *double layer* along the spray axis is a vector that points in the opposite direction as the electric field that drives the spray towards the collector (due to the needle, back plate, and spray). The magnitude of this field  $E$  can be estimated as follows [52]. We assume uniform film thickness  $\bar{h}$ , and uniform electrical charge distribution in the film with a volume density  $\bar{\rho}$  (C/m<sup>3</sup>). The field strength  $E$  along the spray centerline at a distance from the double layer that is small compared to  $\bar{h}$  but large compared to its radius  $R$  is given by [52]:

$$E \approx \frac{\bar{\rho} \bar{h}^2}{2 \varepsilon \varepsilon_0 R}, \quad (4.4)$$

where  $\bar{\rho}$  is the average free charge,  $\varepsilon$  is the effective dielectric constant of the film,  $\varepsilon_0$  is the electric permittivity of vacuum ( $8.854 \times 10^{-12}$  F/m). (Uecker et al. [52] studied a planar distribution of surface charge of density  $\bar{\sigma}$ , while we have made use of the relationship  $\bar{\sigma} = \bar{\rho} \bar{h}$ .) The maximum attainable  $\bar{\rho}$  can be easily computed as

$$\bar{\rho}_{\max} = \frac{(1-P)I \rho_{EC}}{Q c_{EC}} \quad (4.5)$$

where  $P$  is the film porosity ( $\sim 0.6$ ),  $I$  is the electro spray measured current ( $5 \times 10^{-8}$  A),  $\rho_{EC}$  is the mass density of EC ( $1.14 \times 10^3$  kg/m<sup>3</sup>),  $Q$  is the liquid flow rate ( $3.3 \times 10^{-11}$

$\text{m}^3/\text{s}$ ), and  $c_{EC}$  is the concentration of EC in the solution ( $50 \text{ kg}/\text{m}^3$ ). Therefore,  $\bar{\rho}_{\text{max}} = 1.6 \times 10^4 \text{ C}/\text{m}^3$ . This represents a maximum charge density that our films could accumulate, assuming that it is not dissipated away from the film, for example by adsorbed water molecules on surfaces. By using the maximum value of  $\bar{\rho}_{\text{max}}$  in Eq. (4.4), we obtain an upper bound on the electric field caused by the deposited charge. For representative values of film thickness of  $5 \text{ }\mu\text{m}$  and radius of  $7 \text{ mm}$ , we obtain  $E = 3.3 \times 10^6 \text{ V}/\text{m}$  for  $\varepsilon = 1$ , and  $E = 8.4 \times 10^5 \text{ V}/\text{m}$  for  $\varepsilon$  of 4. These upper bound estimates exceed the reference field strength  $E_0$  of  $1.6 \times 10^5 \text{ V}/\text{m}$ . Therefore, we must conclude that (1) the electrostatic charge transported by the spray to the film is enough for distorting the field and thus change the spray trajectories near the collector, and (2) that probably, the charge that accumulates on the film is much less than the charge that has been transported to the film by the spray. This charge reduction could be caused by dissipation or conduction through the film, or perhaps, even electrical discharges within the film.

To close, the hypothesis of electrostatic charging of the film can also explain qualitatively why RH has less influence at  $H = 40 \text{ mm}$  than at  $20 \text{ mm}$  (for equal collection time). At  $H = 40 \text{ mm}$ , the same spray charges spread over a wider area, thus producing a smaller field (since  $\bar{\sigma} = \bar{\rho} \bar{h}$  present in Eq. (4.3) is reduced), and the coating is thinner (smaller  $\bar{h}$ ). As predicted by our simple model, the reduction in both of these factors in Eq. (4-3) (smaller surface charge density, and smaller spacing between the charges and their images) causes a reduction in  $E$ . Therefore, less spray expansion will be expected.



**Table 4-1** Characteristics of the EC films.

H (mm)	RH (%)		Deposition time $t$ <sup>(a)</sup> (min)	Applied voltage <sub>(b)</sub> (kV)	Collected current (nA)	Film diameter <sub>(c)</sub> (mm)	Film volume rate <sup>(d)</sup>		Overall porosity $(\dot{V}_G - \dot{V}_A) / \dot{V}_G$	rms surface roughness ( $\mu\text{m}$ )	Collection efficiency $\eta$ (%)
							granular $\dot{V}_G$ ( $\text{mm}^3/\text{min}$ )	annealed $\dot{V}_A$ ( $\text{mm}^3/\text{min}$ )			
20	7.6	<i>dry</i>	1 <sup>(e)</sup>	6.0	51	13.9	0.246	0.074	0.70	0.20	85
20	7.7	<i>dry</i>	4	6.0	51	17.5	0.208	0.059	0.72	0.43	67
20	7.9	<i>dry</i>	15	6.0	51 <sup>(f)</sup>	24.3 <sup>(g)</sup>	-	-	-	-	-
20	60	<i>humid</i>	1	6.0	54	11.7	0.234	0.082	0.65	0.26	94
20	60	<i>humid</i>	4	6.0	54	14.3	0.206	0.072	0.65	0.32	82
20	60	<i>humid</i>	15	6.0	54	19.3	0.207	0.066	0.68	0.29	75
40	8.7	<i>dry</i>	4	7.9	54	26.3	0.235	0.075	0.67	0.21	86
40	62	<i>humid</i>	4	7.9	58	22.9	0.226	0.084	0.63	0.25	96

<sup>a</sup> Except where noted, the deposition time differed by less than 3% from the nominal value shown here.

<sup>b</sup> Values downstream of the safety resistor, measured with a high voltage probe.

<sup>c</sup> Determined from thickness vs. position data by SEM.

<sup>d</sup> Equal to the integrated film volume divided by the actual deposition time, by integration of the  $h$  vs  $r$  data.

<sup>e</sup> For this condition, the actual deposition time differed by less than 5% from the nominal (63 sec. for the granular, and 58 sec. for the annealed films).

<sup>f</sup> Initial current value is reported, as the current becomes unstable during the deposition (as shown in Fig. 4-2(e)).

<sup>g</sup> Determined from analysis of Fig. 4-2(a).

## 4.4. Conclusions

A study has been made of the shape and morphology of granular coatings produced by the electrospray deposition of ethyl cellulose microparticles. The main droplets from this electrospray evaporate to form dry particles, before they become coulombically unstable. They are collected ballistically to form compact deposits of uneven thickness. As the deposition time increases, these films become wider, while the deposit thickness in the inner regions grows slower than linearly with time. Thin sublayers of small particles (satellite residues) appear ‘buried’ under a significantly thicker layer of large particles (main residues) at some radial positions in the film away from the center. All of these observations suggest that over time the electrospray widens, as the film grows. Imaging of the sprays have confirmed this hypothesis.

The radial growth of the films is slowed down when the relative humidity is raised (to about ~60% in our experiments). This observation is consistent also with the hypothesis

that the spray expands over time due to the electrostatic repulsion between the spray and the charges that accumulate on the granular coating.

While the electrostatic repulsion is reduced at RH of 60 %, the EC films still grow in radius significantly over time at that condition, indicating charge accumulation in the film even at that RH.

An incidental observation at this RH is the radial variation of main particle morphology (shape and texture).

The distribution of polymer mass has been obtained from the film thicknesses of the thermally annealed coatings. It is not uniform over the collection area in any of the coatings made. A maximum in film thickness suggests enhanced mass flow near the spray centerline, also seen in numerical simulations by Arumugham-Achari et al. [51]

The porosities of the granular films were determined from the local coating thicknesses for the granular and the annealed film. Porosity is relatively uniform, decreasing slightly in the central region of the coating. The porosity is somewhat affected by RH, being slightly higher for the low RH condition.

The data generated in this study could further be used for validating theoretical models which consider the electrostatic charging of the coating. Two simplifying features of our spray is that its droplets do not suffer coulombic instabilities, and their size is distributed bimodally, as a result of quasi-periodic axisymmetric jet break up (in absence of whipping instabilities, which are more difficult to model).

## 4.5. References

- [1] Jaworek, A. (2007). Electro spray droplet sources for thin film deposition. *J. Mater. Sci.*, 42, 266–297.
- [2] Woo, J. H., Yoon, H., Cha, J. H., Jung, D. Y., Yoon, S. S. (2012). Electrostatic spray-deposited CuInGaSe<sub>2</sub> nanoparticles: Effects of precursors' Ohnesorge number, substrate temperature, and flowrate on thin film characteristics. *J. Aerosol Sci.*, 54, 1–12.
- [3] Martin, S., Garcia-Ybarra, P. L., Castillo, J. L. (2010). Electro spray deposition of catalyst layers with ultra-low Pt loadings for PEM fuel cells cathodes. *J. Power Sources*, 195, 2443–2449.
- [4] Modesto-Lopez, L. B., Biswas, P. (2010). Role of the effective electrical conductivity of nanosuspensions in the generation of TiO<sub>2</sub> agglomerates with electro spray. *J. Aerosol Sci.*, 41, 790–804.
- [5] Hogan, C. J., Biswas, P. (2008). Porous Film Deposition by Electrohydrodynamic Atomization of Nanoparticle Sols. *Aerosol Sci. Tech.*, 42, 75–85.
- [6] Wang, D., Edirisinghe, M. J., Dorey, R. A. (2008). Formation of PZT crack-free thick films by Electrohydrodynamic atomization deposition. *J. Eur. Ceram. Soc.*, 28, 2739–2745.
- [7] Mahalingam, S. Edirisinghe, M. J. (2007). Characteristics of electrohydrodynamically prepared titanium dioxide films. *Appl. Phys. A*, 89, 987–993.
- [8] Leeuwenburgh, S. C. G., Heine, M. C., Wolke, J. G. C., Pratsinis, S. E., Schoonman, J., Jansen, J. A. (2006). Morphology of calcium phosphate coatings for biomedical applications deposited using Electrostatic Spray Deposition. *Thin Solid Films*, 503, 69–78.
- [9] Kaelin, M., Zogg, H., Tiwari, A., Wilhelm, O., Pratsinis, S. E., Meyer, T., Meyer, A. (2004). Electro sprayed and selenized Cu/In metal particle films. *Thin Solid Films*, 457(2), 391–396.
- [10] Park, S.-E., Hwang, J.-Y., Kim, K., Jung, B., Kim, W., Hwang, J. (2011). Spray deposition of electrohydrodynamically atomized polymer mixture for active layer fabrication inorganic photovoltaics. *Sol. Energ. Mat. Sol. C.*, 95, 352–356.
- [11] Fukuda, T., Asaki, H., Asano, T., Takagi, K., Honda, Z., Kamata, N., Ju, J., Yamagata, Y. (2011). Surface morphology of fluorene thin film fabricated by electro spray deposition technique using two organic solvents: Application for organic light-emitting diodes. *Thin Solid Films*, 520, 600–605.

- [12] Ju, J., Yamagata, Y., Higuchi, T. (2009). Thin-film fabrication method for organic light-emitting diodes using electrospray deposition. *Adv. Mater.*, 21, 4343–4347.
- [13] Hwang, W., Xin, G., Cho, M., Cho, S. M., Chae, H. (2012). Electrospray deposition of polymer thin films for organic light-emitting diodes. *Nanoscale Res. Lett.*, 7, 52.
- [14] Burkarter, E., Saul, C. K., Thomazi, F., Cruz, N. C., Zanata, S. M., Roman, L. S., Schreiner, W. H. (2007). Electrosprayed superhydrophobic PTFE: a non-contaminating surface. *J. Phys. D: Appl. Phys.*, 40, 7778–7781.
- [15] Mateo, J. N., Kulkarni, S. S., Das, L., Bandyopadhyay, S., Tepper, G. C., Wynne, K. J., Bandyopadhyay, S. (2011). Wetting behavior of polymer coated nanoporous anodic alumina films: transition from super-hydrophilicity to super-hydrophobicity. *Nanotechnology*, 22, 035703.
- [16] Kleinedler, J. J., Foley, J. D., Alexander, J. S., Roerig, S. C., Hebert, V. Y., Dugas, T. R. (2011). Synergistic effect of resveratrol and quercetin released from drug-eluting polymer coatings for endovascular devices. *J. Biomed. Mater. Res. B*, 99B(2), 266–275.
- [17] Choi, J., Cho, S. B., Lee, B. S., Joung, Y. K., Park, K., Han, D. K. (2011). Improvement of Interfacial Adhesion of Biodegradable Polymers Coated on Metal Surface by Nanocoupling. *Langmuir*, 27, 14232–14239.
- [18] Sanders, E. H., McGrady, K. A., Wnek, G. E., Edmondson, C. A., Mueller, J. M., Fontanella, J. J., Suarez, S., Greenbaum, S. G. (2004). Characterization of electrosprayed Nafion films. *J. Power Sources*, 129, 55–61.
- [19] Sarkar, S., Levit, N., Tepper, G. (2006). Deposition of polymer coatings onto SAW resonators using AC electrospray. *Sensor. Actuat. B-Chem.*, 114(2), 756-761.
- [20] Rietveld, I. B., Suganuma, N., Kobayashi, K., Yamada, H., Matsushige, K. (2008). Electrospray deposition of photoresist: A low impact method for the fabrication of multilayered films. *Macromol. Mater. Eng.*, 293, 387–399.
- [21] Woo, C. G., Shin, H., Jeong, C., Jun, K., Lee, J., Lee, J.-R., Lee, H., You, S., Son, Y., Choi, M. (2011). Selective nanopatterning of protein via ion-induced focusing and its application to metal-enhanced Fluorescence. *Small*, 7(13), 1790–1794.
- [22] Lee, B. H., Kim, J.-W., Ishimoto, K., Yamagata, Y., Tanioka, A., Nagamune, T. (2003). Fabrication of protein microarrays for immunoassay using the Electrospray Deposition (ESD) method. *J. Chem. Eng. Jpn.*, 36, 1370–1375.
- [23] Avseenko, N. V., Morozova, T. Ya., Ataulakhanov, F. I., Morozov, V. N. (2002). Immunoassay with multicomponent protein microarrays fabricated by electrospray deposition. *Anal. Chem.*, 74, 927–933.

- [24] Morozov, V. N., Morozova, T. Ya. (1999). Electrospray Deposition as a Method for Mass Fabrication of Mono- and Multicomponent Microarrays of Biological and Biologically Active Substances. *Anal. Chem.*, 71, 3110–3117.
- [25] Pareta, R., Edirisinghe, M. J. (2006). A novel method for the preparation of starch films and coatings. *Carbohydr. Polym.*, 63, 425–431.
- [26] Grifoll, J., Rosell-Llompart, J. (2012). Efficient Lagrangian simulation of electrospray droplets dynamics. *J. Aerosol Sci.*, 47, 78–93.
- [27] Wilhelm, O., Mädler, L., Pratsinis, S. E. (2003). Electrospray evaporation and deposition. *J. Aerosol Sci.*, 34, 815–836.
- [28] Yang, W., Lojewski, B., Wei, Y., Deng, W. (2012). Interactions and deposition patterns of multiplexed electrosprays. *J. Aerosol Sci.*, 46, 20–33.
- [29] Jung, J. H., Oh, H., Kim, S. S. (2010). Numerical simulation of the deposition pattern in multiple electrohydrodynamic spraying. *Powder Technol.*, 198, 439–444.
- [30] Oh, H., Kim, K., Kim, S. (2008). Characterization of deposition patterns produced by twin-nozzle electrospray. *J. Aerosol Sci.*, 39, 801–813.
- [31] Rietveld, I. B., Kobayashi, K., Yamada, H., Matsushige, K. (2009). Process parameters for fast production of ultra-thin polymer film with electrospray deposition under ambient conditions. *J. Colloid Interface Sci.*, 339, 481–488.
- [32] Rekhi, G. S., Jambhekar, S. S. (1995). Ethycellulose – A polymer review. *Drug Dev. Ind. Pharm.*, 21, 61-77.
- [33] Larsen, G., Spretz, R., Velarde-Ortiz, R. (2004). Use of coaxial gas jackets to stabilize Taylor cones of volatile solutions and to induce particle-to-fiber transitions. *Adv. Mater.*, 16, 166–169.
- [34] Cloupeau, M., Prunet-Foch, B. (1990). Electrostatic spraying of liquids – Main functioning modes. *J. Electrostat.*, 25(2), 165-184.
- [35] Tang, K., Gomez, A. (1994). On the structure of an electrostatic spray of monodisperse droplets. *Phys. Fluids*, 6, 2317–2332.
- [36] Rosell-Llompart, J., Fernández de la Mora, J. (1994). Generation of monodisperse droplets 0.3 to 4 $\mu\text{m}$  in diameter from electrified cone-jets of highly conducting and viscous liquids. *J. Aerosol Sci.*, 25, 1093–1119.
- [37] Hartman, R. P. A., Borra, J.-P., Brunner, D. J., Marijnissen, J. C. M., Scarlett, B. (1999). The evolution of Electrohydrodynamic sprays produced in the cone-jet mode, a physical model. *J. Electrostat.*, 47, 143–170.

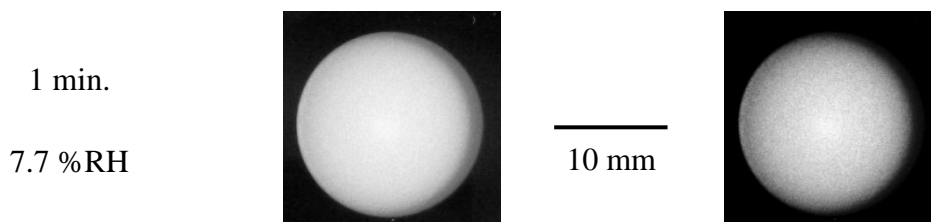
- [38] Morozov, V. N., Morozova, T. Ya., Kallenbach, N. R. (1998). Atomic force microscopy of structures produced by electrospraying polymer solutions. *Int. J. Mass Spectrom.*, 178, 143–159.
- [39] Fernández de la Mora, J. (2007). The fluid dynamics of Taylor cones. *Ann. Rev. Fluid Mech.*, 39, 217–243.
- [40] Li, D., Marquez, M., Xia, Y. (2007). Capturing electrified nanodroplets under Rayleigh instability by coupling electrospray with a sol–gel reaction. *Chem. Phys. Lett.*, 445(4-6), 271-275.
- [41] Hunter, H. C., Ray, A. K. (2009). On progeny droplets emitted during coulombic fission of charged microdrops. *Phys. Chem. Chem. Phys.*, 11(29), 6156–6165.
- [42] Burton, J. C., Taborek, P. (2011). Simulations of coulombic fission of charged inviscid drops. *Phys. Rev. Lett.*, 106, 144501.
- [43] Gomez, A., Tang, K. (1994). Charge and fission of droplets in electrostatic sprays. *Phys. Fluids*, 6(1), 404–414.
- [44] Achtzehn, T., Müller, R., Duft, D., Leisner, T. (2005). The Coulomb instability of charged microdroplets: dynamics and scaling. *Eur. Phys. J. D*, 34, 311–313.
- [45] Grimm, R. L., Beauchamp, J. L. (2005). Dynamics of field-induced droplet ionization: Time-resolved studies of distortion, jetting, and progeny formation from charged and neutral methanol droplets exposed to strong electric fields. *J. Phys. Chem. B*, 109(16), 8244–8250.
- [46] Almería, B., Deng, W., Fahmy, T. M., Gomez, A. (2010). Controlling the morphology of electrospray-generated PLGA microparticles for drug delivery. *J. Colloid Interface Sci.*, 343, 125–133.
- [47] Shenoy, S. L., Bates, W. D., Wnek, G. (2005). Correlations between electrospinnability and physical gelation. *Polymer*, 46, 8990–9004.
- [48] Morota, K., Matsumoto, H., Mizukoshi, T., Konosu, Y., Minagawa, M., Tanioka, A., Yamagata, Y., Inoue, K. (2004). Poly(ethylene oxide) thin films produced by electrospray deposition: morphology control and additive effects of alcohols on nanostructure. *J. Colloid Interface Sci.*, 279, 484–492.
- [49] Rodríguez-Pérez, D., Castillo, J. L., Antoranz, J. C. (2005). Relationship between particle deposit characteristics and the mechanism of particle arrival. *Phys. Rev. E*, 72, 021403.
- [50] Casper, C. L., Stephens, J. S., Tassi, N. G., Chase, D. B., Rabolt, J. F. (2004). Controlling Surface Morphology of Electrospun Polystyrene Fibers: Effect of Humidity and Molecular Weight in the Electrospinning Process. *Macromolecules*, 37, 573–578.

- [51] Arumugham-Achari, A. K., Grifoll, J., Rosell-Llompart, J. (2013). Two-way coupled numerical simulation of electrospray with induced gas flow. *J. Aerosol Sci.*, 65, 121–133.
- [52] Uecker, J., Tepper, G., Rosell-Llompart, J. (2010). Ion-assisted collection of Nylon-4,6 electrospun nanofibers. *Polymer*, 51, 5221–5228.
- [53] N. A. Fuchs (1989) *The Mechanics of Aerosols*. Dover, New York.
- [54] Fernández de la Mora, J., Loscertales, I. G. (1994). The current emitted by highly conducting Taylor cones. *J. Fluid Mech.*, 260, 155–184.
- [55] McDaniel, E. W., Mason, E. A. (1973). *The Mobility and Diffusion of Ions in Gases*. Wiley, New York.
- [56] Bodnár, E., Rosell-Llompart, J. (2013). Growth dynamics of granular films produced by electrospray. *J. Colloid Interface Sci.*, 407, 536-545.
- [57] Friedlander, S. K. (2000). *Smoke, Dust, and Haze (Fundamentals of Aerosol Dynamics)*. Oxford University Press, New York.

## 4.6. Appendix

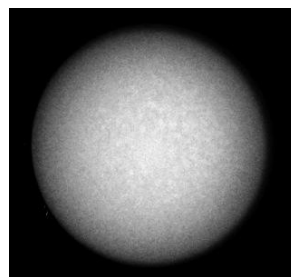
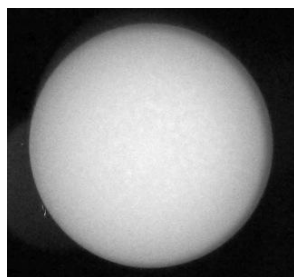
### Film top view photographs

Top view photographs of films collected at low RH reveal uneven grayness, which suggests variable film topography. Shown here are photographs of these films for deposition times of 1, 4, and 15 minutes. The images on the left side are without processing, and are shown again on the right side after having been enhanced (contrast raised to 27 and gamma taken to 0.32). A film deposited under high RH (for 15 min) has been included for comparison on the next page. All cases correspond to  $H = 20\text{mm}$ .



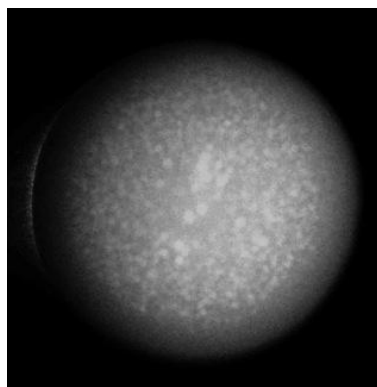
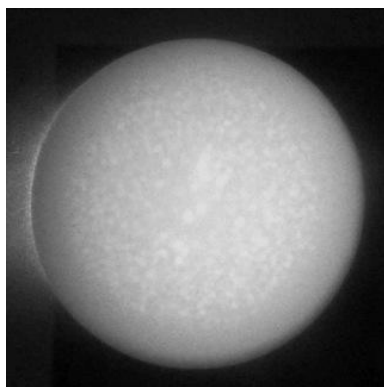
4 min.

7.8 %RH



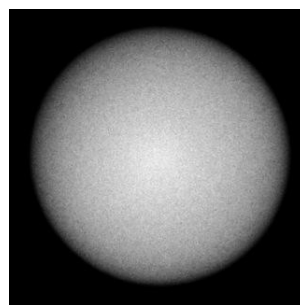
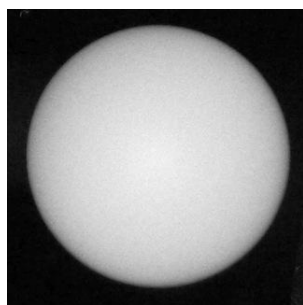
15 min.

7.9 %RH



15 min.

60 %RH





## 5. General conclusions

We have electrospayed different polymeric solutions, studying the effect of the following factors on particle morphology: polymer, solvent, initial polymer concentration, and polymer molecular weight (with weight mean in the 15-350kDa range), in order to identify the role of these factors on the drying process of the electrospayed polymer solution droplets. As polymers we have used poly(methyl)methacrylate, polystyrene, and ethyl cellulose; and as solvents, butanone and dichloromethane. In these experiments, it has been essential to use a co-flowing stream of solvent saturated gas around the electrospay needle, in order to prevent drying of the Taylor cone, particularly in the case of high molecular weight polymers above a polymer concentration (of a few % w/v typically).

The collected deposits have been analyzed by scanning electron microscopy, revealing many particle morphologies. We show that these morphologies present transitions as the initial polymer concentration is reduced, depending on the fluid dynamic regime at which polymer vitrification happens. Four regimes have been identified as: (1) Incomplete jet break up, (2) complete jet breakup without coulomb instabilities, (3) coulombic instabilities without emission of progeny droplets, and (4) coulombic instability of main droplets with emission of progeny droplets (coulombic fission).

The first regime leads to main particles surrounded by thin nanofibers, which present secondary beading. This regime happens only at the high end of the concentration range for the high molecular weight solutions. The second regime is characterized by globular particles, which may be buckled to different extent depending on the polymer and its

molecular weight. These particles do not have filaments attached. The solution concentration for this regime has a narrow range.

In the third regime, obtained at lower concentrations, the particles have one or two opposite filaments, or display elongated shapes, such as dumbbell shapes. These shapes reflect different coulombic instability pathways, some occurring with jet emission, and some without. The absence of additional nanoparticles in any of these deposits indicates that the polymeric solution dried while the particle was undergoing coulomb instability, before fragmentation. The filaments are interpreted as vitrified Rayleigh nanojets that did not break up into progeny droplets.

The fourth regime, encountered only with low molecular weight polymers, led to deposits which had particle residues from progeny droplets arising from coulombic droplet fissions. In the case of high molecular weight polymers, this regime was not observed, as the third regime extended to the lowest concentrations (0.2% w/v).

In all four regimes the polymer accumulated on the droplet surface during droplet drying, where it vitrified forming a shell. The capsule thus formed deflated as solvent evaporated from its interior. As a result, none of our polymeric solutions led to spherical particles. We argue that spherical particles made by electrospray (in other polymer/solvent systems) will have hollow or porous interior. The shell thickness depends, among other factors, on the rate of polymer accumulation relative to the rate of polymer diffusion to the droplet interior (or their ratio, the Péclet number). The shell thickness on the collected particles was dependent on the polymer and on its molecular weight, but only slightly (or not) on the initial polymer concentration.

We have also studied the effect of ambient relative humidity (RH) on the particle formation mechanism during electrospray with different solutions of non-water soluble polymers (PMMA, EC, and PS) having either “low” (~10-35 kDa) or “high” (220-350 kDa) molecular weight, and a volatile, water immiscible solvent (either butanone or dichloromethane), at different initial concentration (0.2, 1.0, or 5.0 % w/v).

We have found that the most notable effect due to RH is the prevention of coulombic instabilities (while at low RH we found Coulombic instabilities only with a few exceptions). We interpret that water from the ambient is transported into the polymer

solution phase, accelerating the formation of a glassy polymer phase, which becomes a shell that is rigid enough to prevent the reaching of the Rayleigh instability diameter.

The surface porosity of the particle also differs much at low and high RH comparing the corresponding initial solutions. At low RH (very dry ambient) the particle surface is smooth, while at high (~60-70%) RH, it is not smooth, being porous at high molecular weight and high initial polymer concentrations. At lower concentrations, the surface pores become smaller and less obvious, even disappearing. For the low molecular weight solutions, the porosity is not present or visible. Under high RH, the solutions with lowest polymer concentration (0.2 % w/v) leads to wet collection at the same collection distance from the electrospray needle as used at other concentrations. This result (not described before, or attributed to the presence of high RH in any electrospray works) is surprising, and might be related to plasticization by the water in the solution.

When using butanone as solvent, the pores are significantly smaller than when dichloromethane is used. We think that water condenses on the surface of the droplet and interacts with the solution in different ways. In the case of dichloromethane solvent evaporation and water condensation are faster than for butanone. Therefore, we attribute the formation of the marked porous structure to the templating of the droplet surface by condensed water nanodrops, leaving an imprint. This proposed mechanism is similar to the phenomenon called breath figure formation, which has been described to explain similar structures on spin coating films, as well as on electrospun nanofibers. However, this mechanism is not as prominent for the case of butanone, where the pores are smaller and occupy a smaller fraction of the particle envelope, or do not form.

Another study has been made of the shape and morphology of granular coatings produced by the electrospray deposition of ethyl cellulose microparticles. The main droplets from this electrospray evaporate to form dry particles, before they become coulombically unstable. They are collected ballistically to form compact deposits of uneven thickness. As the deposition time increases, these films become wider, while the deposit thickness in the inner regions grows slower than linearly with time. Thin sublayers of small particles (satellite residues) appear 'buried' under a significantly thicker layer of large particles (main residues) at some radial positions in the film away from the center. All of these observations suggest that over time the electrospray widens, as the film grows. Imaging of the sprays have confirmed this hypothesis.

The radial growth of the films is slowed down when the relative humidity is raised (to about ~60% in our experiments). This observation is consistent also with the hypothesis that the spray expands over time due to the electrostatic repulsion between the spray and the charges that accumulate on the granular coating.

While the electrostatic repulsion is reduced at RH of 60 %, the EC films still grow in radius significantly over time at that condition, indicating charge accumulation in the film even at that RH.

The distribution of polymer mass has been obtained from the film thicknesses of the thermally annealed coatings. It is not uniform over the collection area in any of the coatings made. A maximum in film thickness suggests enhanced mass flow near the spray centerline, also seen in numerical simulations by Arumugham-Achari et al. [51]

The porosities of the granular films were determined from the local coating thicknesses for the granular and the annealed film. Porosity is relatively uniform, decreasing slightly in the central region of the coating. The porosity is somewhat affected by RH, being slightly higher for the low RH condition.

UNIVERSITAT ROVIRA I VIRGILI

ELECTROSPRAYING OF POLYMER SOLUTIONS FOR THE GENERATION OF MICRO-PARTICLES, NANO-STRUCTURES AND GRANULAR FILMS

Eszter Bodnár